Chemical-Looping Technology: Application of Nonlinear Model Predictive Control and Reactor Network Modelling Using Biomass as a Fuel

by

Kayden Michael Toffolo

A thesis

presented to the University of Waterloo

in fulfillment of the

thesis requirement for the degree of

Master of Applied Science

in

Chemical Engineering

Waterloo, Ontario, Canada, 2023

Author's Declaration

I hereby declare that I am the sole author of this thesis. This is a true copy of the thesis, including any required final revisions, as accepted by my examiners.

I understand that my thesis may be made electronically available to the public.

Abstract

As climate change becomes a more pressing issue, there is increasing research being performed to investigate greenhouse gas reduction strategies such as carbon capture technology and sustainable fuels. To this end, chemical-looping (CL) technologies such as chemical-looping combustion (CLC) and chemical-looping gasification (CLG) are being explored to improve the sustainability of energy generation. In addition, biomass has recently been studied as a renewable fuel for this process. Various works into CL technologies have been performed, but further investigation is required in the areas of process design and control in order to verify whether this technology can feasibly be implemented for energy generation and to determine the most effective implementation strategies for CL processes.

The aim of this thesis is to determine reactor design and control strategies which can be implemented to improve the energy generation, gasification efficiency, and carbon capture effectiveness of packed bed CLC and CLG. In this work, optimal control strategies for large-scale packed bed CLC are obtained by implementing nonlinear model predictive control (NMPC). For NMPC, a multiscale model is developed to simulate the plant behaviour and validated against multiple sources of experimental data, while a pseudo-homogeneous model is used as the internal NMPC model to reduce computational costs for implementation of feedback control. By manipulating the inlet air and inert gas fluxes in the oxidation stage, and the inlet fuel flux in the reduction stage, the outlet temperature and CO_2 selectivity could be controlled in order to improve the energy generation and carbon capture effectiveness of the process. Then, a reactor network model was proposed to simulate packed bed biomass-fueled CLG and CLC, and validated using experimental data under both CLG and CLC conditions. Using this model, a variety of oxygen carrier (OC) bed lengths and locations were assessed to evaluate the resulting impact on the performance of CLG and CLC. For CLG, the highest

gasification efficiency occurred with an OC/biomass ratio of 0.25 combined with a steam/biomass ratio of 1, and the OC placed near the reactor inlet. For CLC, a fully packed bed with steam as the inlet gas resulted in the highest outlet CO_2 fraction.

These design and control strategies obtained through the NMPC scheme and reactor network model can be employed to improve the feasibility of chemical-looping technology. This would make it more CL more practical to implement in existing gasification and combustion processes, improving the sustainability of energy generation.

Acknowledgements

Table of Contents

List of Figures

List of Tables

List of Abbreviations

CL   Chemical-Looping

CLC   Chemical-Looping Combustion

CLG   Chemical-Looping Gasification

CCS   Carbon Capture and Sequestration

CCUS   Carbon Capture, Utilization, and Storage

OC   Oxygen Carrier

MPC   Model Predictive Control

NMPC   Nonlinear Model Predictive Control

PBR   Packed Bed Reactor

PFR   Plug Flow Reactor

CSTR   Continuous Stirred-Tank Reactor

LHV   Lower Heating Value

List of Symbols

Letters

A_c	Reactor cross-sectional area, m^2
a_0	BET surface area, m^2/g
a_p	Characteristic length of particle (volume/surface area), m
a_v	External particle surface area per unit volume, 1/m
b_j	Reaction rate coefficient for reaction j
$C_{c,i}$	Concentration of component i in the oxygen carrier, mol/m^3
$C_{Fe2O3,0}$	Initial oxygen carrier loading in the catalyst; mol Fe_2O_3/kg OC
C_i	Bulk concentration of component i, mol/m^3
C_{Ni}	Concentration of nickel, mol Ni/kg OC
$C_{Ni,0}$	Initial oxygen carrier loading in the catalyst; mol Ni/kg OC
$C'_{Ni,0}$	Initial oxygen carrier loading in the catalyst; kg Ni/kg OC
C_{NiO}	Concentration of nickel oxide, mol NiO/kg OC
$C'_{NiO,0}$	Initial oxygen carrier loading in the catalyst; kg NiO/kg OC
C_{pc}	Specific heat of gas in OC, J/mol/K
C_{pf}	Specific heat of gas, J/mol/K
C'_{pf}	Specific heat of gas, J/kg/K
C_{ps}	Specific heat of solid, J/kg/K
C_T	Total concentration, mol/m^3
D	Reactor diameter, m
$D_{ax,i}$	Effective axial dispersion coefficient of species i, m^2/s
$D_{e,i}$	Effective diffusivity of component i, m^2/s
$D_{k,i}$	Knudsen diffusivity of component i, m^2/s
$D_{m,i}$	Diffusion coefficient of i in the mixture, m^2/s
D_p	Particle diameter, m
d_{ij}	Diffusivity of i in j, m^2/s

d_{pore}	Pore diameter, m
$E_{a,j}$	Activation energy of reaction j, J/mol
F_i	Flowrate of gas i, mol/s
$F_{i,0}$	Inlet flowrate of gas i to a given zone, mol/s
F_T	Total gas flowrate, mol/s
$\boldsymbol{f}$	Mechanistic dynamic model
G	Inlet mass flux into the reactor, kg/m^2/s
G_v	Specific syngas yield, Nm^3/kg biomass
$\boldsymbol{g}$	Inequality constraints
ΔH_j	Heat of reaction j, J/mol
$\boldsymbol{h}$	Output model
h_f	Heat transfer coefficient between bulk and oxygen carrier, W/m^2/K
h_w	Heat transfer coefficient between bulk gas and wall, W/m^2/K
K_j	Equilibrium constant for reaction j
$K_{j,i}$	Adsorption coefficient of species i, in reaction j, bar^{-1}
$k_{0,j}$	Arrhenius pre-exponential factor for reaction j m/s
$k_{c,i}$	Mass transfer coefficient of species i, m/s
k_j	Reaction rate coefficient of species j, m/s
L	Reactor length, m
MW_i	Molar weight of compound i, g/mol
$\dot{m}_i$	Consumption rate of species i, kg/m^3/s
N_i	Moles of gas i, mol
N_T	Total moles of gas, mol
N_{WP}	Weisz-Prater number
n	Avrami-Erofe'ev exponent
n_g	Number of gaseous species in the system
n_j	Reaction order for reaction j
n_r	Number of reactions taking place in the system

n_s	Number of solid species in the system
Pe_a	Axial Peclet number
P_i	Partial pressure of species i, Pa
P_{in}	Inlet pressure, bar
Pr	Prandtl number
Q	Inlet volumetric flowrate, m^3/s
$\boldsymbol{Q}$	Weighting matrix for deviations between predicted states and setpoint
Q_{net}	Combustion potential of biomass feedstock, MJ/kg
$\boldsymbol{R}$	Weighting matrix for changes in the manipulated variables
R_0	Oxygen carrying capacity
Re	Reynolds number
Re_p	Particle Reynolds number
R_g	Universal gas constant, J/mol/K
R'_g	Universal gas constant, $g \cdot m^2/(s^2 \cdot K \cdot mol)$
R_p	Particle radius, m
r_0	Particle grain radius, m
r_c	Radial domain, m
r_j	Reaction rate of reaction j, mol/m^3/s
S_0	Initial surface area, m^2/m^3
Sc	Schmidt number of gas
S_{CO2}	Selectivity of CO_2
T	Bulk temperature, K
T_{in}	Inlet gas temperature, K
T_c	Solid temperature, K
T_w	Temperature of the reactor wall, K
t	Temporal domain
t_c	Control horizon, s
t_f	Final time of the stage, s

t_p	Prediction horizon, s
$\Delta \boldsymbol{u}_{max}$	Maximum change of manipulated variables
$\hat{\boldsymbol{u}}$	Vector of control actions
V	Volume of gas, m³
v	Inlet gas velocity, m/s
X	Conversion of oxygen carrier
X_{char}	Conversion of char
$\boldsymbol{x}$	Vector of process states at the sampling time
$\hat{\boldsymbol{x}}$	Vector of predicted states
$\dot{\hat{\boldsymbol{x}}}$	Derivative vector for predicted states
$\boldsymbol{x}_{sp}$	Setpoint values for control variables
$Y_{CH4,TGA}$	Mass fraction of CH₄ in thermo-gravimetric analyzer experiments
Y_i	Mass fraction of species i
y_i	Mole fraction of component i
$y_{i,0}$	Inlet mole fraction of component i
z	Axial domain, scaled

Greek Symbols

α_j	Avrami exponent for reaction j
ε_0	Initial char porosity
ε_b	Porosity of bed
ε_c	Porosity of oxygen carrier
ε_s	Solid porosity
η_{gas}	Gasification efficiency
λ_{ax}	Effective axial thermal conductivity, W/m/K
λ_m	Thermal conductivity of the gas mixture, W/m/K
λ_{e0}	Static contribution to thermal conductivity, W/m/K
λ_i	Thermal conductivity of component i, W/m/K
λ_s	Weighted thermal conductivity of oxygen carrier, W/m/K

μ	Viscosity of gas, Pa·s
ρ	Mass density of gas, kg/m^3
ρ_c	Mass density of char, kg/m^3
ρ_m	Molar density, mol/m^3
ρ_s	Catalyst density, kg/m^3
v_j	Stoichiometric coefficient of reaction j
τ	Future time within the NMPC model
τ_p	Pore tortuosity

Chapter 1

Introduction

As the global energy demand increases, combustion processes remain integral to generate sufficient amounts of energy to satisfy this demand. Despite the growing prevalence of renewable energy, fossil fuel combustion accounted for 78% of the global energy supply in 2020 [1]. CO_2 is a combustion by-product that accounts for approximately 57% of the temperature increase due to global warming [2], which is driving research into sustainable combustion practices. As such, there is an increasing focus on developing feasible technologies to generate energy using sustainable fuels, as well as developing carbon capture techniques that allow for the continued use of fossil fuels to generate energy without emitting the resultant carbon dioxide into the atmosphere.

One process investigated for sustainable energy generation is chemical-looping (CL) technology. CL technology involves the addition of a solid oxygen carrier (OC) to processes such as gasification and combustion, leading to intensified technologies referred to as chemical-looping gasification (CLG) and chemical-looping combustion (CLC). In both cases, the OC provides an oxygen source while avoiding direct contact between the air and fuel. This prevents the generation of NO_x compounds and the dilution of the product gas, and mitigates the costs which would otherwise be incurred by using an air separation unit to isolate the oxygen [3] [4]. In CLG, this allows for the production of high-quality syngas while using the OC reactions to provide the energy needed for gasification; in CLC, this allows for energy generation with inherent carbon capture.

CLC was initially performed using fluidized bed reactors, but this requires an additional separation process to isolate the OC, which can be made very challenging due to the high temperatures

and pressures required for CLC. As an alternative, CLC has recently been investigated in packed beds; in this configuration, a single reactor is packed with the OC, removing the need for an additional separation process to recover the OC [5]. Packed bed CLC can also be performed at higher pressures, increasing the efficiency of the process; the main downside of packed bed reactors is that the reactor alternates between the oxidation and reduction stages, meaning that this configuration only intermittently generates energy [5].

Some works have developed models for packed bed CLC to assess the industrial feasibility of the process. Many works use multiscale models to represent the behaviour at both the reactor and particle scales. The interactions between the different scales increase the complexity of the system, making this model computationally expensive to solve. Consequently, some works have investigated pseudo-homogeneous models to approximate the process behaviour with reduced computational costs [6] [7] [8]. To the author's knowledge, none of these models have implemented a single kinetic scheme which was validated using experimental data from different reactor designs and operating conditions, and the use of a pseudo-homogeneous model to reduce computational costs has never been implemented in feedback control.

During the oxidation stage of this process, where the OC is exposed to air and produces heat, the hot outlet air can be sent to a downstream turbine to generate energy. Sudden changes in the outlet temperature could damage the downstream turbine [9]; thus, the implementation of a control scheme to mitigate this risk would be beneficial. However, during the oxidation stage, much of the heat generated is absorbed by the solid and accumulates within the packed bed reactor, making it difficult to control the outlet temperature [10] [11]. Furthermore, implementing control for the reduction stage (where the OC is regenerated through contact with fuel) can increase the CO_2 purity of the product

2

stream, thereby improving the carbon capture effectiveness of the process. Nonlinear model predictive control (NMPC) is a feedback control scheme which predicts the future dynamics in order to determine the optimal control actions to take at a given point in time. NMPC is particularly useful for this system because it can account for the predicted future dynamics, can be used for multivariable control, and can account for constraints of the process (e.g., operational safety constraints) [12]. Despite the potential benefits of implementing control schemes for CLC, to the extent of the author's knowledge, there are no existing studies performing feedback control for packed bed CLC, and no works implementing NMPC for the oxidation stage of CLC.

In addition, biomass, a renewable energy source, has recently been investigated as a fuel for energy generation because it is abundant, low-cost, and absorbs carbon dioxide while it grows [13] [14]. This reduces the carbon footprint of biomass-fueled energy generation, and means that when biomass-fueled energy generation is combined with a carbon capture process such as CLC, there is the potential for net negative CO_2 emissions [13] [14]. The main challenges associated with biomass-fueled CL are the reduced reactivity between the solid fuel and solid OC, and the increased generation of char. If large quantities of char are produced, the char will be deposited on the OC and subsequently react with air during the oxidation stage, which would produce CO_2 and diminish the carbon capture efficiency of the process [15] [16]. Nonetheless, because of the promising nature of biomass-fueled energy generation, some works have recently investigated the feasibility of using biomass as a fuel for CLG and CLC. These works found that biomass-fueled CL is feasible under certain operating conditions, for instance, by using a lower flowrate to increase the residence time of the fuel and by introducing a gasifying agent such as steam to increase the char conversion in the reactor [17] [18]. Furthermore, a few works have developed models representing biomass-fueled CL, which can be used

to investigate strategies to improve the gasification efficiency and outlet CO_2 purity of biomass-fueled CLG and CLC, respectively. However, to the author's knowledge, no works have been performed to study packed bed biomass-fueled CLC, and no reactor network models have been developed for packed bed biomass-fueled CL.

1.1 Research Objectives

The aim of this thesis is to determine reactor design and control strategies to improve the energy generation, gasification efficiency, and carbon capture effectiveness of packed bed CLC and CLG technology. First, the optimal control strategies for packed bed CLC are investigated by implementing NMPC for this process, increasing the energy generation and CO_2 purity of CLC. Then, reactor design strategies for packed bed CLG and CLC are investigated by using a reactor network model to explore different reactor designs for biomass-fueled CLG and CLC in PBRs. The objectives for this MASc thesis are listed below:

- Develop and validate multiscale and pseudo-homogeneous models that can provide accurate predictions of the oxidation and reduction stages for packed bed CLC using different reactor designs and operating conditions.

- Develop a strategy to control the outlet temperature for the oxidation stage of packed bed CLC by manipulating the inlet air and nitrogen streams.

- Implement NMPC for both the oxidation and reduction stages of packed bed CLC. In the oxidation stage, the outlet temperature will be controlled to increase the energy generation of this process; in the reduction stage, the CO_2 selectivity and outlet CO_2 flux will be controlled to improve the carbon capture effectiveness of CLC.

4

- Develop and validate a generalized reactor network to model biomass-fueled CLG and CLC in a PBR, which can be applied for various kinds of biomass fuel and different reactor designs.

- Use the reactor network to determine the most effective design to improve the syngas flowrate and gasification efficiency for biomass-fueled CLG, and to improve the product CO_2 and H_2O purity for biomass-fueled CLC.

1.2 Outline of Thesis

This thesis is structured as follows:

Chapter 2: This chapter presents an overview of the literature available for chemical-looping combustion and chemical-looping gasification, including a description of the technology, a summary of relevant works investigating biomass-fueled CL, and literature pertaining to the implementation of control schemes for CLC. The gaps in literature which motivate this thesis are presented in more detail in this chapter.

Chapter 3: This chapter presents a multiscale model for packed bed CLC and proposes an NMPC scheme for this process. The model is validated and used to implement NMPC for both the oxidation and reduction stages of CLC. Different scenarios are investigated by varying the inlet gas and NMPC objectives. The results show that the outlet temperature in the oxidation stage can be controlled by manipulating the inlet air and inert gas fluxes, and that the CO_2 selectivity and outlet CO_2 flux in the reduction stage can be controlled by manipulating the inlet methane flux. The outcomes of this chapter have been submitted to a journal for publication.

Chapter 4: This chapter presents a reactor network model for biomass-fueled CLG and CLC. The model is validated against data from both CLG and CLC processes. The location and length of the

5

OC bed within the reactor network is varied in different scenarios to investigate the resulting effect on the performance of CLG and CLC. The results show that the highest gasification efficiency for CLG can be obtained using an OC/biomass ratio of 0.25, a steam/biomass ratio of 1, and by keeping the OC near the reactor inlet. Furthermore, the highest CO_2 and H_2O purity for CLC can be obtained when the reactor is fully packed with OC and steam is used as the inlet gas. The outcomes of this chapter have been submitted to a journal for publication.

Chapter 5: In this chapter, conclusions from this work are presented, and potential avenues for future work are proposed.

Chapter 2

Background and Literature Review

This chapter presents an overview of the current literature and gaps in existing literature pertaining to CLC and CLG processes. Section 2.1 presents an overview of existing carbon capture technology, and Section 2.2 outlines the principles behind chemical-looping combustion and gasification. Section 2.3 discusses the use of biomass as a fuel for this process and highlights relevant literature pertaining to biomass-fueled CL. Section 2.4 outlines the motivation for implementing a control scheme in CLC, and provides an overview of existing literature in this field. Finally, Section 2.5 presents a summary of this chapter.

2.1 Carbon Capture

To mitigate the effects of climate change, carbon capture and sequestration (CCS) and carbon capture, utilization and storage (CCUS) technologies have become increasingly widespread. In both of these technologies, the aim is to reduce the quantity of CO_2 emitted into the atmosphere. In CCS, the carbon dioxide is captured and can be stored in a geological site – for instance, injected in depleted oil reservoirs, abandoned gas fields, or deep saline aquifers [19]. CCUS also reduces CO_2 emissions, but has a greater focus on utilizing carbon dioxide to achieve different goals. To this end, the CO_2 will be injected into an active reservoir to enhance the recovery of a fuel, such as oil or gas [20]. Additionally, if the CO_2 is isolated into a sufficiently pure stream, it can be sold for use as a reactant in a manufacturing process. In all of the cases described, the captured carbon dioxide stream should be highly concentrated, to make more effective use of the space in the reservoirs or to ensure that the CO_2 is sufficiently pure for manufacturing.

To perform CCS and CCUS, carbon capture technology must be incorporated into processes that generate CO_2 as a byproduct. Different carbon capture technologies are usually classified as pre-combustion, post-combustion, and oxyfuel techniques, and each approach has different benefits and drawbacks. Post-combustion carbon capture is the most mature method; the fuel is burned, and the product gas is subject to a treatment process such as absorption or stripping in order to remove the CO_2 from the stream [21]. Post-combustion carbon capture can maintain high efficiency for the energy generation process, but the additional equipment required for the separation process increases the capital cost of the plant [19]. In pre-combustion carbon capture technologies, the fuel undergoes gasification prior to combustion, and a solvent is used to separate the CO_2 from the product gas. This results in a relatively pure hydrogen stream which can fuel a combustion process to generate energy without producing carbon dioxide. In pre-combustion carbon capture, the solvent can be regenerated by changing the pressure and does not require heat, which is less energy-intensive; however, burning the hydrogen for energy is less efficient than traditional combustion of the fuel [19]. Furthermore, in oxyfuel technologies, the oxygen is separated from the nitrogen in air so that it can be burned to generate a nitrogen-free product stream [19]. Oxyfuel carbon capture is promising as the carbon dioxide is inherently generated into a purer stream and thus does not require subsequent CO_2 separation. However, using an air separation unit to isolate the oxygen from air can be very expensive [21].

Recently, technologies known as chemical-looping gasification and chemical-looping combustion have been investigated for energy generation. Chemical-looping technology involves the addition of a metal oxide known as an oxygen carrier to provide the oxygen source, granting the same benefits as oxyfuel carbon capture without incurring the costs of an air separation unit [3] [4]. This technology is discussed in more detail in the following section.

2.2 Chemical-Looping Technology

Chemical-looping technology refers to energy generation technologies where an oxygen carrier is added to provide the oxygen required to burn the fuel – thus avoiding any direct contact between the air and fuel. This inherently avoids diluting the product gas and producing NO_x compounds, without incurring the costs of an air separation unit [3] [4]. The addition of an OC effectively splits the combustion process into two stages: the oxidation stage, where the OC reacts with the oxygen in the air stream and produces heat, and the reduction stage, where the OC is regenerated by a fuel source [3]. In CLG, the goal is to produce high-quality syngas during the reduction stage, whereas the oxidation stage is used to heat the OC and provide the energy needed for the gasification [22]. In CLC, the aim is to generate energy with inherent carbon capture. To accomplish this, hot air is produced during the oxidation stage that can be used to power a downstream turbine. Then, the OC is regenerated by a fuel source during the reduction stage, producing CO_2 as a by-product. Because the fuel and air streams are kept separate, the product stream mainly consists of carbon dioxide and steam. Hence, the CO_2 can be easily isolated without an energy-intensive separation process, similar to oxyfuel carbon capture [15] [23]. CLG and CLC are schematically depicted in Figure 2.1 and Figure 2.2, respectively.
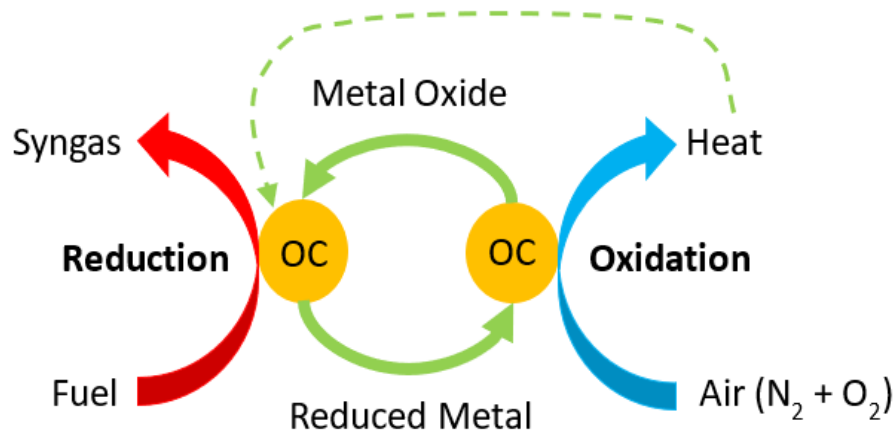
Figure 2.1. Schematic depicting the reactants and products in the oxidation and reduction stages in CLG.
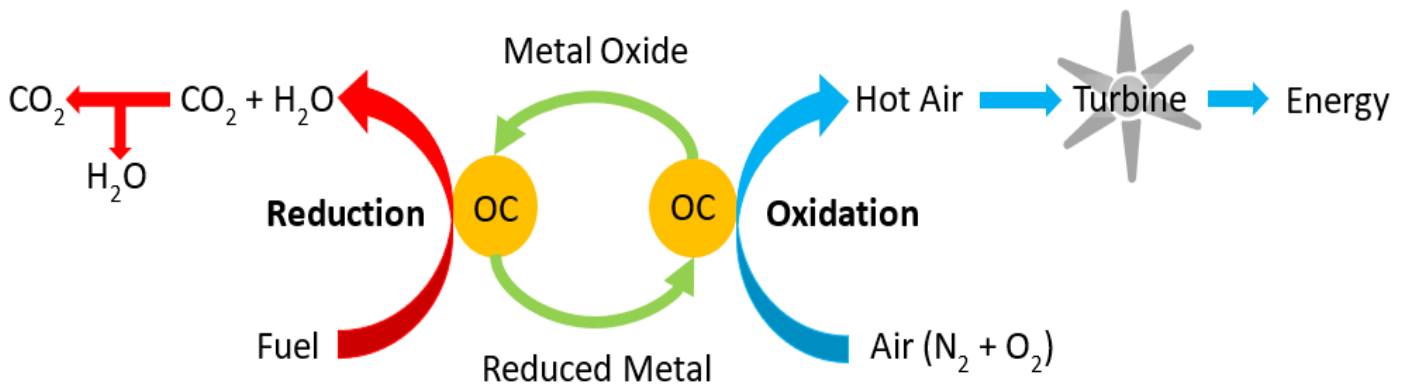
Figure 2.2. Schematic depicting the reactants and products in the oxidation and reduction stages in CLC.

Various works have been performed to investigate the feasibility of this technology. Ishida et al. [3] coined the term "chemical-looping combustion" and initially performed lab-scale experiments using a nickel-based oxygen carrier with interconnected fluidized bed reactors, determining that Ni-based OCs showed good reactivity for the system and maintained their structural integrity after 5 hours of continuous operation [3] [24]. This work was expanded by the Grangemouth Advanced CO_2 Capture

10

Project (GRACE project), which tested over 300 types of metal oxide OCs and investigated various operating conditions for feasible operation of CLC in fluidized beds at a pilot scale [25].

To attain higher temperatures and pressures during operation of CLC, Noorman et al. [10] proposed CLC using packed bed reactors, which is discussed in further detail in Section 2.2.1. They performed lab-scale experimental validation, using copper-based OCs and methane as a fuel. In this experiment, Noorman et al. determined that the change in temperature during the oxidation stage was large enough for energy generation, and observed good selectivity in the conversion of CH_4 to CO_2 during the reduction stage [26]. Jin et al. [27], Hamers et al. [28], and Spallina et al. [29] further examined the feasibility of packed bed CLC using nickel-based OCs at various conditions, confirming that Ni-based oxygen carriers continue to be promising OCs when employed using packed bed conditions. Spallina et al. [9], Han et al. [30], and Chen et al. [31] have performed simulations to investigate the feasibility of large-scale packed bed CLC, but to the author's knowledge, no experimental studies have been performed to verify whether large-scale CLC in a PBR would be feasible for implementation.

In recent years, solid fuels such as coal and biomass have been investigated for CL [32] [15]. With solid fuels, CL was often implemented as chemical-looping gasification, with the aim of introducing an oxygen carrier to enhance the gasification of a solid fuel. Fan et al. [33] added an iron-based OC to enhance the coal gasification process, implementing fluidized bed CLG, and observed that CL could increase the efficiency of the product generation compared to standard gasification. As biomass-fueled processes gained interest, CLG was also implemented using biomass as a fuel, discussed in further detail in Section 2.3. Some lab-scale experimental works, such as those implemented by Liu et al. [18] and Nguyen et al. [34], verified that adding an OC to biomass gasification to perform biomass-fueled CLG could improve the gasification efficiency of the process.

2.2.1 Reactor Types

CL was initially conceptualized using interconnected fluidized bed reactors [3]. In this configuration, the oxygen carrier is cycled between an air reactor, where the OC is oxidized, and a fuel reactor, where the OC is reduced. This configuration allows for the oxidation and reduction stages to occur simultaneously in different reactors, which can produce a continuous stream of hot air. However, to transfer the OC from one reactor to the other, a cyclone is required to separate the OC from the gas, which is made particularly difficult due to the high temperatures and pressures used in this process. In addition, CLC operation is more efficient at higher pressures, but high pressures interfere with the circulation of OC between the beds [10].

To avoid these issues, CL in a packed bed reactor (PBR) has been investigated. In this configuration, the OC is packed into a single reactor, and the air and gas are alternatingly introduced to the reactor. The greatest advantage of using a PBR for CL is that it avoids the need for an additional separation process to recover the OC, further employing process intensification to the CL system [10] [5] [35]. Additionally, packed bed technology inherently allows for a more compact reactor which can operate at higher pressures, improving the efficiency of the combustion process. A PBR can increase the extent of the redox reactions taking place, more effectively utilising the OC; the main drawback of packed bed CL is that hot air is not produced during the reduction or purge stages, meaning that this configuration only intermittently generates heat [10].

To address this, Spallina et al. investigated reactor design and operation strategies for a syngas-fueled power plant using packed bed reactors and determined that 14 reactors could be scheduled to consistently generate energy, dedicating 7 units at any point in time to the heat recovery phase [9]. Chen et al. investigated a simulated moving bed process where the inlet and outlet ports in a semibatch reactor are switched to simulate countercurrent solids and fuel movement, and presented a configuration

using 6 reactor trains, where 3 reactor trains would simultaneously undergo heat recovery [31]. In both of these schemes, half of the available units would undergo heat recovery at a given point in time, allowing a plant to produce a consistent stream of hot air for the turbine and maintain an efficient combustion process.

2.2.2 Oxygen Carriers

For CL processes, various metals have been investigated for use as the OC. An OC should exhibit various properties for effective CLG or CLC. An effective oxygen carrier is sufficiently reactive in both the oxidation and reduction stages, and for CLC, the OC must favour the production of CO_2 and H_2O during the reduction reaction for effective carbon capture. Additionally, the OC should have a high oxygen transport capacity, to reduce the quantity of OC needed for the process. It must have a sufficiently high melting point, to withstand the high temperatures achieved during the oxidation stage, and be resistant to attrition to maintain its reactivity over multiple CL cycles. Finally, the OC should be low-cost and have low environmental impact, for economic feasibility and long-term sustainability [15] [36]. The most common metals used for this process are Ni-, Cu-, Fe-, and Mn- based, each presenting different advantages and challenges [15].

Nickel is a promising oxygen carrier due to its fast kinetics and ability to perform well at high temperatures [37]. At the temperatures frequently used for CLC (900-1100°C), Ni-based OCs have good selectivity to producing CO_2 and H_2O, and demonstrate good resistance to attrition [15] [37]. The main limitations of nickel OCs are that it is toxic, and that Ni-based OCs are one of the most expensive oxygen carriers [15] [36].

Copper-based oxygen carriers also exhibit high reactivity, and the reduction mechanism of CuO makes copper-based OCs particularly desirable for the combustion of solid fuels. At high temperatures,

CuO undergoes an oxygen uncoupling reaction, which releases the oxygen to react independently with the fuel. This increases the rate of reaction of CL using a solid fuel, as it allows for the fuel to react through gas-solid contact, instead of via solid-solid interactions [15]. However, copper has a relatively low melting point, which can cause the particles to agglomerate and lose their reactivity when exposed to the high temperatures undergone in CLC [15] [36].

Iron-based oxygen carriers are inexpensive, non-toxic, and there are many iron-based ores abundantly found in nature, making iron-based OCs attractive for sustainable CL processes. Fe-based OCs have demonstrated sufficient reactivity for CL, although they are less reactive than Ni- and Cu-based OCs and produce higher quantities of CO and H_2 as byproducts [37].

Similar to Fe-based OCs, manganese-based oxygen carriers are attractive due to their low cost and non-toxicity. However, they exhibit lower reactivity than Ni- and Cu-based OCs, particularly when methane is used as the fuel [15] [37].

In addition to the metals listed above, certain natural metallic ores have been gaining attention as promising oxygen carriers. These materials are promising oxygen carriers due to their low cost, abundance, and sustainability. Ilmenite, an abundant iron-based ore, has been used in many CLC studies [15] [38] [39]. Although ilmenite has low reactivity compared to purified metal oxides, its low cost and good structural stability make it an attractive OC [15]. Other iron ores, such as natural hematite and Tierga ore, are also popular due to their low cost and good reactivity compared to other metal ores [16] [17].

2.3 Biomass-Fueled CL Technology

Biomass, a renewable energy source, is a particularly promising fuel as it is abundant, low cost, and absorbs carbon dioxide as it grows [13] [14]. Because of this, when a biomass-fueled combustion

process is combined with a carbon capture process such as CLC, there is the potential to achieve net-negative carbon emissions while still generating heat to satisfy global energy demands [15]. This has been driving interest in biomass-fueled CL technology, including biomass-fueled CLG and biomass-fueled CLC.

In current literature for biomass-fueled chemical-looping, there is a greater focus on CLG than on CLC. Several experimental studies have been performed to verify the feasibility of biomass-fueled CL. Huang et al. [17] and Nguyen et al. [34] investigated biomass-fueled CLG in a fluidized bed and found that adding iron-based OCs to the process enhances carbon conversion and improves the syngas yield. Mendiara et al. [16] performed biomass-fueled CLC in a fluidized bed, and determined that it was a promising biomass carbon capture process. Some works, such as those performed by Liu et al. [18] and Al-Qadri et al. [40] have also examined biomass-fueled CLG in fixed bed reactors and confirmed that hematite is a viable OC for syngas generation through CLG.

To gain insight into the optimal operating conditions for the process, as well as to develop tools that can aid in ascertaining the feasibility of industrial-scale biomass-fueled chemical-looping processes, various models have been developed. Many of these studies have used Aspen Plus as a simulation tool. For instance, Kevat et al. [41] and Zhou et al. [42] developed Aspen Plus models for biomass-fueled CLC, using ideal reactor blocks to model biomass-fueled CLC in fluidized beds. Ohlemüller et al. [43] also used Aspen Plus to model fluidized bed CLC with a coal-fueled process, and incorporated custom calculator blocks to calculate the conversion rates of the coal and of the OC. Furthermore, Gopaul et al. [44] developed an Aspen Plus model for biomass-fueled CLG in a fluidized bed reactor, again using ideal reactor blocks.

A limited number of works have also investigated mechanistic models for biomass-fueled CL. Li et al. [45] and Du et al. [46] performed computational fluid dynamic simulations for biomass-fueled chemical-looping combustion in fluidized beds. Likewise, Yin et al. [47] and Dong et al. [48] carried out computational fluid dynamic simulations for fluidized bed biomass-fueled chemical-looping gasification. Recently, Li et al. developed a mechanistic model that could simulate the behaviour of biomass-fueled CLG in a fixed bed reactor [49]. However, to the author's knowledge, no mechanistic models have been used to investigate the feasibility of biomass-fueled CLC in a PBR; also, no modelling studies have utilized an equivalent reactor network to represent packed bed biomass CL. This thesis aims to address these gaps in Chapter 4.

2.4 CLC Modelling and Control Schemes

Multiple works have developed models for CLC processes in fluidized beds. Porrazzo et al. [50] developed an Aspen Plus model for CLC in a bubbling fluidized bed, using a reactor network to represent the emulsion and bubble phases in this system. Furthermore, Lin et al. [51] and Chein et al. [52] built CFD models to simulate fluidized bed CLC, investigating the effect of different operating conditions to improve the reactor performance.

In addition to the modelling works performed for fluidized bed CLC, some studies investigate the implementation of feedback control to improve the system's energy generation and outlet CO_2 purity. Fan et al. [53] and Wanotayaroj et al. [54] modelled a circulating fluidized bed CLC system using Aspen Dynamics and implemented proportional-integral-derivative (PID) control to control the system in the presence of disturbances. However, to the author's knowledge, no works have implemented NMPC for the control of these systems.

There have also been several works which presented models to represent packed bed CLC. Noorman et al. [10] presented a dynamic PBR model for packed bed CLC using a copper-based OC. The same authors expanded on this homogeneous model to develop a more detailed multiscale model representing the process [5] [35], although the multiscale model is considerably more complex and thus more computationally expensive to solve. Han et al. [6] [7] presented similar homogeneous and heterogeneous dynamic models for packed bed CLC in a reactor packed with a nickel-based OC. These models provide tools which can be used to assess the industrial feasibility of the process, as well as to implement control schemes to improve the performance of CLC.

Due to the high kinetic rates of the oxidation reactions in CLC, the peak temperature in packed bed CLC can be very difficult to control throughout the heat recovery phase. As the air is introduced to the reactor and reacts with the OC, much of the heat is transferred to the solid and accumulates in the reactor bed. As such, the reaction front progresses much more quickly than the heat front, which gradually moves to the outlet (depicted in Figure 2.3). During CLC, sudden changes in the outlet temperature could damage the downstream turbine [9]; this can be regulated by implementing a suitable control scheme. Changing the air flowrate can increase the speed at which the heat front reaches the outlet, but has a minimal impact on the outlet temperature itself. Regulating the temperature in CLC is more commonly achieved through changing the concentration of active material on the OC [10]. Therefore, for metals with fast reaction rates (e.g. nickel-based OCs), the concentration of active metal on the OC is kept low, often less than 20%, to avoid high temperatures which could damage the OC or the reactor itself. Fernández et al. [11] investigated this phenomenon and determined that the maximum temperature could be regulated by diluting the inlet air stream with an inert gas. Diluting the air reduces the concentration of O_2 being supplied to the reactor and slows the reaction front relative to the heat front, making it possible to control the temperature by manipulating the inlet flowrates.
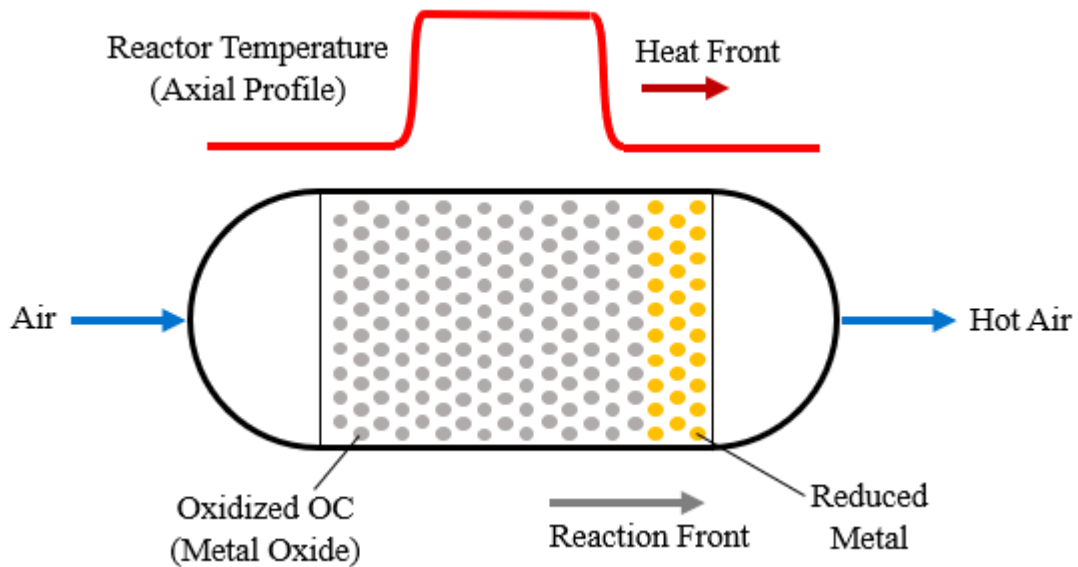
Figure 2.3. Schematic depicting the reaction and heat fronts in the oxidation stage of packed bed CLC.

In existing studies, both experimental and simulation-based, packed bed CLC has been widely investigated using constant inlet flowrates for each stage. Experimental studies for packed bed CLC, such as those performed by Jin et al. [27], Hamers et al. [28], and Spallina et al. [29], typically use a constant inlet air flowrate during the oxidation stage, and a constant inlet fuel flowrate for reduction. Similarly, in modelling works, such as those performed by Noorman et al. [10] and Han et al. [6] [7] the simulations are typically performed using a constant flowrate for the entire duration of a given stage. However, using constant flowrates do not allow a system to respond to disturbances or changes in the dynamics – for instance, changes in the reaction rate as the OC reaches complete conversion. Using dynamic inlet flowrates manipulated by a control scheme would address these issues and make it possible to regulate the high temperatures generated in this process. If the reactor temperature of the oxidation stage is controlled in this way, more efficient design configurations can be used without damaging the reactor or OC. For instance, if the temperature is moderated, a more concentrated oxygen

carrier – and consequently, a more compact reactor – can be used without reaching temperatures that could damage the equipment. In addition, the outlet composition of the reduction stage can be controlled to ensure that the product stream contains highly concentrated CO_2.

Using the models described previously, Han et al. [30] and Spallina et al. [9] [55] recently investigated optimal operation strategies for CLC in PBRs while maintaining constant conditions for each stage of the process. More recently, Lucio et al. [56] and Toffolo et al. [57] investigated dynamic control profiles for packed bed CLC. Moreover, Parker et al. [58] investigated nonlinear model predictive control (NMPC) of a moving bed CLC reactor. In their work, Parker et al. manipulated the inlet OC and methane flowrates to the moving bed reactor to control the outlet compositions and OC conversion during the reduction stage. To the extent of the author's knowledge, there have been no similar studies performing feedback control such as model predictive control (MPC) for chemical-looping combustion in a packed bed reactor, and no studies implementing MPC for the oxidation stage of CLC.

In the oxidation stage of packed bed CLC, the heat front progresses through the reactor relatively slowly. Because of this, changing the inlet flowrate will have a delayed impact on the outlet temperature, making it important to consider the future behaviour while implementing control actions [10]. In addition, to control the outlet temperature, it is necessary to manipulate both the inlet air and inert gas flowrates [11]; in the reduction stage, it is beneficial to control several variables (e.g., the CO_2 selectivity and outlet CO_2 flux) to optimize the CO_2 purity while ensuring that the oxygen carrier is regenerated quickly. To address this, nonlinear model predictive control (NMPC) is chosen because it accounts for predicted future dynamics and can be used for multivariable control. NMPC is additionally useful in that it can handle system constraints, ensuring that processes operate within safe bounds, like a defined temperature range [12].

To the author's knowledge, there is no existing literature for packed bed CLC which employs a single kinetic scheme that has been validated against multiple sets of experimental data using different reactor designs and operating conditions. Furthermore, no works have performed feedback control for packed bed CLC, and no studies have used a pseudo-homogeneous model to reduce computational costs for online application of control. In Chapter 3 of this thesis, NMPC is implemented for packed bed CLC to address these gaps and investigate control strategies to improve the performance of CLC.

2.5 Summary

This chapter presented an overview of relevant works for CL processes. In the first two sections, carbon capture technologies were introduced, and chemical-looping gasification and combustion were described. In the following sections, relevant studies for biomass-fueled CL and the control of CLC were outlined. The results of this literature review revealed that using biomass as a fuel for CL is a promising but relatively new technology, and few existing simulation studies have been performed to assess the most effective design and operating conditions. In addition, it was found that the feasibility of packed bed CLC could be improved through the implementation of a control scheme, but very few works have implemented feedback control for CLC. Thus, this literature review revealed that there are gaps in the literature concerning biomass-fueled CL processes, since there are no works investigating biomass-fueled CLC in a PBR, and only one study that developed a mechanistic model for packed-bed biomass-fueled CL. Furthermore, this literature review found that there are gaps in the literature concerning the implementation of NMPC for CLC, as no works were found which performed MPC for both stages of CLC. In the next section, a multiscale model for CLC is presented, and an NMPC scheme is proposed to improve the feasibility of this process.

Chapter 3

NMPC for Large-Scale Packed Bed CLC

This chapter presents a multiscale model for packed bed CLC, as well as an NMPC framework used to determine the optimal operation strategies for the oxidation and reduction stages. Section 3.1 describes the packed bed reactor model and the corresponding kinetic scheme for CLC with a nickel-based OC. Section 3.2 outlines the NMPC framework, as well as the pseudo-homogeneous model used as the internal NMPC model to reduce computational costs. Section 3.3 presents the results of this work; Section 3.3.2 shows the validation of the oxidation and reduction stages of the model, and in Section 3.3.3, NMPC is implemented for both the oxidation and reduction stages. The outcomes of this chapter have been submitted for publication in a journal.

3.1 Packed Bed Chemical-Looping Combustion Model Description

In packed bed CLC, a single reactor is packed with an oxygen carrier and cyclically exposed to different gases, shown in Figure 3.1. Air is introduced to the system to oxidize the OC, and then the reactor is purged with an inert gas before introducing fuel to the reactor, and purged again before air is added to the reactor once more. In the oxidation stage, when air is introduced to the reactor, hot air is produced by the exothermic reaction and can be sent to a downstream turbine to generate electricity. During the reduction stage, the OC is regenerated by exposing the metal oxide to a fuel source, producing CO_2 as a by-product. As the reduction stage takes place in the absence of air, the outlet stream primarily consists of CO_2 and H_2O. Steam can be removed from the outlet gas via condensation, resulting in a relatively pure CO_2 stream without the need for an additional carbon capture process, effectively employing process intensification [4] [3].
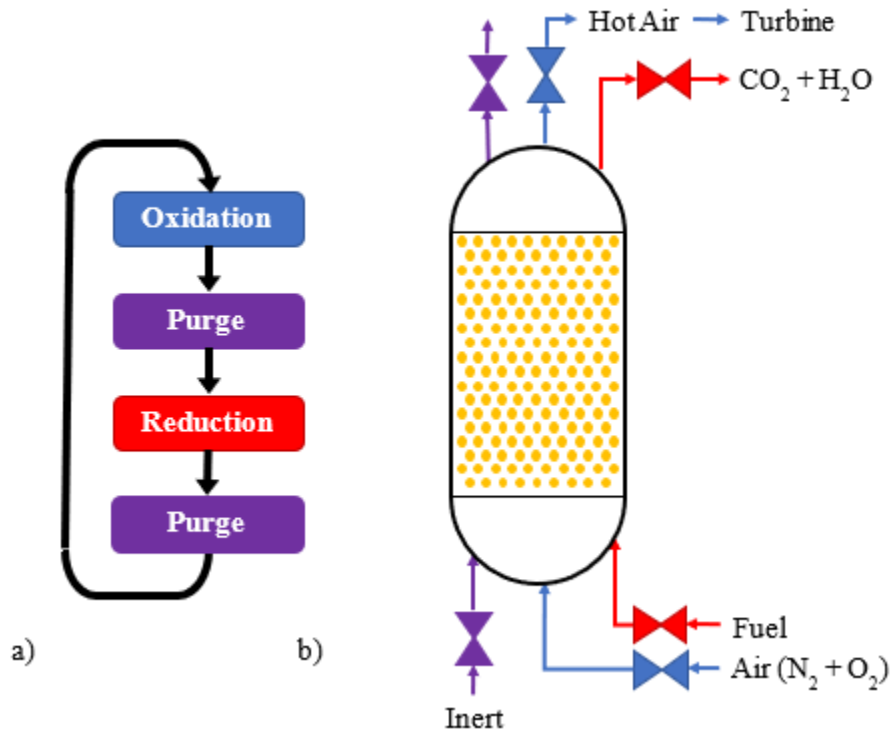
Figure 3.1. Diagram of a) the stage sequence for a reactor in a packed bed CLC process and b) the corresponding inlet and outlet gases of the different stages in a packed bed chemical looping combustion process, where blue denotes the oxidation stage, red denotes the reduction stage, and purple denotes the purge stages.

Within the PBR, there are two different scales considered: the macroscale reactor, and the microscale oxygen carrier. This is considered to be a multiscale system since the phehomena taking place in the oxygen carrier (microscale) needs to be coupled with the overall operation of the reactor (macroscale). There have been few studies regarding coupled multiscale models, as the interactions between the two scales lead to complex nonlinear behaviour with a large number of variables, resulting in high computation costs [59]. However, as the microscale behaviour influences the macroscale events, it is critical to account for the behaviour at both scales to develop a comprehensive model that accurately represents the system [35]. The multiscale model developed in this work is presented next.

3.1.1 Multiscale Packed Bed Reactor Model
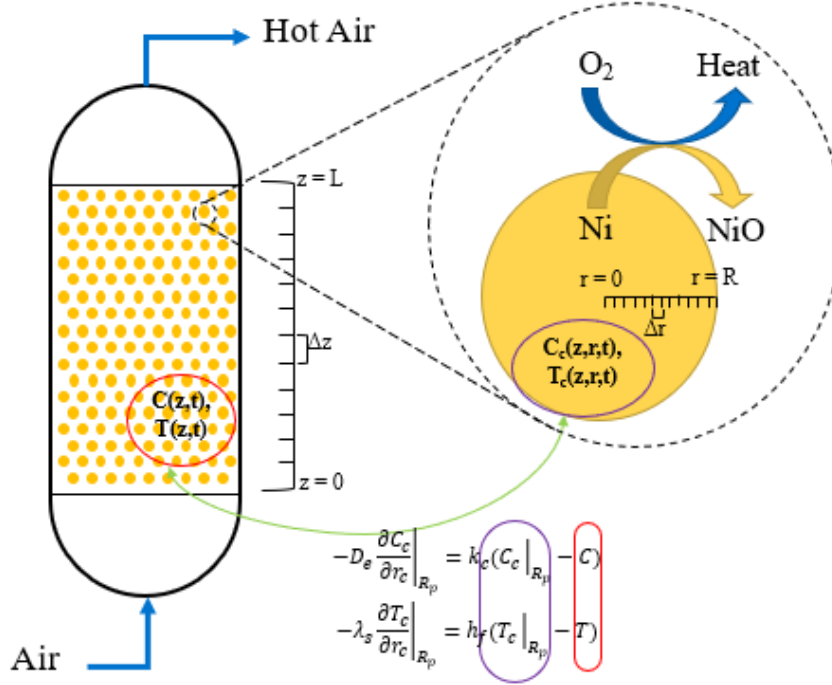
Figure 3.2. Multiscale interactions between the macroscale gas and microscale OC in the oxidation stage of packed bed CLC due to heat and mass transfer at the particle surface. In this diagram, the states circled in red represent the macroscale reactor states, and the ones circled by purple show the microscale particle states (enlarged in the dashed circle). The reaction between Ni and O_2 is shown at the particle scale, and the interactions between both scales at the particle surface are represented with the green arrow.

In this work, a dynamic multiscale model is used to represent the packed bed CLC process, adapted from the models used by Han et al. [6] and Lucio et al. [56]. The model considered in this work uses the same modelling principles presented by those works, but introduces kinetic schemes from different sources to develop a comprehensive multiscale model that can predict the behaviour for multiple PBR designs under different operating conditions. The present multiscale model accounts for the behaviour on two scales: the macroscale reactor model, which considers the axial transport of the bulk gas through the PBR, and the microscale particle model, which accounts for the reaction and

diffusion taking place within the OC (Figure 3.2). Multiscale models must also consider the behaviour at different temporal and spatial scales, which can significantly increase the computational costs.

In order to build the proposed multiscale model, the following assumptions are considered:

- The feed stream is perfectly distributed throughout the reactor diameter

- The gas velocity is constant across the reactor's spatial domain

- The active metal is evenly spread across perfectly spherical OCs

- The particles are uniformly distributed through the PBR

- The macroscopic structure of the OC is uniform and is not affected by the reactions taking place

- The gas at any point within the particle is at the same temperature as the particle itself

- The thermal conductivity of the gas is negligible compared to that of the OC

- There is negligible heat loss through the reactor walls

The proposed multiscale model is comprised of a set of partial differential equations (PDEs) representing the mass and energy balances at both scales. These PDEs, as well as the associated boundary conditions, are presented in Table 3.1.

Table 3.1. Mass and energy balances at the reactor-scale and particle-scale for the multiscale packed bed CLC model.

Reactor Mass and Energy Balances		
Mass Balance	$\varepsilon_b \dfrac{\partial C_i}{\partial t} + \dfrac{\partial F_i}{\partial V} = \dfrac{\partial}{\partial z}\left(D_{axi}\dfrac{\partial C_i}{\partial z}\right) + k_{c,i}a_v(C_{c,i}\vert_{R_p} - C_i)$	(3.1)
Energy Balance	$\varepsilon_b C_{pf} C_T \dfrac{\partial T}{\partial t} + C_{pf} F_T \dfrac{\partial T}{\partial V} = \dfrac{\partial}{\partial z}\left(\lambda_{ax}\dfrac{\partial T}{\partial z}\right) + h_f a_v(T_c\vert_{R_p} - T)$	(3.2)

Dankwerts Boundary Conditions	$\varepsilon_b D_{ax,i} \dfrac{\partial C_i}{\partial z}\bigg|_{z=0} = (F_i|_{z=0} - y_{i,feed}F_{in})/A_c$	(3.3)
	$\varepsilon_b \lambda_{ax} \dfrac{\partial T}{\partial z}\bigg|_{z=0} = (T_c|_{z=0} - T_{in})C_{pf}F_T/A_c$	(3.4)
	$\dfrac{\partial C_i}{\partial z}\bigg|_{z=L} = \dfrac{\partial T}{\partial z}\bigg|_{z=L} = 0$	(3.5)
Particle Mass and Energy Balances		
Mass Balance	$\varepsilon_c \dfrac{\partial C_{c,i}}{\partial t} = \dfrac{1}{r_c^2}\dfrac{\partial}{\partial r_c}\left(D_{e,i}r_c^2\dfrac{\partial C_{c,i}}{\partial r_c}\right) + \varepsilon_c\rho_s\sum_{j=1}^{n_r} r_{i,j}$	(3.6)
Energy Balance	$\left((1-\varepsilon_c)\rho_s C_{ps} + \varepsilon_c C_{pc}C_T\right)\dfrac{\partial T_c}{\partial t} = \dfrac{\lambda_s}{r_c^2}\dfrac{\partial}{\partial r_c}\left(r_c^2\dfrac{\partial T_c}{\partial r_c}\right) + \varepsilon_c\rho_s\sum_{j=1}^{n_r}(-\Delta H_j)r_j$	(3.7)
Mass and Heat Transfer Between the Particle and Reactor	$-D_{e,i}\dfrac{\partial C_{c,i}}{\partial r_c}\bigg|_{R_p} = k_{c,i}(C_{c,i}|_{R_p} - C_i)$	(3.8)
	$-\lambda_s\dfrac{\partial T_c}{\partial r_c}\bigg|_{R_p} = h_f(T_c|_{R_p} - T)$	(3.9)
Particle Symmetry	$\dfrac{\partial C_{c,i}}{\partial r_c}\bigg|_{r_c=0} = \dfrac{\partial T_c}{\partial r_c}\bigg|_{r_c=0} = 0$	(3.10)

In these equations, t represents the time ($0 \leq t \leq t_f$, where t_f is the end time of the oxidation or reduction stage), z is the position in the axial bed ($0 \leq z \leq L$, where L is the reactor length), and r_c represents the radial position in the particle ($0 \leq r_c \leq R_p$, where R_p is the particle radius). These equations predict the behaviour for both the oxidation and reduction stages for each component, i, in the stage (O_2 and N_2 for the oxidation stage; CH_4, H_2, CO, CO_2, H_2O, and N_2 for the reduction stage).

As shown in Table 3.1, Equations 3.1 and 3.2 represent the mass and energy balances for the reactor model, and consider the convection, axial dispersion, and mass and heat transfer with the

particle. Equations 3.3-3.5 denote the Dankwerts boundary conditions, which are the most widely used boundary conditions for packed beds [60]. The particle mass and energy balances are represented by Equations 3.6 and 3.7, respectively, and account for the diffusion and reaction taking place within the particle. Equations 3.8 and 3.9 represent the mass and heat transfer between the particle and the bulk scale reactor, and Equation 3.10 accounts for the symmetry of the radial gradients about the center of the particle. The reactor and particle scales interact at the particle surface; at the reactor scale, this is represented by the terms for heat and mass transfer with the particle surface (Equations 3.1 and 3.2), and at the particle scale, this is represented by the boundary conditions which account for the transfer with the bulk gas (Equations 3.8 and 3.9). Additional details pertaining to the model, including the parameter values and algebraic equations representing the additional correlations, can be found in Appendix A.

3.1.2 Kinetics

In this work, Al_2O_3-supported NiO is used as the oxygen carrier, and CH_4 is used as the fuel. This OC was chosen due to its fast kinetics, high CH_4 conversion, and durability when subjected to multiple CLC cycles [15] [37] [61] [62]. In order to develop a model that accurately predicts the packed bed CLC process under a variety of different conditions (e.g. different reactor designs and inlet flowrates), a kinetic scheme was proposed in this work such that the model is consistent with experimental data from multiple sources. The corresponding reactions and kinetic correlations, presented in Table 3.2, were directly obtained from works which investigated the reaction kinetics, i.e., no model fitting was performed. The oxidation reaction undergone by Ni is presented in R3.1, whereas the reduction reactions are listed in R3.2-R3.5. In addition, equilibrium reactions must be accounted for during the reduction stage as the products react with each other; the steam-methane reforming (SMR) and water-gas shift (WGS) reactions are presented in R3.6 and R3.7, respectively [6] [63].

Table 3.2. Kinetic rate equations for the oxidation and reduction reactions in CLC with a nickel-based catalyst.

	Reaction Stoichiometry		Reaction Kinetics	
Rate of OC Conversion			$$\frac{dX}{dt} = \frac{\sum_{j=1}^{n_r} \nu_j r_{Ni,j}}{C_{Ni,0}}$$	(3.11)
Oxidation Stage	$2Ni + O_2 \rightarrow 2NiO$	(R3.1)	$$r_1 = \frac{a_0}{P_{in}^{1.02}} k_1 (1-X)^{2/3} C_{O_2} C'_{Ni,0}$$	(3.12)
Reduction Stage	$CH_4 + 2NiO \rightarrow$ $2Ni + CO_2 + 2H_2$	(R3.2)	$$r_2 = a_0(1-X)(2k_2)C_{CH4}C_{NiO}C_{Ni}$$	(3.13)
	$CH_4 + NiO$ $\rightarrow Ni + CO + 2H_2$	(R3.3)	$$r_3 = \frac{a_0 k_3}{P_{in}^{1.01}} n(1-X)(-\ln(1-X))^{1-\frac{1}{n}} C_{CH_4} C'_{NiO,0}$$	(3.14)
	$H_2 + NiO$ $\rightarrow Ni + H_2O$	(R3.4)	$$r_4 = a_0(1-X)(k_4)C_{H_2}C_{NiO}$$	(3.15)
	$CO + NiO$ $\rightarrow Ni + CO_2$	(R3.5)	$$r_5 = \frac{a_0 k_5}{P_{in}^{1.21}} nX(1-X)(-\ln(1-X))^{1-\frac{1}{n}} C_{CO} C'_{NiO,0}$$	(3.16)
	$CH_4 + H_2O$ $\leftrightarrow 3H_2 + CO$	(R3.6)	$$r_6 = \frac{k_6\left(P_{CH_4}P_{H_2O} - \frac{P_{H_2}^3 P_{CO}}{K_6}\right)}{P_{H_2O}^{1.5696}}$$	(3.17)
	$CO + H_2O$ $\leftrightarrow H_2 + CO_2$	(R3.7)	$$r_7 = \frac{\frac{k_7}{P_{H_2}}\left(P_{CO}P_{H_2O} - \frac{P_{H_2}P_{CO_2}}{K_7}\right)}{\left(1 + K_{7,CO}P_{CO} + K_{7,H_2}P_{H_2} + K_{7,CH_4}P_{CH_4} + \frac{K_{7,H_2O}P_{H_2O}}{P_{H_2}}\right)^2}$$	(3.18)

For the oxygen carrier, the rate of conversion is measured based on the amount of OC that reacts, taking into account the reaction stoichiometry and the initial amount of active metal (Equation 3.11). For the oxidation reaction, R3.1, the kinetic rate can be estimated with the shrinking core model,

which considers the effect of the decreasing available reaction surface; the kinetic parameters for R3.1 were obtained from Zhou et al. and Nordness et al. [64] [65].

For the reduction stage, reaction mechanics are often consistent with nucleation. This can be modelled using the nucleation-based Avrami-Erofe'ev mechanistic model; if nucleation occurs sufficiently quickly, these kinetics can be simplified using a volumetric approach [15]. Experimental data shows that reactions R3.2 and R3.4 are dominant and occur more quickly than R3.3 and R3.5 [27]; as such, a modified volumetric model was used to model R3.2 and R3.4, with parameters obtained from Iliuta et al. [63]. This scheme was found to provide a good estimation of these reaction rates. For reactions R3.3 and R3.5, which are slower and are more prevalent towards the end of the reduction stage, the nucleation-based Avrami-Erofe'ev mechanistic model was found to provide more accurate reaction rate predictions compared to the simplified volumetric approach. The kinetic rate parameters for these reactions were determined by Han et al. [66] [67].

The equilibrium kinetics were taken from Numaguchi et al. and Spallina et al. for the SMR reaction (R3.6) [68] [29], and Nordness et al. for the WGS reaction (R3.7) [65]. The proposed multiscale model was validated using simulations against data from multiple experimental sources and by performing a sensitivity analysis, shown in Section 3.3.

3.2 NMPC Formulation

In packed bed CLC, implementing a control scheme is useful to account for disturbances (e.g. fluctuations in the inlet temperature) and changes in the transient operation (i.e. changes in the reaction rates as the OC reaches full conversion). In addition, a control strategy can ensure that the temperature remains within safe operating bounds and does not reach reactor- or OC-damaging temperatures. As discussed in the introduction, if the peak temperature of oxidation can be adjusted, this could allow for

the use of more concentrated active material on the oxygen carrier without reaching unsafe temperatures. Implementing a control strategy with a more concentrated OC allows for the possibility of using a more compact reactor to generate the same amount of energy. In the reduction stage, controlling the outlet composition can ensure that most of the inlet CH_4 reacts to form CO_2 and H_2O, improving the purity of this outlet CO_2 stream once the H_2O is removed. To fulfill these requirements, a nonlinear model predictive control (NMPC) strategy is deployed to control the oxidation and reduction stages in packed bed CLC. NMPC was chosen over other control schemes as it can be used for multivariable control and can account for predicted model behaviour. For instance, during the oxidation stage, the heat front moves through the reactor slowly, which causes a delay between the control action and the response in the outlet temperature. This makes it vital that the control actions consider the predicted future states of the system. In addition, NMPC can account for constraints, which ensures that safety considerations are met (e.g. constraining the peak temperature in the reactor such that it remains within safe bounds).

In NMPC, for every sampling interval, an online optimization problem is solved to determine the optimal control actions to minimize the deviations between the controlled variables and a setpoint, while avoiding unnecessary changes made to the manipulated variables. The nominal NMPC formulation used for this process is as follows:

$$\min_{\hat{x}(\tau),\hat{u}(\tau)} \int_t^{t+t_p} \left\| \hat{x}(\tau) - x_{sp} \right\|_Q^2 d\tau + \int_t^{t+t_c} \left\| \Delta\hat{u}(\tau) \right\|_R^2 d\tau \tag{3.19a}$$

s.t.

$$f\big(\dot{\hat{x}}(\tau), \hat{x}(\tau), \hat{u}(\tau), \tau\big) = 0 \tag{3.19b}$$

$$h(\hat{x}(\tau), \hat{u}(\tau), \tau) = 0 \tag{3.19c}$$

29

$$g(\widehat{\boldsymbol{x}}(\tau), \widehat{\boldsymbol{u}}(\tau), \tau) \leq 0 \tag{3.19d}$$

$$\widehat{\boldsymbol{x}}_{\boldsymbol{0}}(\tau) = \boldsymbol{x}(t), \tau_k = t_{k-1} \tag{3.19e}$$

$$\widehat{\boldsymbol{u}}(\tau) = \widehat{\boldsymbol{u}}(t + t_c), \forall \tau \in [t + t_c, t + t_p) \tag{3.19f}$$

$$\widehat{\boldsymbol{u}}(\tau) \in U, \forall \tau \in [t, t + t_c) \tag{3.19g}$$

$$\widehat{\boldsymbol{x}}(\tau) \in \chi, \forall \tau \in [t, t + t_p) \tag{3.19h}$$

$$\chi := \{\boldsymbol{x} \in \mathbb{R}^{N_x}\}, U := \{\widehat{\boldsymbol{u}} \in \mathbb{R}^{N_u}, \boldsymbol{u}^l \leq \widehat{\boldsymbol{u}} \leq \boldsymbol{u}^h\}, T := \{\tau \in \mathbb{R}^{N_\tau}, t \leq \tau \leq t_p\} \tag{3.19i}$$

where $\boldsymbol{x}$ is the vector of process states at the sampling time, assuming that the NMPC has access to the measurement for all process states, and $\widehat{\boldsymbol{u}}$ is the vector of control actions implemented by the plant. $\widehat{\boldsymbol{x}}$ represents the predicted vector of future states within the NMPC framework, with corresponding derivatives denoted by $\dot{\widehat{\boldsymbol{x}}}$. Matrices $\boldsymbol{Q} \in \mathbb{R}^{N_q} \times \mathbb{R}^{N_q}$ and $\boldsymbol{R} \in \mathbb{R}^{N_u} \times \mathbb{R}^{N_u}$ represent the weights for each term in the objective function, with $\boldsymbol{Q}$ penalizing the deviation between a predicted state $\widehat{\boldsymbol{x}}(\tau)$ and the setpoint $\boldsymbol{x}_{sp}$, and $\boldsymbol{R}$ penalizing changes to the control actions $\Delta\widehat{\boldsymbol{u}}(\tau)$. $\boldsymbol{f:}$ $\mathbb{R}^{2N_x} \times \mathbb{R}^{N_u} \times \mathbb{R}^{N_\tau} \rightarrow \mathbb{R}^{N_x}$ denotes the dynamic model used generate model predictions. $\boldsymbol{h:}$ $\mathbb{R}^{N_x} \times \mathbb{R}^{N_u} \times \mathbb{R}^{N_\tau} \rightarrow \mathbb{R}^{N_h}$ represents the set of equality constraints, including the CLC reaction rates presented in Table 3.2 (Equations 3.12-3.18), as well as additional algebraic correlations presented in Appendix A. $\boldsymbol{g:} \mathbb{R}^{N_x} \times \mathbb{R}^{N_u} \times \mathbb{R}^{N_\tau} \rightarrow \mathbb{R}^{N_g}$ represents the set of inequality constraints; for instance, the changes in the manipulated variables $\Delta\widehat{\boldsymbol{u}}$ are restricted by $\Delta\boldsymbol{u}_{max}$ to ensure that the controller does not make drastic changes to the adjustable variables, which can result in an unstable system response. t represents the actual process time, and τ represents the future time within the NMPC model.

For each sampling time t, the plant's states $\boldsymbol{x}$ are measured to obtain the initial conditions for the NMPC framework (Equation 3.19e). The NMPC formulation aims to minimize the objective

function presented in Equation 3.19a over the prediction horizon t_p by changing the values of the manipulated variables over the control horizon t_c, where $t_c \leq t_p$, as depicted in Figure 3.3. NMPC will account for the model and constraints presented in f, h, and g, as well as the manipulated variable bounds u^l and u^h, to find a feasible optimal set of control actions. The states are measured over every time interval k, and the controller will implement the next control action based on the optimal solution obtained from the NMPC model. Then, a new set of measurements are obtained at $t = t+k$, and the next iteration of NMPC is performed, as depicted in Figure 3.4.
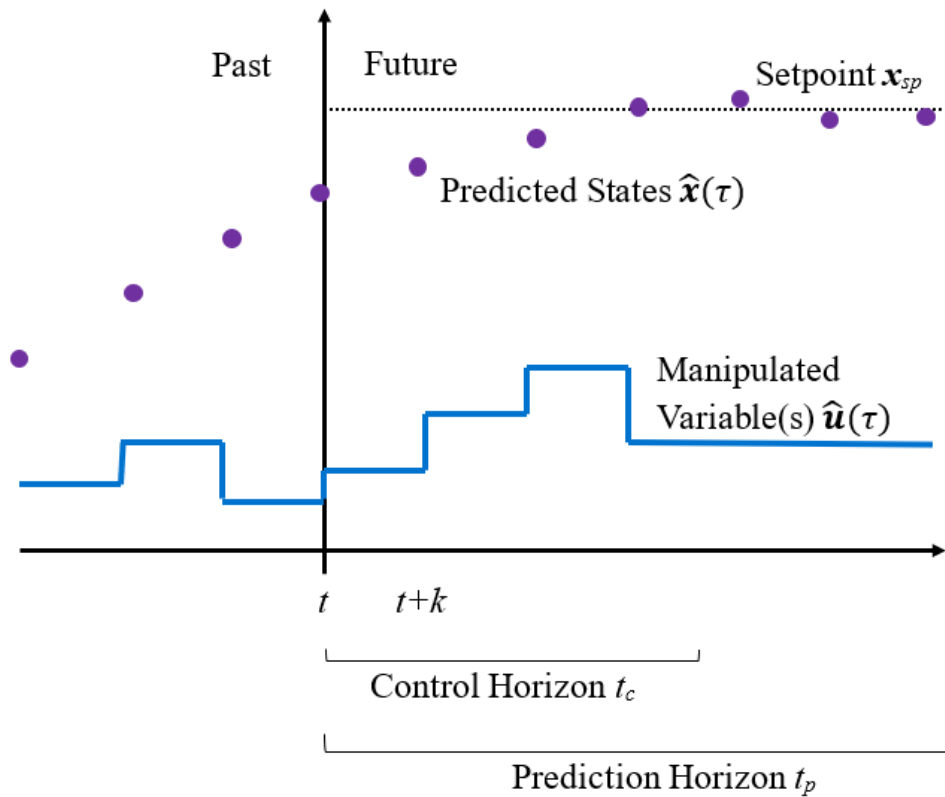
Figure 3.3. Schematic depicting the role of the prediction and control horizons in MPC.
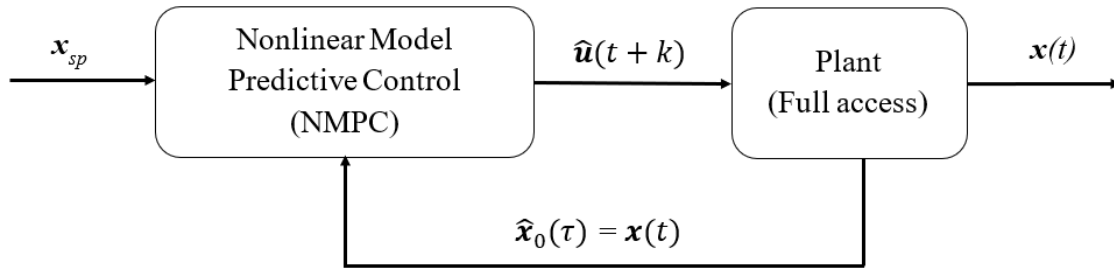
Figure 3.4. Schematic of the feedback loop between the simulated plant and NMPC.

For the packed bed CLC system, the states of interest, x, are the bulk concentration, temperature, and conversion of the oxygen carrier. The manipulated variables, $\hat{u}$, are the inlet mass fluxes; fuel (CH_4) for the reduction stage, and air and inert (N_2) streams for the oxidation stage. In the oxidation stage, the inert gas is added to dilute the oxygen entering the reactor. This slows down the reaction rate so that the relative speed of the reaction and heat fronts can be manipulated to control the temperature and maintain it at a setpoint. This in turn prevents the air from reaching the peak temperature, thereby damaging the reactor, OC, and downstream turbine. The many interacting states, as well as the large number of states which encapsulate the behaviour at the different spatial scales, significantly increase the model complexity, resulting in a multiscale model which is computationally expensive for online control applications. This is addressed by investigating a pseudo-homogeneous model, which is described next.

3.2.1 Pseudo-Homogeneous Model

A pseudo-homogeneous model was investigated as a potential alternative to decrease the online computational costs for real-time applications involving CLC PBR. In the pseudo-homogeneous model, the intra-particle gradients are considered to be negligible allowing for the particle behaviour to be neglected. In this case, the diffusion must occur sufficiently quickly for the reactions to be the rate

limiting step in the process [8]. To ensure that this is appropriate, it was verified that D/D_p is greater than 100 (the particle diameter is sufficiently small that the particle gradients will be insignificant), the mass and heat transfer coefficients k_c and h_f are greater than 0.05 m/s and 0.1 W, respectively (the mass and heat transfer with the particle is not rate-limiting), and the Weisz-Prater criterion is less than 1 (the diffusion occurs much more quickly than the reaction) [8]. The Weisz-Prater criterion is as follows:

$$N_{WP} = \frac{r_{obs}\rho_s\epsilon_s a_p^2}{D_{e,i}C_i},$$
(3.20)

where r_{obs} is the observed reaction rate and a_p is the characteristic length of the particle. Diglio et al. and Han et al. determined that these criteria hold up for packed bed CLC, and the pseudo-homogeneous model can reasonably be used to approximate the behaviour in this system [8] [6]. As such, as long as these criteria are met, neglecting the particle behaviour to focus on the overall bulk-scale behaviour is a reasonable approximation for the internal NMPC model (as depicted in Figure 3.4). The resulting reduced-order mass and energy balances for the pseudo-homogeneous model are presented in Table 3.3.

Table 3.3. Mass and energy balances for the pseudo-homogeneous packed bed CLC model.

Pseudo-Homogeneous Mass and Energy Balances		
Mass Balance	$\varepsilon_b \dfrac{\partial C_i}{\partial t} + \dfrac{\partial F_i}{\partial V} = \dfrac{\partial}{\partial z}\left(D_{ax,i}\dfrac{\partial C_i}{\partial z}\right) + \varepsilon_c\rho_s \sum_{j=1}^{n_r} r_{i,j}$	(3.21)
Energy Balance	$\varepsilon_b C_{pf} C_T \dfrac{\partial T}{\partial t} + C_{pf} F_T \dfrac{\partial T}{\partial V} = \dfrac{\partial}{\partial z}\left(\lambda_{ax}\dfrac{\partial T}{\partial z}\right) + \varepsilon_c\rho_s \sum_{j=1}^{n_r} (-\Delta H_j)r_j$	(3.22)
	$\varepsilon_b D_{ax,i}\dfrac{\partial C_i}{\partial z}\bigg|_{z=0} = (F_i|_{z=0} - y_{i,feed}F_{in})/A_c$	(3.23)

33

Dankwerts Boundary Conditions	$$\left. \varepsilon_b \lambda_{ax} \frac{\partial T}{\partial z} \right|_{z=0} = (T_c|_{z=0} - T_{in}) C_{pf} F_T / A_c$$	(3.24)
	$$\left. \frac{\partial C_i}{\partial z} \right|_{z=L} = \left. \frac{\partial T}{\partial z} \right|_{z=L} = 0$$	(3.25)

As shown in Table 3.3, the pseudo-homogeneous model is similar to the multiscale model presented in Section 3.1.1, but is only comprised of the mass and energy balances for the bulk gas in the system. Because the particle gradients are assumed to be negligible, the reactor balances do not have a term to consider mass and heat transfer with the particle, and the states within the particle are assumed to be the same as the bulk gas. To account for the reactions taking place, the kinetic rates from Table 3.2 are directly incorporated in the reactor mass and energy balances to compute the r_j term in Equations 3.21 and 3.22. The dynamic model in Equations 3.21-3.25 is denoted as f as shown in the NMPC formulation presented in Section 3.2.

3.3 Results and Discussion

3.3.1 Implementation

The multiscale model presented in Section 3.1 was discretized using orthogonal collocation of finite elements with 4 elements which each have 5 interior Radau collocation points for the axial direction z; centered finite differences with 5 intervals for the radial domain r_c, and backward finite differences for the time domain t with one node every 10 s. Both the oxidation and reduction stages were discretized in this way, and the discretization scheme was chosen to ensure that the model could be accurately solved for both stages while still solving quickly.

For the multiscale model of the oxidation stage, the bulk-scale states (oxygen concentration and temperature) and particle-scale states (oxygen concentration, temperature, and OC conversion) must be considered. These states are all dependent on their spatial and temporal positions within the reactor, and as such, must be modelled at different locations within the reactor. This results in 500 spatially-discretized states for the multiscale model, and 9,700 discretized variables in the multiscale plant model.

In the reduction stage, various product gases are generated, and as such, the concentrations for the CH_4, H_2, CO, CO_2, H_2O, and inert gas all need to be considered to accurately predict the behaviour within the system. As with the oxidation stage, these states are space- and time-dependent. This leads to 1,375 spatial states in the multiscale model, and a plant model with 19,425 discretized variables.

To reduce computational costs, the pseudo-homogeneous model presented in Table 3.3 was used as the NMPC internal model, discretizing the axial and time domains using the same discretization scheme implemented for the multiscale model. The resulting oxidation and reduction stage models have fewer states than the full multiscale model: 75 spatial states for the oxidation stage, and 200 spatial states for the reduction stage. Once the algebraic variables are included, this results in a system with 12,777 variables for the oxidation stage, and 11,816 variables for the reduction stage. Note that there are more variables in the pseudo-homogeneous model of the oxidation stage because the NMPC model predicts the behaviour over the entire prediction horizon, resulting in more temporal states.

The control variable for the oxidation stage is the outlet temperature, whereas the control variables for the reduction stage are the CO_2 selectivity (the fraction of carbon in CH_4 that reacts to produce CO_2, as shown in Equation 3.26) and the outlet CO_2 flux.

$$S_{CO_2} = \frac{F_{CO2,out}}{F_{CH_4,in}} \tag{3.26}$$

$F_{CO2,out}$ is the outlet molar flowrate of CO_2, and $F_{CH4,in}$ is the inlet molar flowrate of CH_4.

The systems of PDEs presented in Table 3.1 (multiscale model) and Table 3.3 (pseudo-homogeneous model) were transcribed with pyomo [69] for both the oxidation and reduction stages. They were then solved using an interior-point algorithm (IPOPT) on an Intel core i7-3770 CPU @ 3.40 GHz processor [70].

3.3.2 Model Validation

3.3.2.1 Oxidation

To demonstrate the prediction capabilities of the proposed multiscale and pseudo-homogeneous oxidation models, they were compared to two distinct sets of data: one set of data from a lab-scale experiment by Hamers et al. [28], and another set of data from an industrial-scale simulation performed by Han et al. [30]. For the lab-scale reactor, an additional heat exchange term representing heat lost to the surroundings was included in Equation 3.2, based on the parameters provided by Hamers et al. [28]. The operating conditions used for each simulation are listed in Table 3.4. The predicted outlet temperatures using the multiscale model and the pseudo-homogeneous models under the conditions from Hamers et al. and Han et al. are presented in Figure 3.5.

Table 3.4. Operating conditions of the two sets of data (Hamers et al.: experimental; Han et al.: simulation) which were used as the simulated operating conditions for validation of the packed bed CLC oxidation stage model.

Parameter	Hamers et al. [28]	Han et al. [30]
L [m]	0.69	11.0
D [m]	0.063	5.5
D_p [mm]	2.0	5.0

$C_{Ni,0}$ [kg/kg OC]	0.19	0.20
ε_c	0.55	0.40
T_{in} [°C]	450	450
P_{in} [bar]	2.0	17.0
G [kg/m^2/s]	0.655	2.5
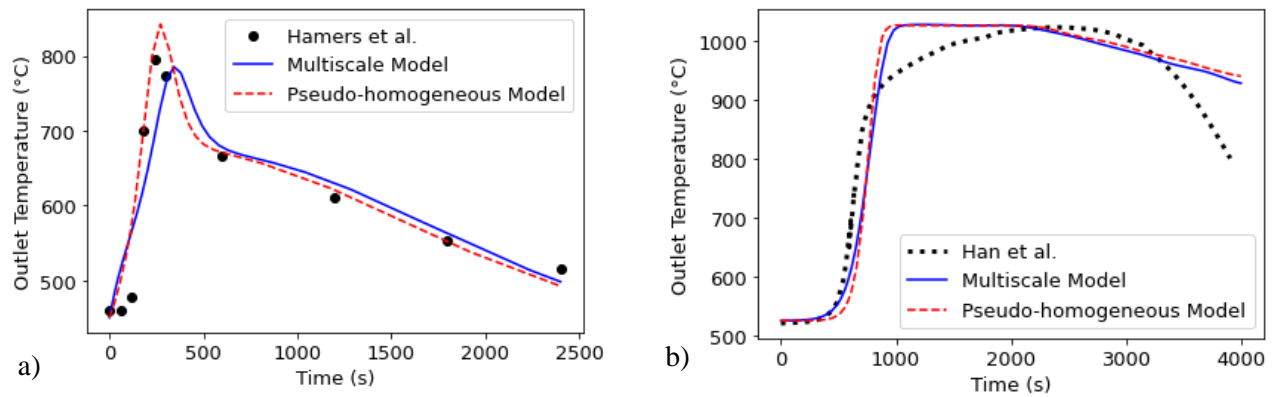
Figure 3.5. Profiles for the outlet temperature of the oxidation stage simulation using the multiscale and pseudo-homogeneous models compared to the literature results from a) the experiment performed by Hamers et al. and b) the simulation performed by Han et al.

As shown in Figure 3.5, both models predicted reasonable behaviour for both the lab-scale and industrial-scale conditions. In Figure 3.5a, both models predict a more immediate change in the outlet temperature than that observed in the experiment; this may be because the experiment is non-ideal, resulting in a lag period as the oxygen is introduced to the reactor. In general, both the multiscale and pseudo-homogeneous models successfully capture the rapid temperature increase of the fast oxidation reaction, followed by a more gradual temperature decline as the heat front is carried through the reactor. Because the pseudo-homogeneous model does not consider diffusion, it predicts a slightly faster reaction, where the outlet temperature increases more quickly and reaches a higher value. The

simulation operating conditions used by Han et al. [30] were vastly different than the experimental conditions used by Hamers et al. [28] in terms of reactor size, pressure, and inlet flowrate, but the proposed models returned acceptable predictions of the outlet temperature profiles under both sets of conditions.

In addition to comparing the model predictions to other literature results, a sensitivity analysis was performed, varying the reactor design and operating conditions. The results from this analysis are presented in detail in Appendix B (Figure B.2-Figure B.4). These results showed that most changes to the reactor design or operating conditions would not meaningfully impact the temperature increase during the oxidation stage, which is in agreement with the observations made by Noorman et al. [10]. The most effective way to change the temperature achieved during the oxidation of the OC was by changing the concentration of active metal on the OC [10]. If air is the only inlet gas, increasing the mass flux increases the speed at which the heat and reaction fronts progress through the reactor, but manipulating the inlet gas cannot control the peak temperature. Likewise, increasing the reactor length can increase the amount of time that the temperature is held high, and will impact the time it takes the hot gas to reach the outlet, but will not affect the actual temperature achieved. Hence, the results from the sensitivity analysis were consistent with findings from literature data, and show that the inlet air flowrate cannot be used as the only manipulated variable in order to control the outlet temperature.

3.3.2.2 Reduction

To verify the reduction kinetic parameter set proposed in this work (see Table 3.2), the models and kinetic scheme were validated against experimental data with different particle diameters, inlet flowrates, and methane concentrations from Jin et al. [27] and from Spallina et al. [29]. The operating conditions used for each experiment are listed in Table 3.5, and the simulation results for both the

multiscale and pseudo-homogeneous models are presented in Figure 3.6 (using the conditions from Jin et al.) and Figure 3.7 (using the conditions from Spallina et al.). An additional validation that compares the model predictions to Jin et al.'s results at 973 K is presented in the Appendix B (Figure B.1).

Table 3.5. Operating conditions of the two sets of experimental data which were used as the simulated operating conditions for validation of the packed bed reduction stage CLC model.

Parameter	Jin et al. [27]	Spallina et al. [29]
L [m]	0.25	0.5
D [mm]	16	30
D_p [mm]	5.0	0.59
$C_{NiO,0}$ [kg/kg OC]	0.60	0.185
ε_c	0.478	0.55
T_{in} [K]	873	1173
P_{in} [bar]	1.0	1.1
Q [L/min]	0.9	20
Inlet Composition	33 vol% CH_4, 67 vol% H_2O	5 vol% CH_4, 30 vol% H_2O, 65 vol% Ar

a)

b)
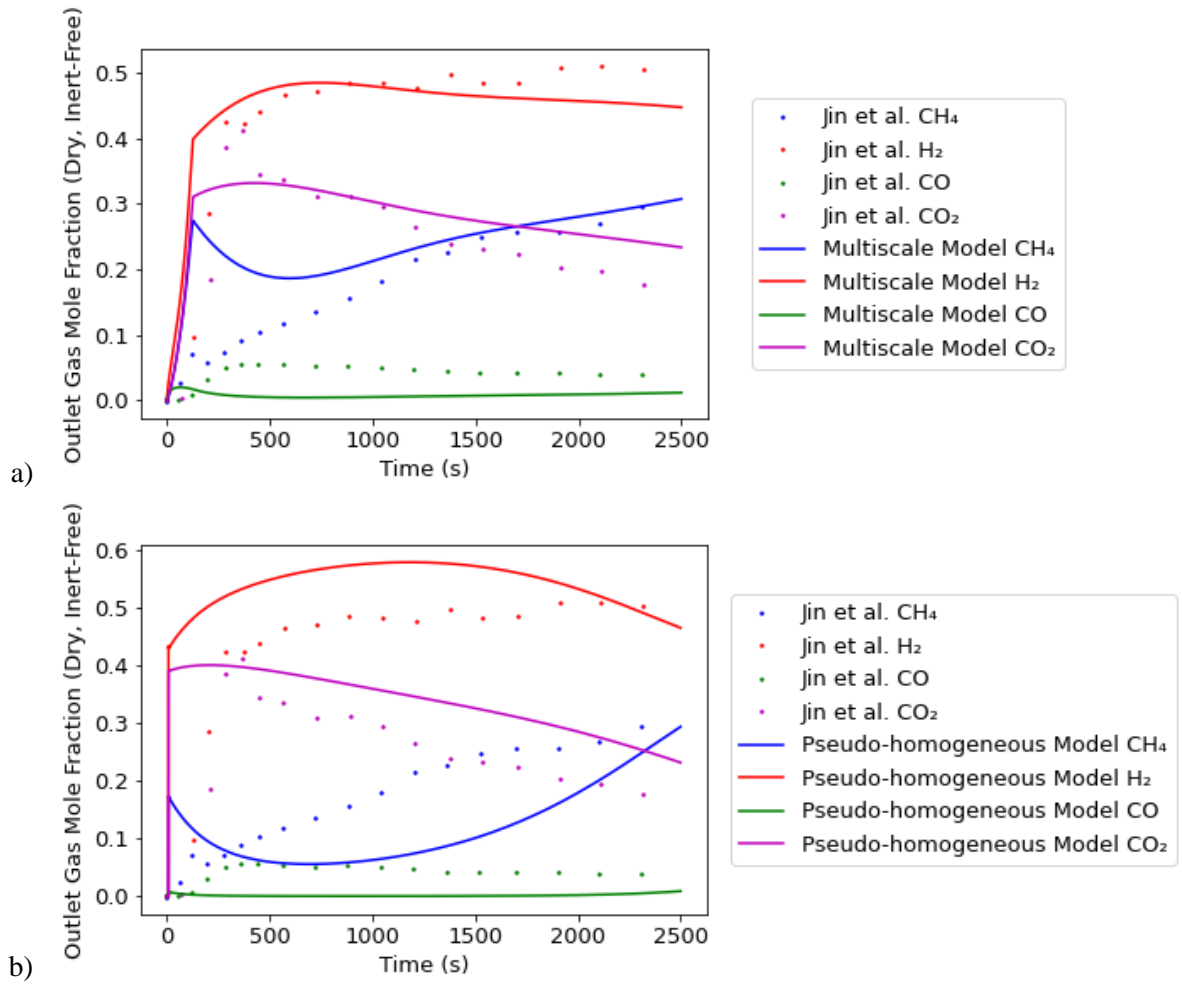
Figure 3.6. Outlet dry gas mole fraction profiles for the reduction stage simulation under the experimental conditions used by Jin et al. at 873 K using a) the multiscale model and b) the pseudo-homogeneous model.
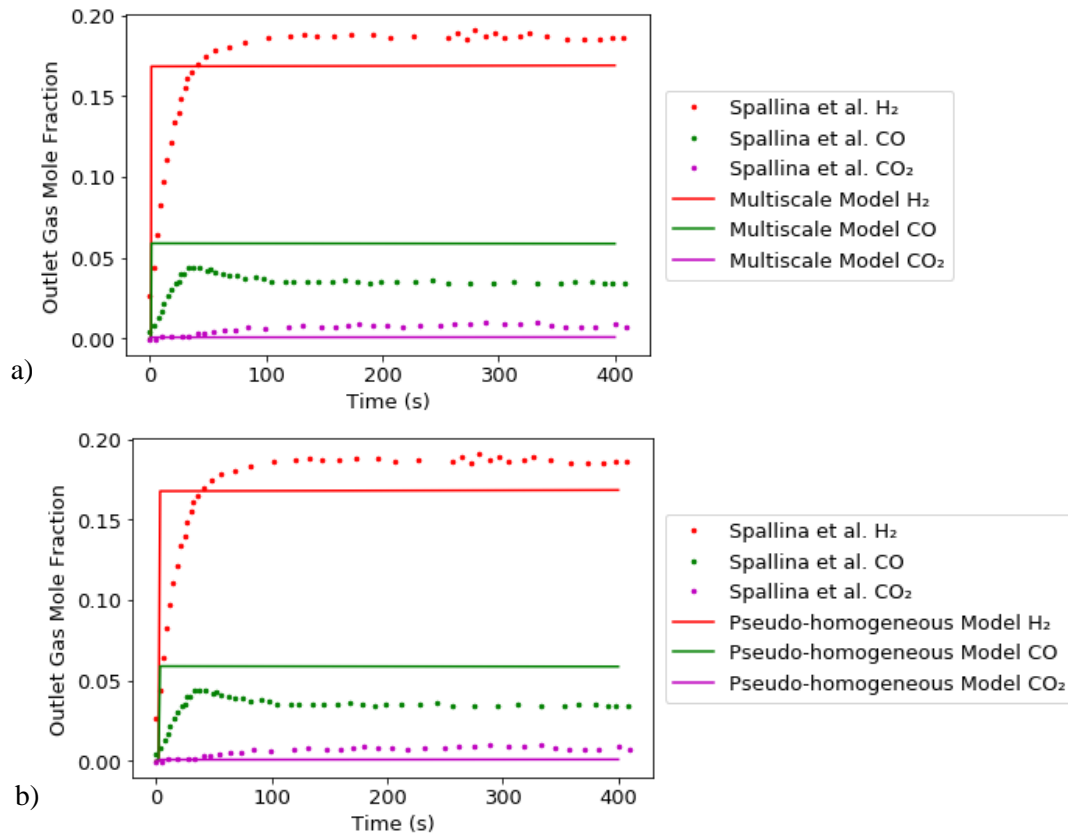
Figure 3.7. Outlet dry gas mole fraction profiles for the reduction stage simulation compared to experimental data under the operating conditions used by Spallina et al. using a) the multiscale model and b) the pseudo-homogeneous model.

Under each set of conditions, the magnitudes and dynamic profiles of each compound as predicted by the multiscale model demonstrated similar behaviour to that observed in the experimental literature. In Figure 3.6, the experimental outlet CH_4 fraction is initially very low (less than 10% of the dry outlet fraction in the experimental data), and increases as the OC reaches complete conversion. Likewise, the outlet CO_2 fraction is at its highest early in the reduction stage, and decreases as the oxygen availability declines. The multiscale model predictions shown in Figure 3.6a overestimated the outlet CH_4 fraction when compared to Jin et al.'s results at 873 K, but as experimental data and model parameters are subject to error (e.g., measurement noise) and uncertainty, this deviation is deemed to

be acceptable. In addition, the proposed multiscale model predicts similar behaviour over the course of the reaction and follows the expected trends as the temperature is increased (most notably, higher CO_2 concentration, and less CH_4 reaching the outlet). The pseudo-homogeneous model predictions depicted in Figure 3.6b neglects diffusion limitations and thus predicts faster reaction rates, under-predicting the outlet CH_4 fraction and over-predicting the outlet H_2 and CO_2 fractions. However, the pseudo-homogeneous model still provides a reasonable approximation of the PBR behaviour.

Because of the additional discrepancies between the pseudo-homogeneous model and experimental data for the larger particle size, the full multiscale model was chosen to simulate the plant behaviour. However, the good approximation provided by the pseudo-homogeneous model suggests that the particle gradients are small enough that they can reasonably be neglected to solve the NMPC model with lower computational costs, which is crucial for online control and optimization applications.

The multiscale model also predicted the different behaviour with a hotter reactor and a lower inlet CH_4 fraction, as observed in Figure 3.7. Both models predicted abrupt changes in the outlet gas composition once the fuel was introduced to the reactor. This change was more sudden than it had been in the experimental results, likely because the models do not account for the time delay as the experiment started and fuel was first introduced to the reactor. Under these conditions, most of the inlet CH_4 reacted to form CO and H_2, making the outlet methane concentration negligible. The model overpredicted the CO fraction and underpredicted the H_2 production, but the absolute errors between the simulated and experimental gas compositions remained below 3%; accordingly, these kinetic equations were used for both models in order to predict the outlet concentrations from the reduction stage. In this case, the pseudo-homogeneous model in Figure 3.7b predicts a very similar response to that shown by the multiscale model in Figure 3.7a, which is likely because the smaller particles in this experiment resulted in smaller intra-particle gradients.

As with the oxidation stage, a sensitivity analysis was performed to further validate the proposed reduction stage models, performing simulations using different reactor designs and operating conditions. Due to the more complex reaction scheme, the reduction stage is more sensitive to changes in the operating conditions, and varying the inlet flowrate or reactor temperature can have a pronounced impact on the outlet mole fractions. Decreasing the flowrate (thus increasing the residence time) and increasing the concentration of active metal both increase the exposure of the inlet gas to oxygen, increasing the amount of gas converted to CO_2 and H_2O. Increasing the temperature speeds up the oxygen carrier reactions taking place, which also leads to an increase in the gas conversion and improves the CO_2 purity of the outlet stream. The results from this sensitivity analysis are presented and discussed in Appendix B (Figure B.5-Figure B.8). The model output was consistent with expectations for both the multiscale and pseudo-homogeneous models, and these were then used as the reduction stage plant and NMPC models, respectively.

3.3.3 Closed-loop Control

Using the validated models and the NMPC formulation outlined in Section 3.2, the closed-loop performance of the CLC PBR was evaluated for both stages. The design and operating conditions used for this control framework are listed in Table 3.6, and the NMPC parameters are presented in Table 3.7.

Table 3.6. Reactor design and operating conditions used for the packed bed CLC process in this work.

Design & Operation Parameters	Parameter Values
L [m]	11.0
D [m]	5.5
D_p [mm]	5.0
$C_{Ni,0}$ [kg/kg OC]	0.3

ε_c	0.4
T_{in} [°C]	450
P_{in} [bar]	17.0

Table 3.7. Parameters used in implementing the NMPC scheme for the oxidation and reduction stages of packed bed CLC.

NMPC Parameters	Oxidation	Reduction
Sampling Interval [s]	50	30
Prediction Horizon [s)	500	150
Control Horizon [s]	500	150
Inlet Flux Bounds [kg/m²/s]	Air: [1, 8] Inert (N_2): [1, 20]	CH_4: [0.1, 5]
Maximum Change in Flux [kg/m²/s]	3	1

The NMPC framework considered in this work was implemented for a large-scale reactor to present operating strategies which increase the energy-generation capacity as well as the carbon capture efficiency of an industrial-scale plant implementing packed bed CLC. A high pressure is used for the system as this has been found to have faster kinetics and can improve the efficiency of the process. In the proposed NMPC scheme, full state access was assumed, and the prediction and control horizons t_p and t_c are chosen to be equal as this was found to result in good setpoint tracking. For the oxidation stage, where the outlet temperature does not immediately reflect changes made to the inlet mass flux, the prediction and control horizons are set to 500 s to ensure that that relevant future behaviour is accounted for.

For industrial-scale incineration plants, measurements of the composition and temperature (the same states which would be measured in a CLC plant) are often taken roughly every 20 s, meaning that the chosen sampling interval for NMPC should be at least 20 s to ensure that the control scheme can be feasibly implemented [71] [72]. Various sampling intervals were investigated, and a sampling interval of 50 s resulted in good control while solving quickly enough for online implementation. For the reduction stage, where the control actions affect the output more quickly, the prediction and control horizons are 150 s and the sampling interval is 30 s.

As mentioned in Section 3.2, for the NMPC optimization problem, the dynamic model f consists of the pseudo-homogeneous model presented in Table 3.3. The problem is constrained by the equality constraints h (the algebraic correlations presented in Table 3.2 and in Appendix A), and inequality constraints g (restricting the changes in the manipulated variables by Δu_{max}, which is used instead of a control suppression term in the objective). The values of Δu_{max}, as well as the manipulated variable bounds u^l and u^h, are presented in Table 3.7. The bounds u^l and u^h were set to values which provided operational flexibility while remaining within a realistic range based on the range of flowrates used in existing CLC literature and in large-scale natural gas combustion plants.

3.3.3.1 Oxidation

For the oxidation stage, NMPC is employed to control the outlet temperature by manipulating the inlet air and inlet inert gas fluxes. The temperature setpoint is set to 900 °C as it falls within the operational range of turbines (827-1627 °C) [73]. It is also low enough to avoid factors which would reduce the effectiveness of the OC; at high temperatures (1000 °C), Al_2O_3-supported NiO is prone to agglomeration and to the phase transformation to $NiAl_2O_4$, which decrease the oxygen-carrying

capacity of the OC [74] [75]. The objective for the oxidation stage was formulated by minimizing the sum of square errors in between the actual outlet temperature and the temperature setpoint:

$$J_{ox} = \int_t^{t+t_p} \left(T_{out}(\tau) - T_{sp} \right)^2 d\tau \tag{3.27}$$

To establish a baseline, this stage was simulated using a constant inlet air flowrate, as it is a common assumption for packed bed CLC. Amrollahi et al. [76] investigated post-combustion CO_2 in a 384 MW natural-gas-fired power plant, which used a constant inlet air flowrate of roughly 650 kg/s (corresponding to approximately 27.4 $kg/m^2/s$ in a reactor of this size). The reactor dimensions used in this work correspond to a 350-400 MW_e power plant [9]; accordingly, a 650 kg/s flowrate was deemed to be an appropriate basis of comparison. The results from this simulation are depicted by the dashed pink lines in Figure 3.8. As shown in Figure 3.8b, the fast, oxygen-rich inlet gas increases the outlet temperature very quickly, but as this quantity of oxygen reacts with the Ni very quickly, the reaction ends and the temperature drops quickly, completing the oxidation stage in about 600 s. Given that a reactor for packed bed CLC only generates energy during the oxidation stage, it is desirable for the oxidation stage to last for a long time to ensure that a greater percentage of the operation time is dedicated to energy production [30]. The high flowrate shown in Figure 3.8a causes the oxidation stage to quickly reach completion, which would be detrimental for energy generation.

To maintain the temperature at a given value for a longer period of time, NMPC was run with a setpoint of 900 °C. Implementing NMPC for this system resulted in good setpoint tracking, shown in Figure 3.8b, and the average computational time for each iteration of NMPC was approximately 40 s, which solves fast enough for online implementation with the sampling interval of 50 s. With NMPC, the temperature is held within 10 °C of the setpoint for approximately 1300 s, which allows the reactor to generate energy for roughly three times longer than the case where a constant air flowrate is

implemented. Gas turbines operate most efficiently under constant conditions [77] [78]; moreover, it would be inefficient to frequently switch stages during CLC. Thus, controlling the outlet temperature to increase the duration of the oxidation stage results in a more efficient process.
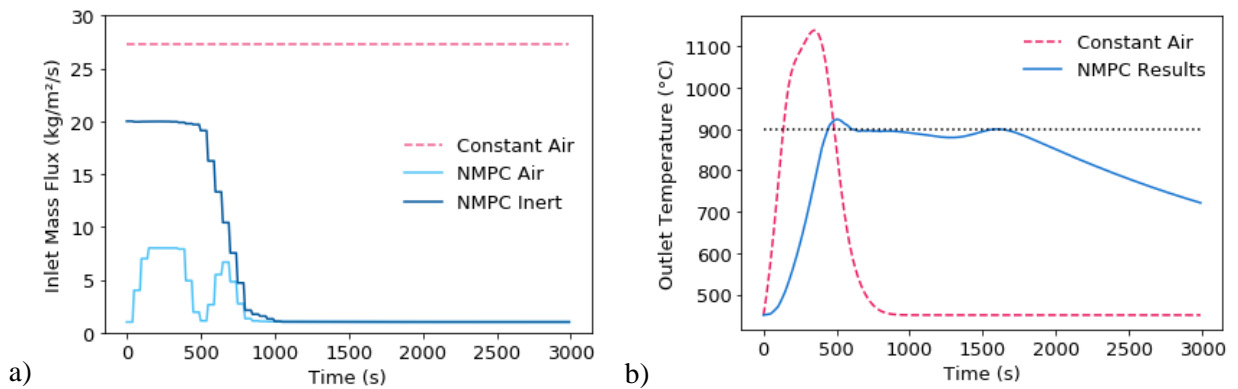
Figure 3.8. a) Inlet mass flux (air and inert) and b) outlet temperature profiles compared from using a constant inlet air flux (dashed pink lines) and from implementing the NMPC scheme (solid blue lines).

In the control profile provided by NMPC (Figure 3.8a), the inlet air flux quickly reaches the upper bound to start the reaction, but drops before 500 s to avoid overshooting the setpoint temperature, with a second peak to ensure that the oxidation reaction reaches completion. The inlet inert flux is initially held at the upper bound to dilute the heat produced and speed up the heat front so that the hot air reaches the outlet more quickly, and decreases to reduce the heat front velocity so that the temperature can be held at the setpoint for longer. Past 1000 s, the exothermic oxidation reaction has reached completion (see Figure B.9 in Appendix B for profiles of the OC conversion during the reaction), and both fluxes are held at their lower bounds to maintain the slow progression of the heat front for the remainder of the oxidation stage.

47

Once the reaction has reached completion at 1000 s, the reactor is in the heat recovery phase, where gas is introduced to the reactor to carry the remaining heat to the outlet. Because no further heat is produced, both gas fluxes are at their lower bounds to avoid diluting the heat and keep the outlet temperature at the setpoint for longer. This results in a total inlet gas flux of 2 kg/m^2/s, which is much lower than the 27 kg/m^2/s flux in a typical natural gas combustion process. If needed, a smaller turbine could be used to accommodate this lower flowrate, although using a lower flowrate would generate less energy. Various studies have investigated reactor scheduling for packed bed CLC, and it is common practice for multiple reactors to undergo the heat recovery phase at the same time; this would increase the overall flowrate of hot air, which could power a larger turbine to generate more energy [9] [31].

The NMPC scheme where two inlet gas fluxes were manipulated was compared to a case where there was only an air inlet stream as the manipulated variable, as shown in Figure 3.9.
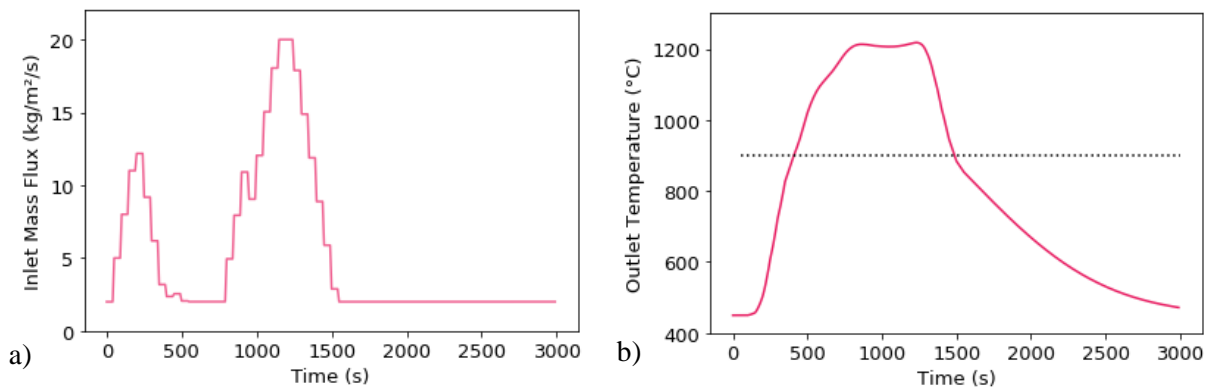
Figure 3.9. a) Inlet mass flux and b) outlet temperature profiles when air is the only control variable used in the NMPC scheme.

When air is the only inlet gas, the resulting outlet temperature cannot track the setpoint, even while implementing NMPC (Figure 3.9b), as the inert gas is necessary to dilute the oxygen and the heat to avoid overshooting the temperature. By the time the NMPC decreases the inlet air flowrate in Figure 3.9a, the temperature within the reactor has already surpassed the setpoint by roughly 300 °C – which

48

is made evident at around 500 s when this heat front reaches the outlet. Temperatures this high would increase the rates of agglomeration and attrition of the oxygen carrier [30] [75], thus adding an inert gas to this system is vital in order to control the outlet gas temperature.

To further verify that the NMPC scheme could provide appropriate control actions to track different setpoints, the NMPC scheme was also tested using a setpoint of 850 °C, shown in Figure 3.10.
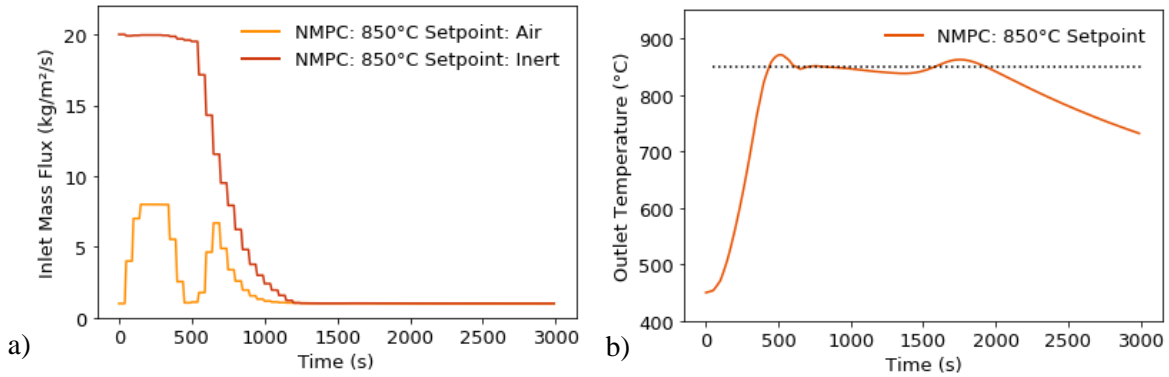
Figure 3.10. a) Inlet mass flux (air and inert) and b) outlet temperature profiles implementing an NMPC scheme using a setpoint of 850 °C.

Under this new setpoint, the control profiles from the NMPC in Figure 3.10a were slightly different, and these adjustments were appropriate in order to keep the temperature within 10 °C of 850 °C for approximately 1500 s (Figure 3.10b). To meet the new setpoint, the air flux is decreased sooner to slow down the reaction, and the inert flux is decreased more gradually to continue to dilute the inlet oxygen. These results show that the NMPC is able to adequately control the temperature during the oxidation stage, resulting in a system that can respond to changes in dynamics and potentially use a more compact reactor with more concentrated metal oxide.

49

3.3.3.2 Reduction

NMPC was also implemented for the reduction stage of packed bed CLC to optimize the carbon capture effectiveness. To accomplish this goal, the CO_2 selectivity was selected as one of the control variables, to ensure that the outlet stream consisted mainly of CO_2 and H_2O, allowing the carbon dioxide to be easily isolated. The other control variable was the outlet CO_2 flux, maintaining faster OC conversion so that the reactor can be switched to the oxidation stage to generate energy more quickly. The reduction objective function J_{red} is as follows:

$$J_{red} = \int_{t}^{t+t_p} \left(S_{CO_2}(\tau) - S_{CO_2,sp} \right)^2 d\tau + \int_{t}^{t+t_p} \left(G_{CO_2,out}(\tau) - G_{CO_2,sp} \right)^2 d\tau \qquad (3.28)$$

Note that setpoints are used instead of a maximization function to improve the stability of the system.

The CO_2 selectivity's set point ($S_{CO_2,sp}$) is set to 0.9 to ensure that an adequately pure CO_2 stream is produced to facilitate carbon capture [30]. In addition, the CO_2 flux setpoint ($G_{CO_2,sp}$) is 0.12 kg/m^2/s, based on the maximum outlet CO_2 flowrate from a large-scale simulation performed by Han et al. [30]. The setpoint for the CO_2 flux allows a process to quickly regenerate the OC to switch back to the oxidation stage and generate energy. In addition, if the outlet CO_2 is being sold to a manufacturing process [79], this setpoint can be used to ensure that the CO_2 demand is met. The selectivity has a higher magnitude than the CO_2 flux, meaning that with equal weights, NMPC prioritizes the setpoint tracking of the CO_2 selectivity. Various combinations of weights for each term in the objective function were investigated for this system, and using equal weights resulted in good control of the selectivity while maintaining the outlet CO_2 flux reasonably close to the setpoint. In this work, the selectivity objective was prioritized to improve the CO_2 purity of the outlet stream, so using equal weights was deemed to provide the most appropriate compromise between the two objectives. Thus, for this objective function,

no weights are used, although they could be incorporated to adhere to the operational goals of a particular CLC process.

As with the oxidation stage, a baseline was established by simulating CLC with a constant flowrate. In a natural gas combustion plant, the fuel flowrate is usually much lower than the air flowrate; for instance, it might be maintained to the order of 9.4 kg/s, corresponding to a constant mass flux of 0.4 $kg/m^2/s$ in a reactor of this diameter (Table 3.6) [80]. The results of this simulation are presented as the dashed pink lines in Figure 3.11. The NMPC scheme described previously was implemented for the reduction stage. The average computational time to solve each iteration of NMPC was roughly 23 s, which would allow for online implementation with the 30 s sampling interval used for the reduction stage. The results are shown in Figure 3.11 and the subsequent mole fractions are presented in Figure 3.12b.
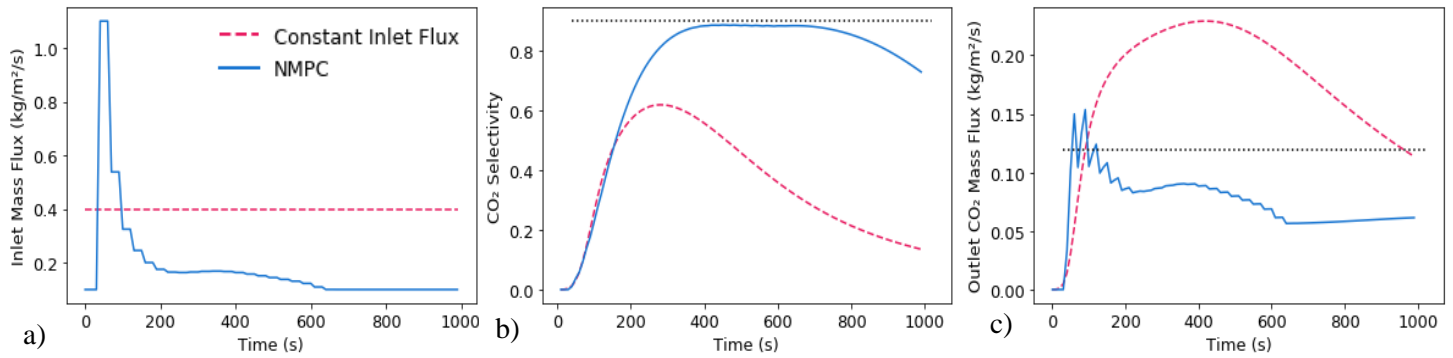
Figure 3.11. a) Inlet mass flux, b) CO_2 selectivity, and c) outlet CO_2 flux profiles using a constant inlet CH_4 flux (dashed pink line); and NMPC scheme (solid blue line).
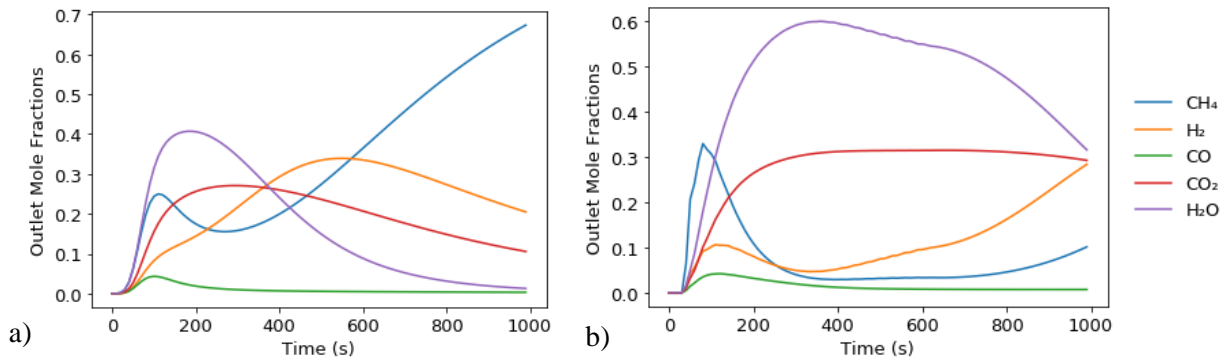
Figure 3.12. Outlet mole fractions of different components during the reduction stage for a) a constant inlet CH_4 flux and b) the optimal control scheme from NMPC.

When NMPC is implemented for the reduction stage, the control actions successfully improve the process output, and there is a particularly notable improvement in the CO_2 selectivity (Figure 3.11b), which stays within 2% of the setpoint for 430 s. As shown in Figure 3.12b, this also results in a much more desirable outlet composition profile, where the $CO_2 + H_2O$ fraction remains above 0.8 for the majority of the reduction stage, improving the purity of the CO_2 stream. This is much more suited to CO_2 capture than the outlet mole fractions obtained from using a constant inlet flowrate, shown in Figure 3.12a, where the carbon dioxide and water are comparatively diluted and the $CO_2 + H_2O$ molar

52

ratio is less than 0.6 for most of the reduction period. As mentioned previously, with equal weighting, deviations in the CO_2 selectivity from the setpoint are inherently penalized more heavily than deviations of the outlet CO_2 flux due to the higher magnitude of the CO_2 selectivity. As a result, although the outlet CO_2 in Figure 3.11c was maintained within 0.05 kg/m^2/s of the setpoint for most of the reduction stage, it did not track the setpoint as well as the selectivity, and the changes in the inlet mass flux resulted in sudden spikes in the outlet CO_2 flux.

As specific combustion plants might have different objectives, the NMPC strategy for the reduction stage was also performed using an alternative objective function. For instance, the outlet CH_4 flux can be controlled to maximize the methane conversion of this stream. This scheme was implemented using a low setpoint for the outlet CH_4 flux (0.01 kg/m^2/s) to reduce the amount of unreacted methane reaching the outlet, represented by Equation 3.29. The results from this scenario are presented in Figure 3.13.

$$J_{red} = \int_t^{t+t_p} \left(G_{CH_4,out}(\tau) - G_{CH_4,sp}\right)^2 d\tau + \int_t^{t+t_p} \left(G_{CO_2,out}(\tau) - G_{CO_2,sp}\right)^2 d\tau \qquad (3.29)$$
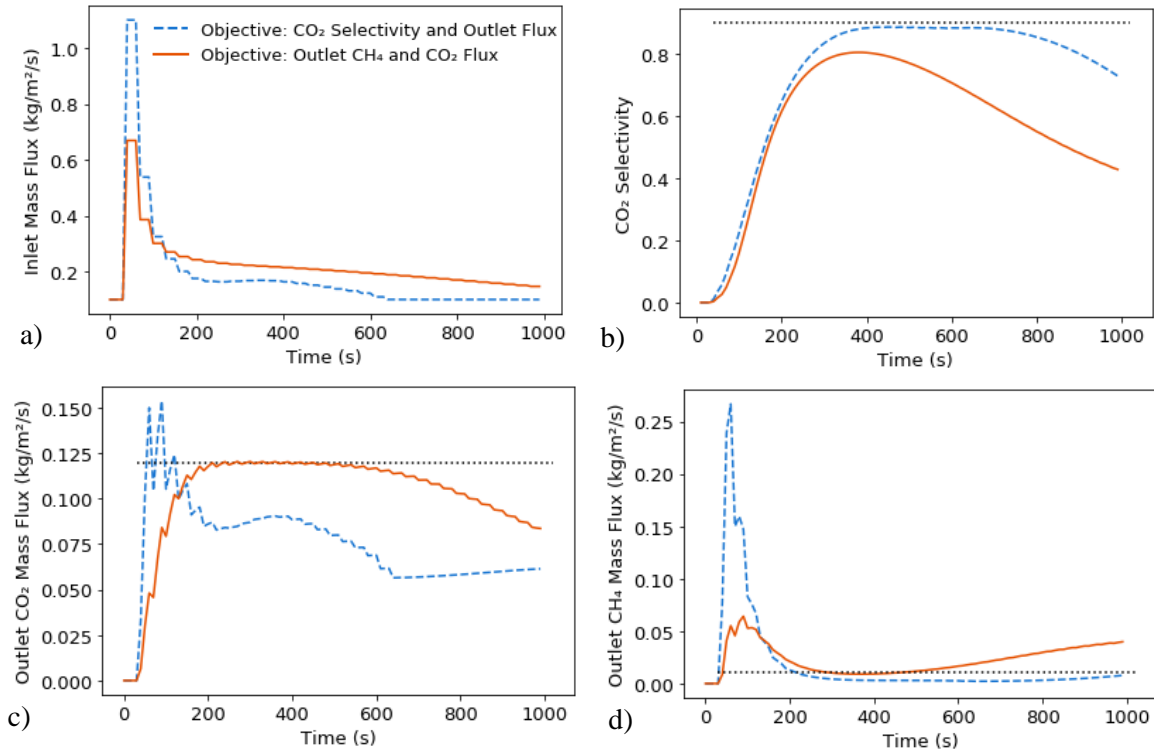
Figure 3.13. a) Inlet mass flux, b) CO_2 selectivity, c) outlet CO_2 flux, and d) outlet CH_4 flux profiles compared from implementing an NMPC scheme where the outlet CO_2 flux and CO_2 selectivity are control variables (dashed blue line) and where the control variables are the outlet CO_2 flux and outlet CH_4 flux (solid orange line).

When the outlet CH_4 flux is used as a control variable, the inlet CH_4 is not increased as much as it was when the CO_2 selectivity was one of the control variables (Figure 3.13a). This decreases the unreacted methane in the outlet stream (Figure 3.13d) until the reaction approaches completion at 600 s. In addition, the inlet CH_4 flux decreases more gradually, and the outlet CO_2 flux (Figure 3.13c) can be maintained closer to the setpoint for a longer period of time. The CO_2 selectivity (Figure 3.13b) is consistently much lower (often more than 10% lower) than that observed when the selectivity is used as a control variable. Based on the above, this shows that the NMPC scheme is able to effectively change the control actions to reflect a plant's operatinal goals.

54

3.4 Summary

In this chapter, an NMPC framework for large-scale packed bed CLC processes was presented. A multiscale model was used to represent the bulk gas and particles in the system and was validated against multiple sets of literature data under different designs and operating conditions. In addition, a pseudo-homogeneous model was developed and validated for use as the internal NMPC model, reducing the computational costs incurred by feedback control. The NMPC scheme was implemented for both the oxidation and reduction stages of a large-scale packed bed CLC process. When NMPC was implemented for the oxidation stage, the outlet temperature could be controlled if both the inlet air and inert gas fluxes were manipulated. This resulted in better setpoint tracking than the case using a constant inlet air flux, allowing the process to generate energy for a longer period of time. For NMPC of the reduction stage, the inlet fuel flowrate was manipulated to control the CO_2 selectivity and outlet CO_2 flux. This resulted in a purer outlet CO_2 stream, improving the carbon capture effectiveness of this process.

Chapter 4

Reactor Network Modelling for Biomass-Fueled CL Processes

This chapter presents a reactor network model for biomass-fueled chemical-looping gasification and chemical-looping combustion and employs the model to investigate the performance of different reactor designs. Section 4.1 presents the reactor network, which consists of continuous stirred-tank reactor (CSTR), plug flow reactor (PFR), and packed bed reactor (PBR) zones. Section 4.1.1 introduces the reactor network and the reactions taking place in each zone, and Section 4.1.2 establishes the models for each zone and outlines the interactions between the models. Section 4.2 presents simulation results from this reactor network model. In Section 4.2.2, the model is validated against experimental data under CLG and CLC conditions. In Section 4.2.3, different reactor designs are explored for biomass-fueled CLG to investigate the effect of OC bed placement on the gasification efficiency. Finally, in Section 4.2.4, the OC bed length and placement are modified to explore the impact of different reactor designs on the outlet CO_2 stream purity for biomass-fueled CLC. The outcomes of this chapter have been submitted for publication in a journal.

4.1 Model Development

4.1.1 Reactor Network

To represent the biomass-fueled packed bed CL configuration, a reactor network was developed, as shown in Figure 4.1. The nominal reactor design was based on a common setup in experimental studies, where a small amount of OC is placed on a mesh wire midway through the reactor. The reactor network is accordingly comprised of sequential zones to represent the behaviour in these

different regions: CSTR, PFR, and PBR zones. These zones are connected using boundary conditions to account for the mass and heat transfer between each region. In this system, natural hematite (which is principally found as Fe_2O_3) is used as the oxygen carrier as it is abundant, inexpensive, environmentally friendly, and has sufficient reactivity for CL processes [81] [15].
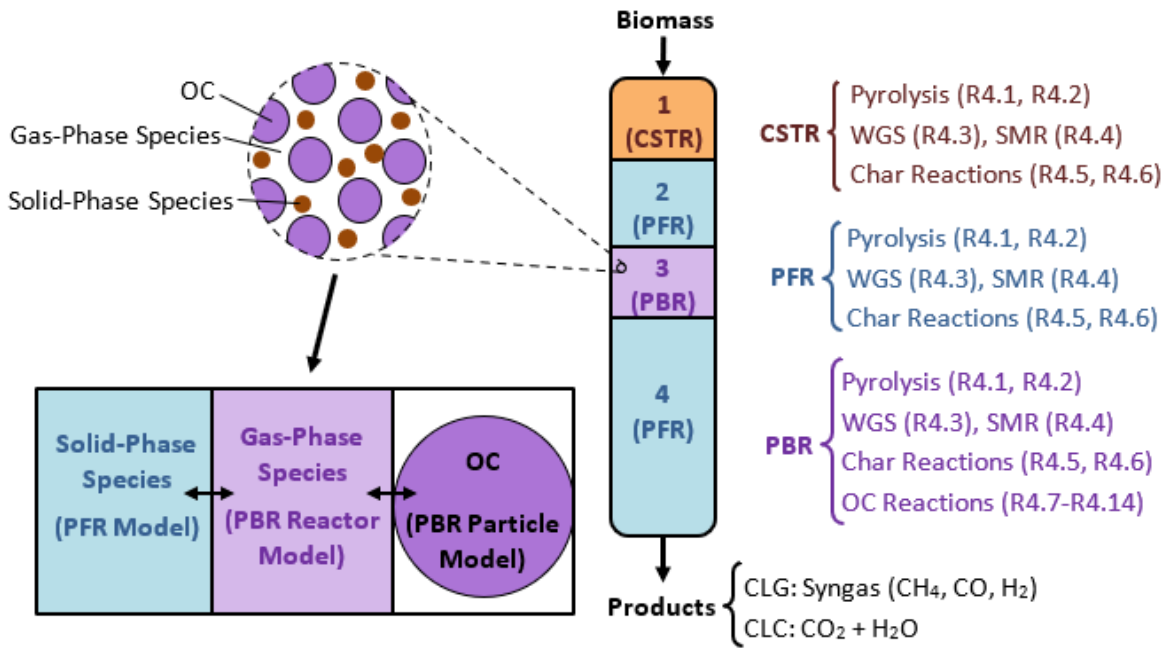
Figure 4.1. Schematic depicting the locations of the zones in the nominal reactor design as well as the reactions taking place in each zone.

As biomass is introduced to the reactor, it quickly devolatilizes through a process called pyrolysis (R4.1 and R4.2 in Table 4.1) [82] [83]. At the reactor inlet (Zone 1 in Figure 4.1), the components are well-mixed and thus are represented by a CSTR. Das et al. [84] and Darido et al. [85] developed reactor networks for similar processes using a CSTR to model the inlet zone where the biomass is introduced to the reactor and undergoes pyrolysis, and found their reactor networks exhibited good agreement with experimental results. The remainder of the network consists of a PBR zone (Zone

3) contained between two PFR zones (Zones 2 and 4). In the PBR zone, the gaseous species are modelled using a traditional PBR model, outlined in Section 4.1.2. The solid fuel particles used in the experiment are smaller than the OC particles [18] and it is assumed that they travel in the void space between the OC, but do not go into the OC pores. Also, it is assumed that the solid species are perfectly mixed in the spaces between the OC particles. A PFR model is used to represent the behaviour of the solid components in this zone. The PFR volume is defined as the volume of void space within OC bed, which is estimated using the volume and bed porosity of the PBR zone [56]. The solid species do not interact directly with the OC, but will react with the gas (Reactions R4.1, R4.2, R4.5 and R4.6 in Table 4.1), influencing the concentrations of the gaseous species which diffuse into the OC and react with the hematite.

The actual kinetics of the pyrolysis reaction, which involves organic compounds breaking down with multiple reaction intermediates, are much more complex than those presented in Reactions R4.1 and R4.2 in Table 4.1. In this work, the pyrolysis reaction is assumed to take place using primary and secondary pyrolysis, shown as R4.1 and R4.2, respectively [86]. In primary pyrolysis, the biomass decomposes into volatile gases, char, and tar. The volatile gases mainly consist of CH_4, CO, CO_2, H_2, and C_2H_4. The secondary pyrolysis represents the tar cracking, which produces additional volatile gases. The stoichiometric coefficients *a-g* in R4.1 and *a-e* in R4.2 are obtained empirically and generalized to be functions of a fuel's ultimate and proximate analysis [17] [87].

Once the biomass is devolatilized, the gaseous products react through a water-gas shift (WGS) reaction and steam-methane reforming (SMR) reaction, R4.3 and R4.4, respectively. The gaseous products also react with the char through the Boudouard and char gasification reactions, R4.5 and R4.6, respectively. Although reactions R4.1-R4.6 are considered for each zone, for Zone 1 the primary

reactions are pyrolysis (R4.1 and R4.2), while Zones 2-4 are focused on the WGS, SMR, and char reactions (R4.3 through R4.6). In Zone 3, where the oxygen carrier is present, the OC reactions (R4.7-R4.14) must also be accounted for, so the reaction rates for R4.1-R4.14 are all evaluated. The reactions, as well as the corresponding kinetic schemes, are listed in Table 4.1, and the kinetic parameters are presented in Appendix A.

Table 4.1. Reaction kinetics occurring within the biomass-fueled chemical-looping reactor network.

	Reaction Stoichiometry		Reaction Kinetics		Source
Pyrolysis	Biomass $\rightarrow a$CH$_4$ + bH$_2$ + cCO + dCO$_2$ + eC$_2$H$_4$ + fChar + gTar	(R4.1)	$r_1 = k_{0,1} e^{-\frac{E_{a,1}}{R_g T}} C_{biomass}$	(4.1)	[45]
	Tar $\rightarrow a$CH$_4$ + bH$_2$ + cCO + dCO$_2$ + eInertTar	(R4.2)	$r_2 = k_{0,2} e^{-\frac{E_{a,2}}{R_g T}} C_{tar}$	(4.2)	[45]
WGS	CO + H$_2$O $\leftrightarrow$ CO$_2$ + H$_2$	(R4.3)	$r_3 = -k_{0,3} \left(e^{-\frac{E_{a,3}}{R_g T}} C_{H_2}^{0.5} C_{CO_2} - \frac{1}{K_3} e^{-\frac{E_{a,3}}{R_g T}} C_{H_2O} C_{CO} \right)$	(4.3)	[88]
SMR	CH$_4$ + H$_2$O $\rightarrow$ CO + 3H$_2$	(R4.4)	$r_4 = k_4 C_{CH_4} C_{H_2O}$	(4.4)	[89]
Char Reactions	C + CO$_2$ $\rightarrow$ 2CO	(R4.5)	$r_{5,char} = \frac{k_5 K_{5,CO_2} P_{CO_2}}{1 + K_{5,CO_2} P_{CO_2} + K_{5,CO} P_{CO}}$ $\times \rho_c \epsilon_s \frac{S_0}{1 - \epsilon_0} (1 - X_{char})^{2/3}$	(4.5)	[90]

	$C + H_2O \rightarrow CO + H_2$ (R4.6)	$r_{6,\text{char}} = \dfrac{k_6 K_{6,H_2O} P_{H_2O}}{1 + K_{6,H_2O} P_{H_2O} + K_{6,H_2} P_{H_2}}$ $\times \rho_c \epsilon_s \dfrac{S_0}{1 - \epsilon_0} (1 - X_{char})^{2/3}$	(4.6)	[90]
OC Reactions	$3Fe_2O_3 + 2CH_4 \rightarrow$ $Fe_3O_4 + 3FeO + 4H_2 +$ $2CO$ (R4.7)	$r_j = \dfrac{k_j R_o}{2MW_{O_2}} \rho_s \epsilon_s \left(Y_{Fe_2O_3} \right.$ $\left. + Y_{Fe_3O_4} \times \dfrac{12MW_{Fe_2O_3}}{8MW_{Fe_3O_4}} \right)$ $\times (1 - X) \dfrac{Y_{CH_4}}{Y_{CH_4,TGA}} \times \dfrac{1}{1000}$ $\times C_i^{n_j}$	(4.7)	[91] [92] [93] [94]
	$8Fe_2O_3 + C_2H_4 \rightarrow$ $4Fe_3O_4 + 4FeO + H_2 +$ $H_2O + CO + CO_2$ (R4.8)			
	$3Fe_2O_3 + CO \rightarrow$ $2Fe_3O_4 + CO_2$ (R4.9)	$r_j = \dfrac{k_j R_o}{2MW_{O_2}} \rho_s \epsilon_s \left(Y_{Fe_2O_3} \right.$ $\left. + Y_{Fe_3O_4} \times \dfrac{3MW_{Fe_2O_3}}{2MW_{Fe_3O_4}} \right)$ $\times (1 - X)^{2/3} \times \dfrac{1}{1000} \times C_{CO}^{n_j}$	(4.8)	[91] [92] [93] [94]
	$Fe_3O_4 + CO \rightarrow 3FeO$ $+ CO_2$ (R4.10)			
	$Fe_3O_4 + 4CO \rightarrow 3Fe$ $+ 4CO_2$ (R4.11)			
	$3Fe_2O_3 + H_2$ $\rightarrow 2Fe_3O_4 + H_2O$ (R4.12)	$r_j = \dfrac{k_j R_o}{2MW_{O_2}} \rho_s \epsilon_s \left(Y_{Fe_2O_3} \right.$ $\left. + Y_{Fe_3O_4} \times \dfrac{3MW_{Fe_2O_3}}{2MW_{Fe_3O_4}} \right)$ $\times (1 - X)^{2/3} \times \dfrac{1}{1000} \times C_{H_2}^{n_j}$	(4.9)	[91] [92] [93] [94]
	$Fe_3O_4 + H_2 \rightarrow 3FeO$ $+ H_2O$ (R4.13)			
	$3FeO + H_2O \rightarrow Fe_3O_4$ $+ H_2$ (R4.14)	$r_{14} = \alpha_{14} k_{14} C_{H_2O}^{n_{14}} (1$ $- X) \left(-\dfrac{\ln(1 - X)}{k_{14} C_{H_2O}^{n_{14}}} \right)^{\alpha_{14} - 1/\alpha_{14}}$	(4.10)	[95]

Within the reactor zones, the mass and energy balances account for the convection and reactions taking place. Additionally, the PBR zone considers the axial dispersion, diffusion within the particle, and interactions between the bulk gas and the particle. To account for the heat being supplied to the reactor, which is very common in CLG setups, an additional term was included to model the heat transfer between the gas inside the reactor and the reactor wall. Further details pertaining to the reactor model for each zone are presented in Section 4.1.2.

4.1.2 Reactor Models

The heat and mass balances for the CSTR, PFR, and PBR zones are presented in this section. Overall assumptions used in the development of the model are:

- The gaseous and solid feed streams are perfectly mixed and evenly distributed throughout the reactor's diameter (plug flow)

- The gas velocity is constant throughout the reactor

- There is negligible heat loss through the reactor walls

- The biomass fuel is introduced to the reactor at a constant rate throughout the reduction stage

- The effect of trace pollutants in the biomass (S, N, etc.) is neglected

The reactor is modelled over the time domain t ($0 \leq t \leq t_f$, where t_f is the final time of the stage), the axial domain z ($0 \leq z \leq L$, where L is the reactor length), and in the packed bed reactor zone, the radial domain r_c ($0 \leq r_c \leq R_p$, where R_p is the particle radius). In each zone, the behaviour is modelled for the gaseous components (CH_4, H_2, CO, CO_2, H_2O, C_2H_4, and N_2) as well as the solid compounds (biomass, char, ash, tar, and inert tar).

At any point in the time domain, the reactor network follows a sequential configuration; hence, the outlets of one zone are passed on as the inlets for the subsequent zone. The zones and locations within the reactor can be varied, to ensure that the reactor network can be used to represent different reactor designs. Therefore, the model can be used for both the CLG and CLC processes by changing the amount of OC used within the system. The model for each zone is outlined in further detail in the following subsections. The notation used is defined in the nomenclature section. Additional information pertaining to the model, including additional algebraic correlations and parameter values, are presented in Appendix A.

4.1.2.1 CSTR Zone

The inlet CSTR zone (Zone 1) is modelled using the mass and energy balances represented below:

$$\frac{\partial N_i}{\partial t} = F_{i,0} - F_i + V \sum_{j=1}^{n_r} r_{i,j} \tag{4.11}$$

$$N_T C_{pf} \frac{\partial T}{\partial t} = (T_{in} - T) F_T C_{pf} + V \sum_{j=1}^{n_r} (-\Delta H_j) r_j - h_w \frac{4}{D} (T - T_w) \tag{4.12}$$

It is assumed that the total molar flowrate F_T and heat capacity C_{pf} from the reactor inlet and outlet are constant. Equation 4.11 represents the mass balance for the CSTR and considers the mass flow into and out of the zone, as well as the reactions taking place. These balances are computed for all 12 components i (CH_4, H_2, CO, CO_2, H_2O, C_2H_4, N_2, biomass, char, ash, tar, and inert tar), and the reaction rates are calculated for the 6 reactions taking place in the CSTR zone (R4.1-R4.6). The energy balance (Equation 4.12) considers the heat flow through the zone, the heat released through the reactions, and the heat transfer with the reactor wall.

4.1.2.2 PFR Zones

The PFR zones (Zones 2 and 4) are modelled using the balances presented, depicting the convection through the reactor and the reactions taking place:

$$\frac{\partial C_i}{\partial t} + \frac{\partial F_i}{\partial V} = \sum_{j=1}^{n_r} r_{i,j} \tag{4.13}$$

$$C_{pf} C_T \frac{\partial T}{\partial t} + C_{pf} F_T \frac{\partial T}{\partial V} = \sum_{j=1}^{n_r} (-\Delta H_j) r_j - h_w \frac{4}{D} (T - T_w) \tag{4.14}$$

Equation 4.13 is the mass balance for the PFR and models the axial convection and reactions taking place in the zone. As with the CSTR zone, the mass balance is computed for all 12 components, and the reaction rates for R4.1-R4.6 are evaluated. Equation 4.14 considers the convection, heat released through the reactions, and the heat transfer between the gas and the reactor wall.

4.1.2.3 PBR Zones

The packed bed reactor zone (Zone 3) consists of a small layer of oxygen carrier in the reactor; the height and location of the OC bed are varied for different simulations. The oxygen carrier contains active metal, which undergoes the redox reactions, as well as impurities in the natural hematite, which are inert. There are some additional assumptions pertaining to the OC particles in this zone:

- The active metal is evenly spread across perfectly spherical OCs

- The OCs are uniformly distributed through the PBR

- The OC macroscopic structure is not affected by the reactions occurring

- The gas within the particle is at the same temperature as the surrounding solid

- Thermal conductivity of the gas is negligible compared to that of the solid

- The size of the solid fuel species is small compared to the size of the solid OC particles [18] so that the fuel particles can travel through the spaces between the OC particles

- The solid fuel particles do not react with the OC

- The solids (char, ash, etc.) in the packed bed reactor zones are perfectly mixed in the regions between the OC particles

- The movement of solids through the void spaces in the bed can be accurately represented by a PFR model (Equation 4.13), as shown in Figure 4.1

- The solid fuel particles are at the same temperature as the surrounding gas at that point in the reactor

- No solids or tar accumulate on the surface of the OC or within the pores of the OC particles

The model is comprised of partial differential equations (PDEs) representing the mass and energy balances at the reactor and particle scales, presented in Table 4.2.

Table 4.2. Reactor-scale and particle-scale mass and energy balances employed in the packed bed reactor zones of the reactor network.

Reactor Mass and Energy Balances		
Mass Balance	$\varepsilon_b \dfrac{\partial C_i}{\partial t} + \dfrac{\partial F_i}{\partial V} = \dfrac{\partial}{\partial z}\left(D_{ax,i}\dfrac{\partial C_i}{\partial z}\right) + \varepsilon_b \sum_{j=1}^{n_r} r_{i,j} + k_{c,i}a_v(C_{c,i}\vert_{R_p} - C_i)$	(4.15)
Energy Balance	$\varepsilon_b C_{pf} C_T \dfrac{\partial T}{\partial t} + C_{pf} F_T \dfrac{\partial T}{\partial V}$ $= \dfrac{\partial}{\partial z}\left(\lambda_{ax}\dfrac{\partial T}{\partial z}\right) + \varepsilon_b \sum_{j=1}^{n_r}(-\Delta H_j)r_j + h_f a_v(T_c\vert_{R_p} - T) - h_w\dfrac{4}{D}(T - T_w)$	(4.16)
Particle Mass and Energy Balances		

Mass Balance	$$\varepsilon_c \frac{\partial C_{c,i}}{\partial t} = \frac{1}{r_c^2} \frac{\partial}{\partial r_c} \left(D_{e,i} r_c^2 \frac{\partial C_{c,i}}{\partial r_c} \right) + \varepsilon_c \rho_s \sum_{j=1}^{n_r} r_{i,j}$$	(4.17)
Energy Balance	$$\left((1 - \varepsilon_c) \rho_s C_{ps} + \varepsilon_c C_{pf} C_T \right) \frac{\partial T_c}{\partial t} = \frac{\lambda_s}{r_c^2} \frac{\partial}{\partial r_c} \left(r_c^2 \frac{\partial T_c}{\partial r_c} \right) + \varepsilon_c \rho_s \sum_{j=1}^{n_r} (-\Delta H_j) r_j$$	(4.18)
Particle Conversion	$$\frac{dX}{dt} = \frac{\sum_{j=1}^{n_r} \nu_j r_{Fe_2O_3,j}}{C_{Fe_2O_3,0}}$$	(4.19)

Equations 4.15 and 4.16 represent the mass and energy balances of the bulk gas in the reactor, including the axial convection, dispersion, bulk gas reactions (R4.1 through R4.6), and transfer with the particle. These reaction rates are functions of the concentrations of both the bulk gas and the solid species at that location in the PBR (Equations 4.1-4.6 in Table 4.1). The particle mass and energy balances are presented in Equations 4.17 and 4.18, and take into account the diffusion and reactions taking place within the particle (R4.7 to R4.14). At the particle surface, there is mass and heat transfer with the bulk gas, using the same boundary conditions presented in Chapter 3 (Equations 3.3-3.5 and 3.8-3.10). Furthermore, Equation 4.19 measures the rate of conversion of Fe_2O_3, factoring in the OC reaction rates, reaction stoichiometry, and initial amount of active metal. The mass balances in Equations 4.15 and 4.17 are computed for a subset of the 12 species in the reactor, consisting of the 7 gaseous components i (CH_4, H_2, CO, CO_2, H_2O, C_2H_4, and N_2).

The solid species passing through the PBR are assumed to be perfectly mixed in the void space between the OC particles and are represented by a PFR model, using Equation 4.13. This mass balance is only evaluated for the 5 solid components i (biomass, char, ash, tar, and inert tar). The solids do not interact directly with the OC particles or the gas within the OC particles' pores, but will react with the gaseous species in the void space. The reaction term in Equation 4.13 calculates the reaction rates for

65

R4.1, R4.2, R4.5, and R4.6, which are influenced by the concentrations of the solid, as well as the concentrations of CO_2 and H_2O calculated in the bulk gas model. These reaction rate terms couple the bulk gas (Equation 4.15) and solid PFR (Equation 4.13) mass component balances, as the reaction rates are functions of the concentrations of both the gaseous and solid species, and calculate the consumption and generation of the gases and solids.

The temperature of the bulk gas in the PBR zone is calculated using Equation 4.16, and it is assumed that the solid species are at the same temperature as the gas at that position in the reactor. This assumption is justified by the very small size of the solids carried by the bulk gas, as well as the heat transfer with the reactor wall, which is the dominant term in the bulk gas energy balance.

The reactor network is built to be flexible, such that it can be employed to test a wide variety of design and operating conditions. The reactor design can be changed by varying the number of zones in the reactor, as well as the lengths and locations of the zones. In addition, because the model is validated under both CLG and CLC conditions, the reactor network can be used to simulate both processes. Furthermore, since the pyrolysis coefficients are generalized to be functions of the compound's ultimate and proximate analyses, this model can be implemented for various kinds of biomass fuel.

4.2 Results and Discussion

4.2.1 Implementation

The method of lines was implemented to solve the PDEs that conform the reactor network model described in Section 4.1. The length and location of each zone, as well as the operating conditions and inlet biomass flowrate, are specified to calculate the concentrations, temperature, and OC

conversion at any point during the process. The CSTR (Equations 4.11 and 4.12) outlet states were computed and passed to the subsequent zones. The PFR (Equations 4.13 and 4.14) and PBR (Equations 4.15-4.19) zones in the reactor were discretized in the axial direction using orthogonal collocation of finite elements, using 5 interior Radau collocation points in each element. The number of elements was scaled uniformly for different designs, based on the length of each zone (i.e., OC bed height and location). The nominal reactor design is taken to be the design presented in Figure 4.1, using an OC bed of length 0.5 mm placed partway through the reactor. The design parameters and nominal operating conditions are those used by Liu et al. [18] in their experiment, shown in Table 4.3. For the nominal design, there were 2 finite elements in each PFR and PBR zone (6 elements total). In addition, centered finite differences was applied to the particle model in the PBR zone, using 6 segments. The resulting network of ODEs and PDEs consists of 2905 spatially-discretized states for the nominal reactor design, and was solved through the solve_ivp function in Python using the implicit 5th order Radau IIA Runge-Kutta method [96].

4.2.2 Validation

In order to validate the reactor network, simulations were performed under two different sets of experimental conditions. To ensure that the model provided reasonable predictions under conditions for biomass-fueled CLG and CLC, it was compared to experimental data obtained for both CLG and CLC. For CLG, the experimental data was obtained by Liu et al. [18] at a variety of conditions. Due to the limited availability of data for biomass-fueled CL in packed beds, experimental data reported by Huang et al. [17] in a fluidized bed was considered for CLC. In both cases, the CSTR zone (Zone 1) was taken to be 10% of the reactor length, as the first 10% of this reactor was found to be the region where most of the biomass underwent pyrolysis [97]. The length of the PBR zones (Zone 3) was

estimated based on the mass of the OC used in the experiment using the particle density and bed porosity to calculate the volume occupied by the oxygen carrier. The operating conditions used in each experiment are presented in Table 4.3, and the proximate and ultimate analyses are presented in Table A.8 in Appendix A. The results at the conditions used by Liu et al. and Huang et al. are presented in Figure 4.2 and Figure 4.3, respectively.

Table 4.3. Experimental conditions employed by Liu et al. for CLG and by Huang et al. for CLC.

Parameter	Liu [18] (CLG)	Huang [17] (CLC)
Reduction Time	30 min	50 min
Reactor Length	0.3 m	1 m
Reactor Diameter	26 mm	60 mm
CSTR Zone (Zone 1) Length	10% (0.03 m)	10% (0.1 m)
PBR Zone (Zone 3) Length	0.5 mm	3.7 cm
Location of PBR Zone (height within the reactor)	0.15 m	0.7 m
Concentration of Active Metal (kg Fe_2O_3/kg OC)	0.9	0.9
OC Diameter	180 μm	250 μm
Inlet Temperature	850 °C	840 °C
Inlet Pressure	1 atm	1 atm

Biomass Flowrate	2 g/hr	0.12 kg/h
Biomass Type	Pine Wood	Pine Sawdust
Gas Flowrate	200 mL/min	200 L/h
Gas Composition	Nitrogen	Argon
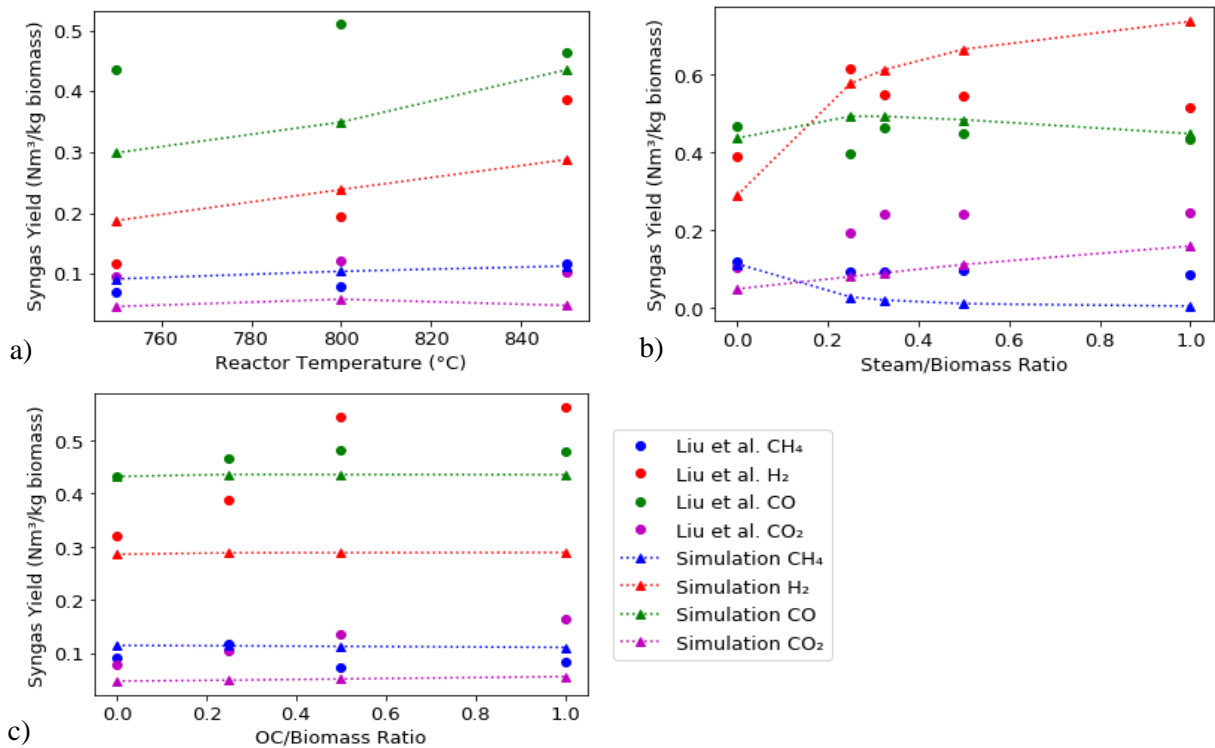
Figure 4.2. Comparison between the syngas yields of different components obtained through Liu et al.'s experiment and through the proposed model while varying a) the reactor temperature, b) the steam/biomass ratio, and c) the OC/biomass ratio.
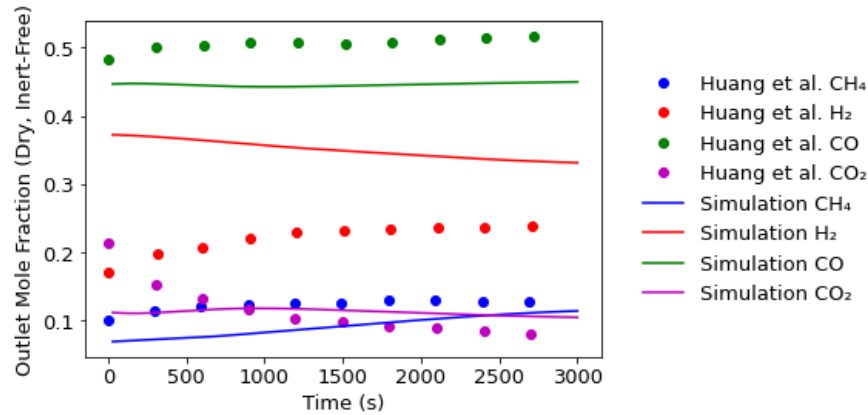
Figure 4.3. Comparison between experimental data from Huang et al. and simulation results for the dynamic profiles of the outlet dry, inert-free, mole fractions for biomass-fueled CLC.

As shown in Figure 4.2, the results have similar trends to those obtained in the experiment performed by Liu et al. when the temperature (Figure 4.2a) and steam/biomass ratio (Figure 4.2b) are modified. When the temperature is increased, the reactions occur more quickly, increasing the gas yield; in particular, the yields of H_2 and CO, which are products of the char gasification reactions. While increasing the steam/biomass ratio, it can be observed that the introduction of steam to the system significantly increases the H_2 yield, as the presence of steam increases the char gasification and SMR reaction rates, both of which produce H_2. As the oxygen carrier to biomass ratio is increased (Figure 4.2c), the model does not predict large changes for these amounts of OC. The main discrepancy between the model predictions and experimental results was the hydrogen yield, as the change in yield was overpredicted with higher concentrations of steam, and underpredicted when the OC/biomass ratio was increased. The discrepancy in Figure 4.2c could be related to the catalytic effect of Fe_2O_3 on secondary pyrolysis. Hematite is known to have a catalytic effect on tar cracking, which would increase the amount of hydrogen released through secondary pyrolysis – a phenomenon that lies outside of the scope

70

of this work [98] [99]. In addition, in Liu et al.'s work, the mass of the OC was reported, which was used in this work to approximate the height of the OC bed in the reactor network. This was calculated using the particle density and bed porosity, which were estimated from other sources [91] [56], and introduces uncertainty to the bed height implemented in the reactor network.

When compared to Huang et al.'s experimental CLC results (Figure 4.3), the model predicts similar magnitudes of the resulting outlet mole fractions. The predicted dynamic profiles for H_2 and CO_2 don't exhibit the same trends as the experimental data, which can be attributed to the different flow regime used in Huang et al.'s experiment. The agitation of OC in fluidized beds improves the gas-solid contact, thereby accelerating the observed OC reaction rates at the beginning of the reduction stage [100] [101]. Faster OC kinetics would result in higher CO_2 production, and would consume more H_2, accounting for the discrepancy between the experimental data and simulation results. Despite the differences between the experimental and simulation conditions (e.g., the OC bed height and flow regime), the model agrees with the experimental results since it captures the expected performance of this system under the design and operating conditions considered in this study.

To further validate the model, a sensitivity analysis was performed for biomass-fueled CLC using a full packed bed reactor with steam as the inlet gas (i.e. modelling the entire reactor as Zone 3, as represented in Figure 4.6c in Section 4.2.4). These results are presented in Figure C.2 and Figure C.3 in Appendix C, and show that increasing the temperature (Figure C.2a and Figure C.3a) increases the OC conversion rate and gas yields, particularly the yield of CO_2. This reflects the expected increase in reaction rates at higher temperatures. Experimental studies have reported an increase in the endothermic char reaction rates R4.5 and R4.6 [18] [40] at higher temperatures, which is reflected in the higher CO and H_2 yields, as well as the increase in the amount of char which reacts to form syngas. In addition,

higher temperatures increase the OC reaction rates, which increases the production of CO_2 and H_2O [91]. Increasing the inlet biomass flowrate (Figure C.2b and Figure C.3b) results in a proportional increase in the gas yields; thus the specific gas yields, which are normalized by the biomass flowrate (Nm^3/kg biomass), are not significantly affected. However, increasing the inlet biomass flowrate speeds up the rate of OC conversion as the OC is introduced to greater quantities of fuel. Furthermore, when the inlet steam flowrate is increased (Figure C.2c and Figure C.3c), the residence time of the fuel within the reactor is reduced, decreasing the observed OC conversion and gas yields [10]. The results from this sensitivity analysis were consistent with expectations, and this model was used to investigate the reactor design in the following sections.

4.2.3 CLG Configuration

The reactor network configuration presented in Figure 4.1 was subsequently used to test various reactor designs by changing the length of the OC bed and location of OC within the reactor. For CLG, a reactor design that can generate large quantities of high-quality syngas is desirable. The quantity of syngas is denoted by the specific syngas yield G_v (in Nm^3/kg biomass), and the quality is determined based on the lower heating value (LHV, MJ/Nm^3), i.e.,

$$LHV = 10.82y_{H_2} + 12.64y_{CO} + 35.88y_{CH_4} + 59.44y_{C_2H_4} \,, \tag{4.20}$$

where y_i represents the mole fraction of component i in the outlet syngas. To quantify the tradeoffs between the syngas quality and quantity produced, the gasification efficiency η_{gas} was computed as follows:

$$\eta_{gas} = \frac{LHV \times G_v}{Q_{net}} \times 100\% \,, \tag{4.21}$$

where Q_{net} is the LHV of the biomass feedstock. Note that the lower heating value is used in this calculation for consistency with existing literature [18] [45]. Using these quantities, the performance of different reactor designs can be compared. The reactor designs investigated are presented in Figure 4.4, where the nominal reactor design is taken to be the one operating under the conditions used by Liu et al. [18], previously depicted in Table 4.3. The amount of OC used in each design with a PBR zone was kept constant at 0.5 mm (OC/biomass ratio of 0.25 for the half hour reaction time), as this was found to have the highest gasification efficiency (Figure C.1c in Appendix C). The location of the OC was changed in cases CLG-A, CLG-C, CLG-D, and CLG-E to determine the OC placement that would result in the highest gasification efficiency. To further improve the gasification efficiency, steam was added to the reactor, as show in Figure 4.4 (CLG-F). The steam/biomass (S/B) ratio was chosen based on the S/B ratio which provided the highest gasification efficiency during the validation presented in Section 4.2.2. It was found that an S/B ratio of 1 resulted in the highest gasification efficiency (Figure C.1b in Appendix C). The results from these tests are presented in Table 4.4.
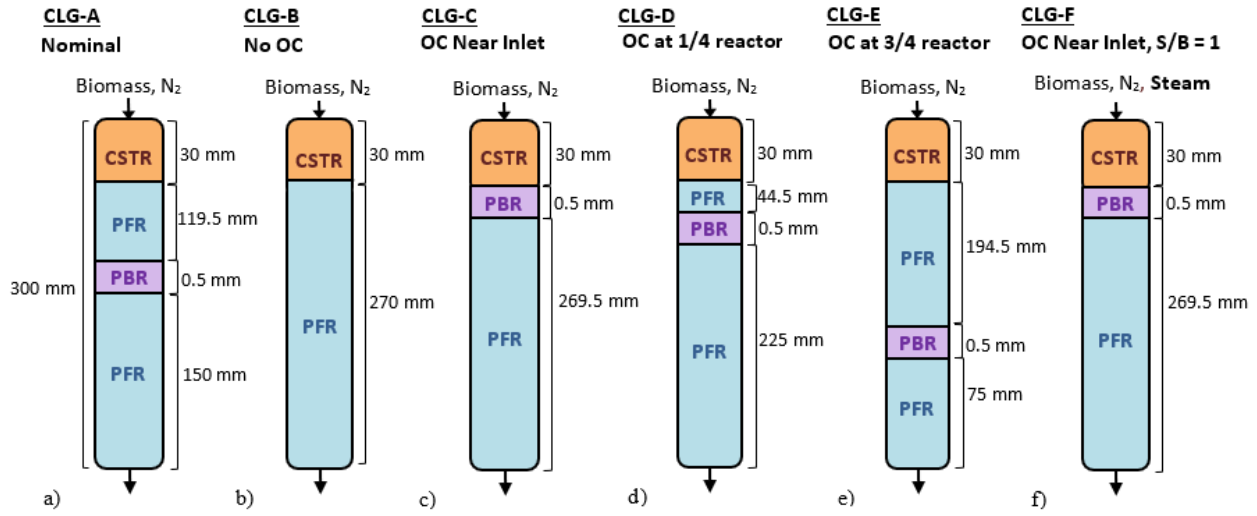
Figure 4.4. Different reactor designs to investigate the reactor performance of biomass-fueled CLG.

Table 4.4. Cumulative mole fractions (dry, inert-free) and gasification performance for different reactor designs presented in Figure 4.4.

Configuration	Reactor Design	Mole Fractions (Dry, Inert-Free)				G_v (Nm³/kg biomass)	LHV (MJ/Nm³)	η_{gas} (%)
		CH₄	H₂	CO	CO₂			
CLG-A	Nominal (OC at reactor midpoint)	0.128	0.326	0.492	0.054	0.8890	14.32	68.84
CLG-B	No OC	0.130	0.325	0.492	0.053	0.8773	14.39	68.25
CLG-C	OC Near Inlet	0.128	0.326	0.493	0.053	0.8895	14.34	68.96
CLG-D	OC ¼ of the way through reactor	0.127	0.326	0.493	0.053	0.8898	14.33	68.93
CLG-E	OC ¾ of the way through reactor	0.128	0.325	0.491	0.056	0.8871	14.32	68.69
CLG-F	OC Near Inlet, S/B = 1	0.003	0.548	0.332	0.117	1.3569	10.24	75.09

As shown in Table 4.4, by adding the oxygen carrier to the system (case CLG-A), the LHV of the resulting gas will be lower (more of the H_2 and CO react, reducing the combustion potential) than in CLG-B, where there is no OC in the reactor. However, adding OC increases the char conversion in the reactor, increasing the syngas yield, and thus the gasification efficiency. In CLG-A, the addition of OC does not increase the gasification efficiency as much as the improvement reported in experimental data; this might be a result of the catalytic effect of the oxygen carrier, which is not accounted for in the model [98] [99]. Changing the location of the OC bed (CLG-A, CLG-C, CLG-D, and CLG-E) showed that keeping the OC closer to the inlet (CLG-C) had a higher gasification efficiency. Figure 4.5 shows the axial concentration profiles within the reactor using the nominal design from CLG-A (Figure 4.5a) and using CLG-F, where the OC is placed near the inlet with a steam/biomass ratio of 1 (Figure 4.5b). The CO_2 and H_2O concentrations increase quickly at the oxygen carrier bed due to the OC reactions taking place (R4.7-R4.14); this means that when the OC is placed closer to the reactor outlet, the resulting gas will have more CO_2 and H_2O (and reduced combustion potential). Instead, placing an OC bed near the reactor inlet will produce CO_2 and H_2O earlier on, which can react with the char (R4.5 and R4.6) to form CO and H_2, increasing both the combustion potential and syngas yield. Accordingly, the gasification efficiency in CLG-C and CLG-D is higher than in CLG-A and CLG-E, where the OC is placed closer to the reactor outlet. The highest gasification efficiency is observed in CLG-C, when the OC bed is placed directly after the CSTR zone, and this value is of similar magnitude to that observed in biomass-fueled CLG experiments [18]. Moreover, adding a small amount of steam to the reactor inlet (CLG-F) can further increase the char gasification reaction rate (R4.6), increasing the syngas yield and H_2 yield. Adding more steam would introduce too much oxygen to the system, decreasing the CH_4 and CO yields and decreasing the gasification efficiency. It was found that using a

75

small OC bed (OC/biomass ratio 0.25) placed near the inlet and introducing a small amount of steam (steam/biomass ratio of 1) to the reactor resulted in the highest gasification efficiency for biomass-fueled CLG.
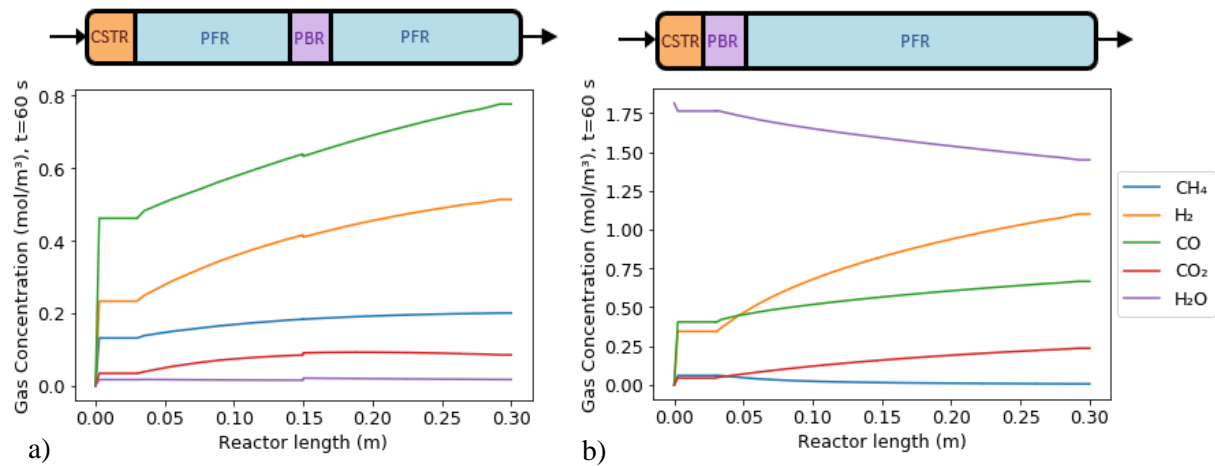
Figure 4.5. Axial gas concentration profiles after one minute of reaction, shown for a) nominal conditions (CLG-A), and b) OC bed placement near the inlet using a steam/biomass ratio of 1 (CLG-F).

4.2.4 CLC Configuration

The reactor network model was also used to investigate the feasibility of using biomass as a fuel for packed bed CLC. In this case, the goal is to generate a stream which mainly consists of CO_2 and H_2O such that the CO_2 can be easily isolated. Accordingly, the quantity of interest for CLC is the dry outlet CO_2 fraction, to ensure that when H_2O is removed from the stream, the remaining gas consists of concentrated CO_2. The reactor designs tested are presented in Figure 4.6, and the corresponding simulation results are shown in Table 4.5.
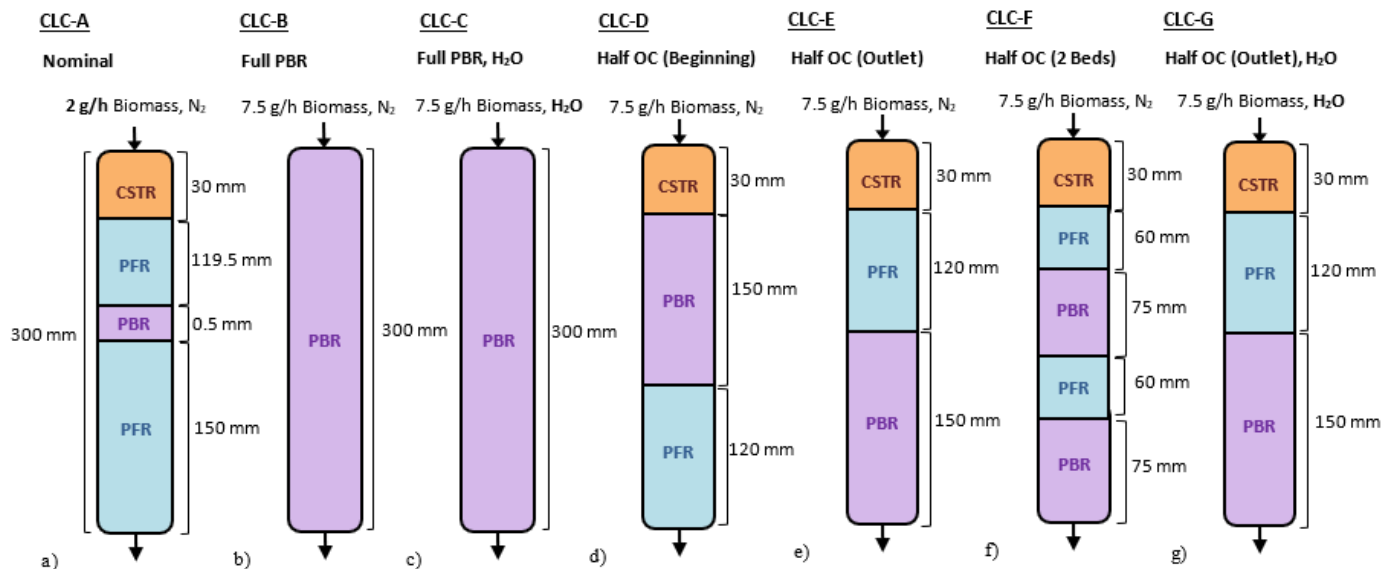
Figure 4.6. Reactor designs to investigate the reactor performance of biomass-fueled CLC.

Table 4.5. Cumulative outlet mole fractions (dry, inert-free) and outlet H_2O fractions of the product gas for CLC with reactor designs presented in Figure 4.6.

Configuration	Reactor Design	Mole Fractions (Dry, Inert-Free)				H_2O Overall Fraction
		CH_4	H_2	CO	CO_2	
CLC-A	Nominal	0.128	0.326	0.492	0.054	0.001
CLC-B	Full PBR	0.028	0.076	0.144	0.752	0.111
CLC-C	Full PBR, Inlet H_2O	0.002	0.067	0.111	0.820	0.718
CLC-D	Half OC (inlet)	0.012	0.300	0.379	0.310	0.049
CLC-E	Half OC (outlet)	0.057	0.141	0.156	0.646	0.080
CLC-F	Half OC (2 OC beds)	0.029	0.173	0.159	0.639	0.059

| CLC-G | Half OC (outlet), Inlet H_2O | 0.001 | 0.308 | 0.081 | 0.611 | 0.405 |

As with CLG, the conditions from Liu et al. [18] presented in Table 4.3 were used as the nominal conditions, to establish a basis of comparison for CLC. To improve the performance of biomass-fueled CLC, in case CLC-B (presented in Figure 4.6), more oxygen was added to the system by using a reactor completely packed with OC, where the reactor network consists of a single PBR zone. To accommodate the increased amount of OC, a higher biomass flowrate of 7.5 g/h was used for all cases except for CLC-A. Steam was used as the carrying gas in CLC-C and CLC-G to further increase the amount of oxygen present for combustion. Additionally, a set of scenarios (CLC-D to CLC-G) were investigated using half the amount of OC in the reactor. With less OC, the combustion products have a smaller outlet fraction of CO_2; these cases were investigated to determine which reactor designs make the most effective use of the OC if a limited amount of OC is available for use.

As shown in Table 4.5, when a full PBR is used with N_2 used as the inlet gas (CLC-B), the OC provides enough oxygen to produce a relatively pure CO_2 stream, with an outlet dry CO_2 fraction of 0.752. Experimental studies for CLC often report CO_2 fractions of approximately 0.1-0.2 [17] [27], suggesting that using more OC can significantly improve the outlet CO_2 purity in CLC. Additionally, when steam is used as the inlet gas instead of an inert gas (CLC-C), the CO_2 fraction is even higher – the dry outlet gas has a CO_2 fraction of 0.82, and the overall outlet gas has an H_2O fraction of 0.718. Therefore, approximately 95% of the outlet gas is CO_2 or H_2O. This outlet CO_2 fraction is improved by an order of magnitude compared to experimental CLC studies [17] [27], and is adequately pure for effective carbon capture through CLC [30]. Using steam as the inlet gas has the added advantage that there is no inert gas in the outlet stream, facilitating the isolation of CO_2.

When half the amount of OC is used (CLC-D to CLC-G), the outlet CO_2 fraction is lower, as there is less oxygen introduced to the system. As observed using CLG conditions, once CO_2 and H_2O are produced from the OC reactions, they will react with char through the Boudouard and char gasification reactions R4.5 and R4.6. Therefore, to maintain the maximum outlet CO_2 and H_2O fractions, all of the OC should be placed as close to the reactor outlet as possible (CLC-E).

Using half of the full OC bed, if steam is used as the inlet gas (CLC-G), the outlet CO_2 fraction decreases despite the addition of more oxygen to the system. This is because more steam will increase the production of H_2 from the SMR and char gasification and reactions R4.4 and R4.6, increasing the overall gas yield and diluting the outlet fraction of CO_2. However, by removing the inert gas from the system, the resulting CO_2 would be easier to isolate. This case was further investigated by examining the dynamic profiles, shown in Figure 4.7.

In addition to providing insights regarding reactor configuration, this reactor network model can be used to investigate the dynamics of biomass-fueled CLC. This can be useful to determine when the OC has reached complete conversion, to ensure that the reduction stage can be finished before higher quantities of unreacted gas (H_2, CO, etc.) dilute the outlet product. This is exemplified in Figure 4.7a and b, which show the dynamic profiles for design CLC-C, where a full PBR is used and steam is the inlet gas. Figure 4.7c and d show the dynamic profiles for CLC-G, when half as much OC is used and placed at the outlet, also using steam as the inlet gas.
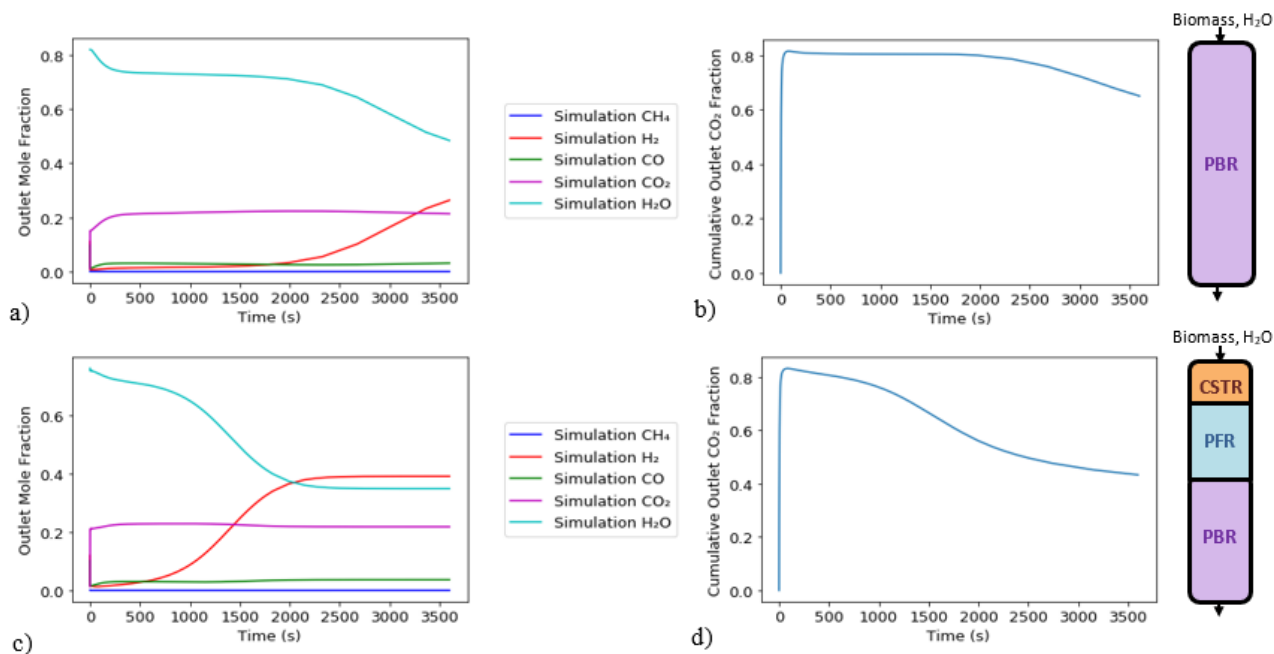
Figure 4.7. Dynamic profiles depicting a) and b) the outlet mole fractions and cumulative outlet CO_2 fraction (respectively) for the case using a full PBR with inlet steam (CLC-C), and c) and d) the outlet mole fractions and cumulative outlet CO_2 fraction (respectively) for the case where half as much OC is placed at the reactor outlet with steam as the inlet gas (CLC-G).

The cases in Figure 4.7 are simulated for 3600 s (as opposed to the 1800 s used to report the outlet mole fractions in Table 4.5). In this case, in Figure 4.7a, it can be seen that the outlet CO_2 and H_2O compositions stay high for 2000 s before the H_2O fraction starts to drop, and the H_2 starts to increase. This corresponds to the cumulative outlet CO_2 fraction shown in Figure 4.7b, which is calculated as the CO_2 fraction in the dry, inert-free syngas that has been produced up to any given time. The cumulative CO_2 fraction stays steady at 0.82 until the hydrogen production starts to increase. To ensure that the overall CO_2 fraction of the product syngas is above 0.8, the reduction stage should be stopped at approximately 2100 s. At this point, most of the OC bed has been at least 90% converted from Fe_2O_3 to Fe_3O_4 (Figure C.4a), meaning that most of the OC bed has been regenerated and could generate energy during the oxidation stage.

80

It is beneficial to end the reduction stage once most of the OC has been reduced to Fe_3O_4, as opposed to waiting for it to further reduce to FeO or Fe, due to the relative rates of reaction taking place. Note that the CO can still be converted to CO_2 as the OC is further reduced, causing the outlet CO_2 fraction to remain high after the hematite reaches full conversion. However, it is known that the reaction where hydrogen reacts with magnetite (R4.13) is much slower than the reduction of hematite to magnetite using hydrogen (R4.12) [102] [103]. This indicates that once the hematite has fully reacted, negligible amounts of hydrogen will react to produce H_2O through the OC reactions; hence, the reduction stage should be stopped (~2100 s) to maintain a concentrated outlet CO_2 stream.

For CLC-G (Figure 4.7c and d), where half of the amount of OC is used, the outlet CO_2 composition is elevated for about half as long as when the reactor is fully packed (Figure 4.7a and b), and most of the hematite has been converted at approximately 1000 s into the reduction stage (Figure C.4b). For the remaining 2600 s simulated beyond this point, the outlet hydrogen fraction gradually increases (Figure 4.7c), reducing the outlet CO_2 composition (Figure 4.7d). If the reduction stage is stopped after 1000 s, the overall outlet CO_2 fraction is 0.76 (an improvement compared to the 0.611 reported in Table 4.5 for an 1800 s reduction stage), and most of the hematite will have reached at least 90% conversion in preparation for the oxidation stage.

4.3 Summary

In this chapter, a reactor network model was developed for biomass-fueled CLG and CLC, and used to investigate designs which improve the performance of these processes. The reactor network consists of CSTR, PFR, and PBR zones to represent the behaviour at different locations within the reactor. This model was validated against experimental data obtained under both CLG and CLC conditions, as well as using a sensitivity analysis. Using this validated model, the OC bed lengths and

locations were varied in order to investigate the resulting impact on the performance of these CL processes. For CLG, the results showed that the highest gasification efficiency occurred when the OC was placed near the inlet, using an OC/biomass ratio of 0.25 and a steam/biomass ratio of 1. For CLC, the highest outlet CO_2 fraction was obtained using a reactor which was fully packed with OC and using steam as the inlet gas. In this design, the outlet CO_2 purity was improved by an order of magnitude when compared to experimental data. This reactor network could also be used to simulate the process dynamics in order to determine the most effective time to end the reduction stage of the process.

Chapter 5

Conclusions and Recommendations

5.1 Conclusions

The objective of this thesis is to improve the feasibility of chemical-looping technology to improve the sustainability of energy generation. Specifically, in this work, reactor design and control strategies were determined to improve the energy generation, gasification efficiency, and carbon capture of packed bed CLG and CLC through implementation of NMPC and through reactor network modelling.

A multiscale model for the oxidation and reduction stages of CLC in a PBR was developed and validated against multiple sets of experimental data. By integrating kinetics from different sources, the model provides good predictions of the behaviour of both stages under various sets of operating conditions. A pseudo-homogeneous variant of this model was built and verified in order to offset computational costs, and these models were used simultaneously to implement NMPC for this process. Using the multiscale model as the plant model and the pseudo-homogeneous model as the NMPC model, optimal control strategies were obtained to improve the energy generation and carbon capture effectiveness of this process. The main outcomes from the implementation of NMPC for packed bed CLC are:

- The temperature for packed bed CLC cannot be controlled by manipulating the inlet air flux alone, but by adding an inert gas stream and manipulating this flowrate as well, the temperature can be controlled and exhibits good setpoint tracking.

- The NMPC for the oxidation stage adjusted the control actions appropriately as a means of tracking the setpoint temperature, which was demonstrated at two different setpoints.

83

- Implementing NMPC for the oxidation stage effectively controls the temperature, which increases the energy generation of this process; this also allows for the use of a more concentrated OC, resulting in the possibility of using a more compact reactor.

- Employing NMPC for the reduction stage significantly increases the CO_2 selectivity, improving the carbon capture capacity of the process.

- Multiple objective functions can be implemented for the reduction stage, showcasing the flexibility of the NMPC scheme to meet different carbon capture targets.

In addition, a reactor network for biomass-fueled packed bed chemical-looping gasification and chemical-looping combustion was presented. The network consists of various reactor blocks (CSTR, PFR, and PBR) in series, where the CSTR models the biomass pyrolysis, the PBR model represents the oxygen carrier in the reactor, and the PFR section represents the flow through the reactor in the regions where there is no OC. To validate the model, it was compared against experimental data using a reactor network that mimics the experimental setup, and an additional sensitivity analysis was performed for CLC. The reactor network model gives reasonable predictions under both CLG and CLC conditions, and this validated model was used to simulate biomass-fueled CLG and CLC using different oxygen carrier bed lengths and locations within the reactor. The main findings from these simulations are as follows:

- Placing the OC near the reactor inlet increased the gasification efficiency of packed bed biomass-fueled CLG, because the CO_2 and H_2O produced from the oxygen carrier reactions have more time to react with char, thereby increasing the syngas yield and LHV of the product stream.

84

- Placing the OC near the inlet and using an OC/biomass ratio of 0.25 and a steam/biomass ratio of one resulted in the highest gasification efficiency for biomass-fueled CLG.

- Biomass-fueled CLC in a PBR produced an outlet gas consisting of 75.2% CO_2 (dry, inert-free), which would be adequately pure CO_2 for effective carbon capture using CLC.

- Using a reactor fully packed with OC and using steam as the carrier gas for the system resulted in an outlet stream with a CO_2 and H_2O composition of 95%, which is an improvement of an order of magnitude compared to experimental data for packed bed CLC.

- If a limited amount of OC is available for biomass-fueled CLC, it should be located near the outlet to maximize the CO_2 fraction in the product stream.

- The model can simulate the dynamic profiles of biomass-fueled CLC and evaluate the most effective time to end the reduction stage, significantly improving the outlet gas composition and the overall economics of this system.

5.2 Recommendations for Future Work

The work presented in this thesis can be extended to determine additional design and control strategies to further improve the feasibility of chemical-looping technology. Recommendations for future work in this area which can be pursued are:

- Assess the observability and implement a suitable state estimation framework for the NMPC of packed bed CLC to enable control with a realistic set of measured states for this process.

- Develop optimal scheduling and control frameworks [104] such that multiple reactors undergo the heat recovery phase at the same time, increasing the outlet flowrate of hot air which is sent to the turbine to generate energy.

- Investigate the use of more compact reactors through simultaneous optimization of design and control of this process to account for the interactions and compromises between the system design and control to further improve the effectiveness of carbon capture [105].

- Further validate the biomass-fueled CL reactor network model using experimental data from packed bed (as opposed to fluidized bed) biomass-fueled CLC.

- Extend the biomass-fueled CL reactor network model to industrial-scale reactors to facilitate the implementation of biomass-fueled chemical-looping technologies in gasification and combustion processes.

- Implement NMPC for packed bed biomass-fueled CL to determine control strategies which can improve the performance of these processes.

- Implement economic model predictive control or real-time optimization to further improve the performance and economic feasibility of CL processes [106].

- Investigate CLC reactor designs using different OCs stacked within the reactor to take advantage of their different properties (e.g., use copper-based OCs near the reactor inlet to take advantage of their high reactivity, with nickel-based OCs at the reactor outlet because of their good stability at high temperatures).

- Investigate the potential of machine learning to improve the online operation of these systems (e.g., develop neural network models to decrease the computational time required to solve these systems) [107] [108].

References

[1] IEA, "Key World Energy Statistics," IEA, 2021. [Online]. Available: https://www.iea.org/reports/key-world-energy-statistics-2021/supply.

[2] IPCC, Climate Change 2007: Mitigation, Contribution of Working Group III to the Fourth Assessment Report of the Intergovernmental Panel on Climate Change, B. Metz, O. R. Davidson, P. R. Bosch, R. Dave and L. A. Meyer, Eds., Cambridge, UK: Cambridge University Press, 2007.

[3] M. Ishida and H. Jin, "A Novel Chemical-Looping Combustor without NOx Formation," *Industrial & Engineering Chemistry Research,* vol. 35, pp. 2469-2472, 1996.

[4] M. Ishida, D. Zheng and T. Akehata, "Evaluation of a chemical-looping-combustion power-generation system by graphic exergy analysis," *Energy,* vol. 12, no. 2, pp. 147-154, 1987.

[5] S. Noorman, F. Gallucci, M. van Sint Annaland and J. Kuipers, "A theoretical investigation of CLC in packed beds. Part 1: Particle model," *Chemical Engineering Journal,* vol. 167, pp. 297-307, 2011.

[6] L. Han, Z. Zhou and G. M. Bollas, "Heterogeneous modeling of chemical-looping combustion. Part 1: Reactor Model," *Chemical Engineering Science,* vol. 104, pp. 233-249, 2013.

[7] L. Han, Z. Zhou and G. M. Bollas, "Heterogeneous modeling of chemical-looping combustion. Part 2: Particle model," *Chemical Engineering Science,* vol. 113, pp. 116-128, 2014.

[8] G. Diglio, P. Bareschino, E. Mancusi and F. Pepe, "Techno-Economic Evaluation of a Small-Scale Power Generation Unit Based on a Chemical Looping Combustion Process in Fixed Bed Reactor Network," *Industrial & Engineering Chemistry Research,* vol. 57, pp. 11299-11311, 2018.

[9] V. Spallina, P. Chiesa, E. Martelli, F. Gallucci, M. Romano, G. Lozza and M. van Sint Annaland, "Reactor design and operation strategies for a large-scale packed-bed CLC power plant with coal syngas," *International Journal of Greenhouse Gas Control,* vol. 36, pp. 34-50, 2015.

[10] S. Noorman, M. van Sint Annaland and H. Kuipers, "Packed Bed Reactor Technology for Chemical-Looping Combustion," *Industrial & Engineering Chemistry Research,* vol. 46, pp. 4212-4220, 2007.

[11] J. Fernández and J. Abanades, "Conceptual design of a Ni-based chemical looping combustion process using fixed-beds," *Applied Energy,* vol. 135, pp. 309-319, 2014.

[12] F. Albalawi, H. Durand and P. D. Christofides, "Process operational safety via model predictive control: Recent results and future research directions," *Computers & Chemical engineering,* vol. 114, no. 9, pp. 171-190, 2018.

[13] J. Kemper, "Biomass and carbon dioxide capture and storage: A review," *International Journal of Greenhouse Gas Control,* vol. 40, pp. 401-430, 2015.

[14] P. McKendry, "Energy production from biomass (part 1): overview of biomass," *Bioresource Technology,* vol. 83, no. 1, pp. 37-46, 2002.

[15] J. Adánez, A. Abad, F. García-Labiano, P. Gayán and L. F. de Diego, "Progress in Chemical-Looping Combustion and Reforming technologies," *Progress in Energy and Combustion Science,* vol. 38, pp. 215-282, 2012.

[16] T. Mendiara, A. Pérez-Astray, M. Izquierdo, A. Abad, L. de Diego, F. García-Labiano, P. Gayán and J. Adánez, "Chemical Looping Combustion of different types of biomass in a 0.5 kWth unit," *Fuel,* vol. 211, pp. 868-875, 2018.

[17] Z. Huang, F. He, Y. Feng, K. Zhao, A. Zheng, S. Chang and H. Li, "Synthesis gas production through biomass direct chemical looping conversion with natural hematite as an oxygen carrier," *Bioresource Technology,* vol. 140, pp. 138-145, 2013.

[18] Q. Liu, C. Hu, B. Peng, C. Liu, Z. Li, K. Wu, H. Zhang and R. Xiao, "High H2/CO ratio syngas production from chemical looping co-gasification of biomass and polyethylene with CaO/Fe2O3 oxygen carrier," *Energy Conversion and Management,* vol. 199, no. 111951, 2019.

[19] J. Gibbins and H. Chalmers, "Carbon capture and storage," *Energy Policy,* vol. 36, pp. 4317-4322, 2008.

[20] H. J. Liu, P. Were, Q. Li, Y. Gou and Z. Hou, "Worldwide Status of CCUS Technologies and Their Development and Challenges in China," *Geofluids,* vol. 2017, no. 6126505, 2017.

[21] T. Wilberforce, A. Baroutaji, B. Soudan, A. H. Al-Alami and A. G. Olabi, "Outlook of carbon capture technology and challenges," *Science of the Total Environment,* vol. 657, pp. 56-72, 2019.

[22] H. Ge, W. Guo, L. Shen, T. Song and J. Xiao, "Experimental investigation on biomass gasification using chemical looping in a batch reactor and a continuous dual reactor," *Chemical Engineering Journal,* vol. 286, pp. 689-700, 2016.

[23] O. Brandvoll and O. Bolland, "Inherent CO2 Capture Using Chemical Looping Combustion in a Natural Gas Fired Power Cycle," *Journal of Engineering for Gas Turbines and Power,* vol. 126, no. 2, pp. 316-321, 2004.

[24] M. Ishida, M. Yamamoto and T. Ohba, "Experimental results of chemical-looping combustion with NiO/NiAl2O4 particle circulation at 1200 C," *Energy Conversion and Management,* vol. 43, pp. 1469-1478, 2002.

[25] A. Lyngfelt, B. Kronberger, J. Adánez, J.-X. Morin and P. Hurst, "The Grace Project. Development of oxygen carrier particles for chemical-looping combustion, design and operation of a 10 kW chemical-looping combustor.," in *International Conference of Greenhouse Gas Control Technology (GHGT-7)*, Vancouver, 2004.

[26] S. Noorman, M. van Sint Annaland and J. Kuipers, "Experimental validation of packed bed chemical-looping combustion," *Chemical Engineering Science,* vol. 65, no. 1, pp. 92-97, 2010.

[27] H. Jin and M. Ishida, "Reactivity Study on Natural-Gas-Fueled Chemical-Looping Combustion by a Fixed-Bed Reactor," *Industrial & Engineering Chemistry Research,* vol. 41, pp. 4004-4007, 2002.

[28] H. Hamers, F. Gallucci, G. Williams and M. van Sint Annaland, "Experimental demonstration of CLC and the pressure effect in packed bed reactors using NiO/CaAl2O4 as oxygen carrier," *Fuel,* vol. 159, pp. 828-836, 2015.

[29] V. Spallina, B. Marinello, F. Gallucci, M. Romano and M. Van Sint Annaland, "Chemical looping reforming in packed-bed reactors: Modelling, experimental validation and large-scale reactor design," *Fuel Processing Technology,* vol. 156, pp. 156-170, 2017.

[30] L. Han and G. M. Bollas, "Dynamic optimization of fixed bed chemical-looping combustion processes," *Energy,* vol. 112, pp. 1107-1119, 2016.

[31] C. Chen and G. M. Bollas, "Design and Scheduling of Semibatch Chemical-Looping Reactors," *Industrial & Engineering Chemistry Research,* vol. 59, pp. 6994-7006, 2020.

[32] Y. Cao, B. Casenas and W.-P. Pan, "Investigation of Chemical Looping Combustion by Solid Fuels. 2. Redox Reaction Kinetics and Product Characterization with Coal, Biomass, and Solid Waste as Solid Fuels and CuO as an Oxygen Carrier," *Energy & Fuels,* vol. 20, no. 5, pp. 1845-1854, 2006.

[33] L. Fan, F. Li and S. Ramkumar, "Utilization of chemical looping strategy in coal gasification processes," *Particuology,* vol. 6, no. 3, pp. 131-142, 2008.

[34] N. M. Nguyen, F. Alobaid and B. Epple, "Chemical looping gasification of torrefied woodchips in a bubbling fluidized bed test rig using iron-based oxygen carriers," *Renewable Energy,* vol. 172, pp. 34-45, 2021.

[35] S. Noorman, F. Gallucci, M. van Sint Annaland and J. Kuipers, "A theoretical investigation of CLC in packed beds. Part 2: Reactor model," *Chemical Engineering Journal,* vol. 167, pp. 369-376, 2011.

[36] A. Nandy, C. Loha, S. Gu, P. Sarkar, M. K. Karmakar and P. K. Chatterjee, "Present status and overview of Chemical Looping Combustion technology," *Renewable and Sustainable Energy Reviews,* vol. 59, pp. 597-619, 2016.

[37] X. Cheng, K. Li, X. Zhu, Y. Wei, Z. Li, Y. Long, M. Zheng, D. Tian and H. Wang, "Enhanced performance of chemical looping combustion of methane by combining oxygen carriers via optimizing the stacking sequences," *Applied Energy,* vol. 230, pp. 696-711, 2018.

[38] N. Berguerand and A. Lyngfelt, "Design and operation of a 10 kWth chemical-looping combustor for solid fuels - Testing with South African coal," *Fuel,* vol. 87, no. 12, pp. 3713-2726, 2008.

[39] A. Cuadrat, A. Abad, G.-L. F., P. Gayán, L. de Diego and J. Adánez, "The use of ilmenite as oxygen-carrier in a 500 Wth Chemical-Looping Coal Combustion unit," *International Journal of Greenhouse Gas Control,* vol. 5, no. 6, pp. 1630-1642, 2011.

[40] B. Al-Qadri, X. Wang and D. Chen, "Experimental Study on Chemical Looping Co-gasification of Alfalfa and Polyethylene with Iron Ore as the Oxygen Carrier for High H2/CO Production," *Energy & Fuels,* vol. 36, pp. 6939-6948, 2022.

[41] M. D. Kevat and T. Banerjee, "Process Simulation and Energy Analysis of Chemical Looping Combustion and Chemical Looping with Oxygen Uncoupling for Sawdust Biomass," *Energy Technology,* vol. 6, pp. 1237-1247, 2018.

[42] L. Zhou, K. Deshpande, X. Zhang and R. K. Agarwal, "Process simulation of Chemical Looping Combustion using ASPEN plus for a mixture of biomass and coal with various oxygen carriers," *Energy,* vol. 195, no. 116955, 2020.

[43] P. Ohlemüller, F. Alobaid, A. Gunnarsson, J. Ströhle and B. Epple, "Development of a process model for coal chemical looping combustion and validation against 100 kWth tests," *Applied Energy,* vol. 157, pp. 433-448, 2015.

[44] S. G. Gopaul, A. Dutta and R. Clemmer, "Chemical looping gasification for hydrogen production: A comparison of two unique processes simulated using ASPEN Plus," *International Journal of Hydrogen Energy,* vol. 39, pp. 5804-5817, 2014.

[45] Z. Li, H. Xu, W. Yang, A. Zhou and M. Xu, "CFD simulation of a fluidized bed reactor for biomass chemical looping gasification with continuous feedstock," *Energy Conversion and Management,* vol. 201, no. 112143, 2019.

[46] W. Du, L. Ma, Q. Pan, Q. Dai, M. Zhang, X. Yin, X. Xiong and W. Zhang, "Full-loop CFD simulation of lignite Chemical Looping Gasification with phosphogypsum as oxygen carrier using a circulating fluidized bed," *Energy,* vol. 262A, no. 125451, 2023.

[47] W. Yin, S. Wang, K. Zhang and Y. He, "Numerical investigation of in situ gasification chemical looping combustion of biomass in a fluidized bed reactor," *Renewable Energy,* vol. 151, pp. 216-225, 2020.

[48] R. Dong, S. Yang, J. Hu, F. Chen, G. Bao and H. Wang, "CFD investigation of the in-situ gasification process of biomass in the chemical looping combustion system," *Renewable Energy,* vol. 185, pp. 1245-1260, 2022.

[49] Z. Li, H. Xu, W. Yang, M. Xu and F. Zhao, "Numerical investigation and thermodynamic analysis of syngas production through chemical looping gasification using biomass as fuel," *Fuel,* vol. 246, pp. 466-475, 2019.

[50] R. Porrazzo, G. White and R. Ocone, "Aspen Plus simulations of fluidised beds for chemical looping combustion," *Fuel,* vol. 136, pp. 46-56, 2014.

[51] J. Lin, L. Sun, K. Luo, D. Kong and J. Fan, "Three-dimensional simulation of a gas-fueled chemical looping combustion system with dual circulating fluidized bed reactors," *Energy,* vol. 246, no. 123293, 2022.

[52] R.-Y. Chein, W.-F. Tseng and K.-T. Wu, "Numerical simulation of fuel reactor for a methane-fueled chemical looping combustion using bubbling fluidized bed with internal particle circulation," *International Journal of Hydrogen Energy,* vol. 47, no. 88, pp. 37415-37428, 2022.

[53] C. Fan, Z. Cui, J. Wang, Z. Liu and W. Tian, "Exergy analysis and dynamic control of chemical looping combustion for power generation system," *Energy Conversion and Management,* vol. 228, no. 113728, 2021.

[54] T. Wanotayaroj, B. Chalermsinsuwan and P. Piumsomboon, "Dynamic simulation and control system for chemical looping combustion," *Energy Reports,* vol. 6, pp. 32-39, 2020.

[55] V. Spallina, M. C. Romano, P. Chiesa, F. Gallucci, M. van Sint Annaland and G. Lozza, "Integration of coal gasification and packed bed CLC for high efficiency and near-zero emission power generation," *International Journal of Greenhouse Gas Control,* vol. 27, pp. 28-41, 2014.

[56] M. Lucio and L. A. Ricardez-Sandoval, "Dynamic modelling and optimal control strategies for chemical-looping combustion," *Fuel,* vol. 262, no. 116544, 2020.

[57] K. Toffolo and L. Ricardez-Sandoval, "Optimal Design and Control of a Multiscale Model for a Packed Bed Chemical-Looping Combustion Reactor," *IFAC PapersOnLine,* vol. 54, no. 3, pp. 615-620, 2021.

[58] R. B. Parker and L. T. Biegler, "Dynamic Modelling and Nonlinear Model Predictive Control of a Moving Bed Chemical Looping Combustion Reactor," *IFAC PapersOnLine,* vol. 55, no. 7, pp. 400-405, 2022.

[59] L. A. Ricardez-Sandoval, "Current Challenges in the Design and Control of Multiscale Systems," *The Canadian Journal of Chemical Engineering,* vol. 89, pp. 1324-1341, 2011.

[60] R. G. Rice and D. D. Do, "Solution Techniques for Models Yielding Ordinary Differential Equations (ODE)," in *Applied Mathematics and Modeling for Chemical Engineers*, Toronto, John Wiley & Sons, Inc, 1995, pp. 37-103.

[61] Y. Yuan, X. Dong and L. Ricardez-Sandoval, "A multi-scale model for syngas combustion on NiO oxygen carrier for chemical looping combustion: the role of nearest neighbours," *Fuel Processing Technology,* vol. 229, no. 107172, 2022.

[62] M. M. Hossain and H. I. de Lasa, "Chemical-looping combustion (CLC) for inherent CO2 separations - a review," *Chemical Engineering Science,* vol. 63, no. 18, pp. 4433-4451, 2008.

[63] I. Iliuta, R. Tahoces, G. S. Patience, S. Rifflard and F. Luck, "Chemical-Looping Combustion Process: Kinetics and Mathematical Modeling," *American Institute of Chemical Engineers Journal,* vol. 56, no. 4, pp. 1063-1079, 2010.

[64] Z. Zhou, L. Han and G. M. Bollas, "Kinetics of NiO reduction by H2 and Ni oxidation at conditions relevant to chemical-looping combustion and reforming," *International Journal of Hydrogen Energy,* vol. 39, pp. 8535-8556, 2014.

[65] O. Nordness, L. Han, Z. Zhou and G. M. Bollas, "High-Pressure Chemical-Looping of Methane and Synthesis Gas with Ni and Cu Oxygen Carriers," *Energy & Fuels,* vol. 30, pp. 504-514, 2016.

[66] L. Han, Z. Zhou and G. M. Bollas, "Model-Based Analysis of Chemical-Looping Combustion Experiments. Part I: Structural Identifiability of Kinetic Models for NiO Reduction," *American Institute of Chemical Engineers Journal,* vol. 62, no. 7, pp. 2419-2431, 2016.

[67] L. Han, Z. Zhou and G. M. Bollas, "Model-Based Analysis of Chemical-Looping Combustion Experiments. Part II: Optimal Design of CH4-NiO Reduction Experiments," *American Institude of Chemical Engineers Journal,* vol. 62, no. 7, pp. 2432-2446, 2016.

[68] T. Numaguchi and K. Kikuchi, "Intrinsic kinetics and design simulation in a complex reaction network; steam-methane reforming," *Chemical Engineering Science,* vol. 43, no. 8, pp. 2295-2301, 1988.

[69] W. E. Hart, J.-P. Watson and D. L. Woodruff, "Pyomo: modeling and solving mathematical programs in Python," *Mathematical Programming Computation,* vol. 3, no. 219, 2011.

[70] A. Wächter and L. T. Biegler, "On the implementation of an interior-point filter line-search algorithm for large-scale nonlinear programming," *Mathematical Programming,* Vols. 1-6, pp. 25-57, 2006.

[71] M. Okada, K. Yoneda, S. Morii, T. Suzuki and K. Seki, "On-line Monitoring Equipments of Dioxins and their Precursors for Incineration Plants," *Mitsubishi Heavy Industries Technical Review,* vol. 40, no. 5, 2003.

[72] C. Muller, I. Craig and N. Ricker, "Modelling, validation, and control of an industrial fuel gas blending system," *Journal of Process Control,* vol. 21, no. 6, pp. 852-860, 2011.

[73] T. K. Ibrahim, M. M. Rahman, O. M. Ali, F. Basrawi and R. Mamat, "Optimum Performance Enhancing Strategies of the Gas Turbine Based on the Effective Temperatures," *MATEC Web of Conferences,* vol. 38, no. 01002, 2016.

[74] R. Daroughegi, F. Meshkani and M. Rezaei, "Enhanced activity of CO2 methanation over mesoporous nanocrystalline Ni-Al2O3 catalysts prepared by ultrasound-assisted co-precipitation method," *International Journal of Hydrogen Energy,* vol. 42, no. 22, pp. 15115-15125, 2017.

[75] A. Umar and J. T. Irvine, "Gasification of Glycerol Over Ni//γ-Al2O3 For Hydrogen Production: Tailoring Catalytic Properties to Control Deactivation," *Catalysis for Sustainable Energy,* vol. 7, pp. 65-74, 2020.

[76] Z. Amrollahi, P. A. M. Ystad, I. S. Ertesvåg and O. Bolland, "Optimized process configurations of post-combustion CO2 capture for natural-gas-fired power plant - Power plant efficiency analysis," *International Journal of Greenhouse Gas Control,* vol. 8, pp. 1-11, 2012.

[77] C. L. Proctor, "Internal Combustion Engines," in *Encyclopedia of Physical Science and Technology (Third Edition)*, Academic Press, 2003, pp. 33-44.

[78] J. H. Kim, T. W. Song, T. S. Kim and S. T. Ro, "Model Development and Simulation of Transient Behavior of Heavy Duty Gas Turbines," *Journal of Engineering for Gas Turbines and Power,* vol. 123, no. 3, pp. 589-594, 2000.

[79] Y. K. Salkuyeh and T. A. I. Adams, "Integrated petroleum coke and natural gas polygeneration process with zero carbon emissions," *Energy,* vol. 91, pp. 479-490, 2015.

[80] A. R. Sefiddashti, R. Shirmohammadi and F. Petrakopoulou, "Efficiency Enhancement of Gas Turbine Systems with Air Injection Driven by Natural Gas Turboexpanders," *Sustainability,* vol. 13, no. 10994, 2021.

[81] Y. Guan, Y. Liu, B. Wang, Y. Feng and Q. Lyu, "Reaction characteristics and lattice oxygen transformation mechanism of semi-coke chemical looping gasification with Fe2O3/CaSO4-Al2O3 oxygen carrier," *Journal of Cleaner Production,* vol. 369, no. 133291, 2022.

[82] X. Li, A. Lyngfelt and T. Mattisson, "An experimental study of a volatiles distributor for solid fuels chemical-looping combustion process," *Fuel Processing Technology,* vol. 220, no. 106898, 2021.

[83] S. Xue and X. Wang, "Process simulation of chemical looping gasification of biomass using Fe-based oxygen carrier: Effect of coupled parameters," *Journal of Cleaner Production,* vol. 356, no. 131839, 2022.

[84] B. Das, A. Bhattacharya and A. Datta, "Kinetic modeling of biomass gasification and tar formation in a fluidized bed gasifier using an equivalent reactor network (ERN)," *Fuel,* vol. 280, no. 118582, 2020.

[85] J. Darido, A. Dhahak, R. Bounaceur, C. Le Dreff-Lorimier, G. Leyssens, F. Cazier, P. Genevray and F. Battin-Leclerc, "Emissions from a Domestic Wood Heating Appliance: Experimental Measurements and Numerical Study Using an Equivalent Reactor Network (ERN) Approach Coupled with a Detailed Chemical Mechanism," *Energy & Fuels,* vol. 35, pp. 18680-18698, 2021.

[86] S. Gerber, F. Behrendt and M. Oevermann, "An Eulerian modeling approach of wood gasification in a bubbling fluidized bed reactor using char as bed material," *Fuel,* vol. 89, no. 10, pp. 2903-2917, 2010.

[87] M. L. Boroson, J. B. Howard, J. P. Longwell and W. A. Peters, "Product Yields and Kinetics from the Vapor Phase Cracking of Wood Pyrolysis Tars," *AIChE Journal,* vol. 35, no. 1, pp. 120-128, 1989.

[88] F. Bustamante, R. M. Enick, A. V. Cugini, R. P. Killmeyer, B. H. Howard, K. S. Rothenberger, M. V. Ciocco, B. D. Morreale, S. Chattopadhyay and S. Shi, "High-Temperature Kinetics of the Homogeneous Reverse Water-Gas Shift Reaction," *AIChE Journal,* vol. 50, no. 5, pp. 1028-1041, 2004.

[89] W. P. Jones and R. P. Lindstedt, "Global Reaction Schemes for Hydrocarbon Combustion," *Combustion and Flame,* Vols. 233-249, p. 73, 1988.

[90] R. C. Everson, H. W. Neomagus, H. Kasaini and D. Njapha, "Reaction kinetics of pulverized coal-chars derived from inertinite-rich coal discards: Gasification with carbon dioxide and steam," *Fuel,* vol. 85, pp. 1076-1082, 2006.

[91] T. Mattisson, J. Abanades, A. Lyngfelt, A. Johansson, J. Adánez, F. García-Labiano, L. de Diego, P. Gayán, B. Kronberger, H. Hofbauer, M. Luisser, J. Palacios, D. Alvares, M. Orjala and V. Heiskanen, "Capture of CO2 in Coal Combustion ECSC Coal RTD Programme Final Report," ECSC-7220-PR125, 2005.

[92] T. Mattisson, A. Lyngfelt and P. Cho, "The use of iron oxide as an oxygen carrier in chemical-looping combustion of methane with inherent separation of CO2," *Fuel,* vol. 80, pp. 1953-1962, 2001.

[93] K. Mahalatkar, J. Kuhlman, E. D. Huckaby and T. O'Brien, "CFD simulation of a chemical-looping fuel reactor using solid fuel," *Chemical Engineering Science,* vol. 66, pp. 3617-3627, 2011.

[94] K. Mahalatkar, J. Kuhlman, E. D. Huckaby and T. O'Brien, "Computational fluid dynamics simulations of chemical looping fuel reactors using gaseous fuels," *Chemical Engineering Science,* vol. 66, pp. 469-479, 2011.

[95] E. Lorente, Q. Cai, J. Peña, J. Herguido and N. Brandon, "Conceptual design and modelling of the steam-iron process and fuel cell integrated system," *International Journal of Hydrogen Energy,* vol. 42, pp. 13607-13616, 2017.

[96] E. Hairer and G. Wanner, "Implementation of Implicit Runge-Kutta Methods," in *Solving Ordinary Differential Equations II: Stiff and Differential-Algebraic Problems*, Heidelberg, Springer Berlin, 1996, pp. 118-130.

[97] D. M. Y. Maya, E. E. S. Lora, R. V. Andrade, A. Ratner and J. D. M. Angel, "Biomass gasification using mixtures of air, saturated steam, and oxygen in a two-stage downdraft gasifier. Assessment using a CFD modeling approach," *Renewable Energy,* vol. 177, pp. 1014-1030, 2021.

[98] M. A. Uddin, H. Tsuda, S. Wu and E. Sasaoka, "Catalytic decomposition of biomass tars with iron oxide catalysts," *Fuel,* vol. 87, pp. 451-459, 2008.

[99] A. Nzihou, B. Stanmore and P. Sharrock, "A review of catalysts for the gasification of biomass char, with some reference to coal," *Energy,* vol. 58, pp. 305-317, 2013.

[100] D. Kunii and O. Levenspiel, Fluidization Engineering, Boston: Butterworth-Heinemann, 1991.

[101] S. Maroufi, B. Khoshandam and R. V. Kumar, "Comparison between fluidised bed and packed bed reactors: non-catalytic gas-solid reactions," *Ironmaking and Steelmaking,* vol. 39, no. 4, pp. 301-311, 2012.

[102] B. Hou, H. Zhang, H. Li and Q. Zhu, "Study on Kinetics of Iron Oxide Reduction by Hydrogen," *Chinese Journal of Chemical Engineering,* vol. 20, no. 1, pp. 10-17, 2012.

[103] E. R. Monazam, R. W. Breault and R. Siriwardane, "Kinetics of Hematite to Wüstite by Hydrogen for Chemical Looping," *Energy & Fuels,* vol. 28, pp. 5406-5414, 2014.

[104] O. Andrés-Martínez and L. A. Ricardez-Sandoval, "Integration of planning, scheduling, and control: A review and new perspectives," *The Canadian Journal of Chemical Engineering,* vol. 100, no. 9, pp. 2057-2070, 2022.

[105] M. Rafiei and L. A. Ricardez-Sandoval, "New frontiers, challenges, and opportunities in integration of design and control for enterprise-wide sustainability," *Computers and Chemical Engineering,* vol. 132, no. 106610, 2020.

[106] G. D. Patrón and L. Ricardez-Sandoval, "An integrated real-time optimization, control, and estimation scheme for post-combustion CO2 capture," *Applied Energy,* vol. 308, no. 118302, 2022.

[107] D. Rangel-Martinez, K. Nigam and L. A. Ricardez-Sandoval, "Machine learning on sustainable energy: A review and outlook on renewable energy systems, catalysis, smart grid and energy storage," *Chemical Engineering Research and Design,* vol. 174, pp. 414-441, 2021.

[108] Y. Zhang, H. Wang, W. Chen, J. Zeng, L. Zhang, H. Wang and W. E, "DP-GEN: A concurrent learning platform for the generation of reliable deep learning based potential energy models," *Computer Physics Communications,* vol. 253, no. 107206, 2020.

[109] A. Abad, J. Adánez, F. García-Labiano, L. F. de Diego, P. Gayán and J. Celaya, "Mapping the range of operational conditions for Cu-, Fe-, and Ni-based oxygen carriers in chemical-looping combustion," *Chemical Engineering Science,* vol. 62, pp. 533-549, 2007.

[110] F. García-Labiano, L. De Diego, J. Adánez, A. Abad and P. Gayán, "Temperature variations in the oxygen carrier particles during their reduction and oxidation in a chemical-looping combustion system," *Chemical Engineering Science,* vol. 60, pp. 851-862, 2005.

[111] C. Satterfield, Mass transfer in heterogeneous catalysis, Cambridge: Massachusetts Institute of Technology Press, 1981.

[112] T. Marrero and E. Mason, "Gaseous diffusion constants," *Journal of Physical and Chemical Reference Data,* vol. 1, pp. 1-118, 1972.

[113] K. B. Bischoff and O. Levenspiel, "Fluid dispersion - generalization and comparison of mathematical models - II Comparison of models," *Chemical Engineering Science,* vol. 17, pp. 257-264, 1962.

[114] S. Yagi, D. Kunii and N. Wakao, "Studies on Axial Effective Thermal Conductivities in Packed Beds," *AIChE Journal,* vol. 6, no. 4, pp. 543-546, 1960.

Appendix A – Mass and Heat Transfer Correlations and Parameters

The kinetic parameters from these respective sources are listed in Table A.1 to Table A.5, where the rate constant k is calculated using the Arrhenius equation, as per Equation A.1, and the equilibrium coefficients K_j are calculated from Equation A.2, and the adsorption coefficients $K_{k,i}$ are obtained using Equation A.3. Equation A.4 presents an additional correlation used to calculate the kinetic rate coefficient in the OC reactions R4.7-R4.13.

$$k_j = k_{0,j} \exp\left(-\frac{E_{a,j}}{R_g T}\right) \tag{A.1}$$

$$K_j = K_{0,j} \exp\left(-\frac{\Delta H_j}{R_g T}\right) \tag{A.2}$$

$$K_{j,i} = K_{0,j,i} \exp\left(-\frac{\Delta H_{j,i}}{R_g T}\right) \tag{A.3}$$

$$k_j = \frac{3 b_j k_{0,j} \exp\left(-\frac{E_{a,j}}{R_g T}\right)}{\rho_m r_0} \tag{A.4}$$

Table A.1. Adsorption coefficients and miscellaneous parameters for the reaction kinetics in the nickel-based CLC system.

Parameter	Value
a_0 [m²/g OC]	102
n	0.65
$K_{0,7,CO}$ [bar^{-1}]	8.23×10^{-5}
$\Delta H_{7,CO}$ [kJ/mol]	-70.6
$K_{0,7,H2}$ [bar^{-1}]	6.12×10^{-9}
$\Delta H_{7,H2}$ [kJ/mol]	-82.9
$K_{0,7,CH4}$ [bar^{-1}]	6.65×10^{-4}

$\Delta H_{7,CH4}$ [kJ/mol]	-38.3
$K_{0,7,H2O}$ [bar^{-1}]	1.77×10^5
$\Delta H_{7,H2O}$ [kJ/mol]	88.7

Table A.2. Reaction rate coefficients, activation energies, and equilibrium constants for the reactions in CLC with a nickel-based oxide.

Reaction	$k_{0,j}$ [s^{-1}]	$E_{a,j}$ [kJ/mol]	K_j	ΔH_j [kJ/mol]	Source
R3.1	1.38×10^{-3}	22	-	-468	[64] [65]
R3.2	4.66	77.4	-	52.76	[63]
R3.3	2.32×10^{-4}	39	-	156.5	[66] [67]
R3.4	1.31×10^{-4}	26.4	-	-2.1	[63]
R3.5	4.22×10^{-4}	37	-	-43.3	[66] [67]
R3.6	3.65×10^2	42.8	1.2×10^{13}	268	[68] [29]
R3.7	7.25×10^1	102	1.77×10^{-2}	-36.6	[65]

Table A.3. Heats of reaction, Arrhenius pre-exponential factors, and activation energies for the reactions in biomass-fueled chemical-looping.

Reaction	ΔH_j [kJ/mol]	$k_{0,j}$ [s^{-1}]	$E_{a,j}$ [kJ/mol]	Source
R4.1	1.1×10^3 kJ/kg	4.13×10^6	112.7	Li [45]
R4.2	-	9.55×10^4	123.3	Li [45]
R4.3	-41	2.17×10^7	192.9	Bustamante [88]

R4.4	206	3.00×10^5	125	Jones & Lindstedt [89]
R4.7, R4.8	141	Table A.4	Table A.4	Mattisson [91] [92], Yin [47], Abad [109]
R4.9- R4.11	-5.8	Table A.4	Table A.4	Mattisson [91] [92], Mahalatkar [93] [94]
R4.12, R4.13	-47	Table A.4	Table A.4	Mattisson [91] [92], Mahalatkar [93] [94]
R4.14	-	1.75	18.7	Lorente [95]

Table A.4. Additional reaction rate parameters for OC reactions R4.7-R4.13 with an iron-based oxygen carrier.

Reaction	k_0 [mol^{1-n}m^{3n-2}/s]	$E_{a,j}$ [kJ/mol]	b_j	n_j
CH_4 (R4.7)	8.0×10^{-4}	49	12	1.3
C_2H_4 (R4.8)	8.0×10^{-4}	49	12	1.3
CO (R4.9)	6.2×10^{-4}	20	3	1
CO (R4.10)	6.2×10^{-4}	20	1	1
CO (R4.11)	6.2×10^{-4}	20	1	1
H_2 (R4.12)	2.3×10^{-3}	24	3	0.8
H_2 (R4.13)	2.3×10^{-3}	24	1	0.8

Table A.5. Additional reaction rate parameters for iron-based OC reactions R4.7-R4.14 and char reactions R4.5-R4.6.

	Parameter	Value	Source
OC Reactions	r_0 [1/m]	2.6×10^{-7}	Mattisson [91] [92], Mahalatkar [93] [94]
	ρ_m [mol/m^3]	32811	
	$Y_{CH4,TGA}$	0.1	
	R_0	0.3	
Char (General)	ρ_c [kg/m^3]	1940	Everson [90]
	$S_0/(1-\varepsilon_0)$ [m^2/m^3]	8.83×10^4	
Char (Boudouard)	k_5 [1/s] (1173 K)	2.00×10^{-9}	
	$E_{a,5}$ [kJ/mol]	137	
	$K_{5,CO}$ [Pa^{-1}] (1173 K)	2.6×10^{-4}	
	$K_{5,CO}$ [Pa^{-1}] (1273 K)	1.4×10^{-4}	
	$K_{5,CO2}$ [Pa^{-1}] (1173 K)	1.98×10^{-5}	
	$\Delta H_{5,CO2}$ [kJ/mol]	41	
Char (Gasification)	k_6 [1/s] (1173 K)	7.97×10^{-9}	
	$E_{a,6}$ [kJ/mol]	212	
	$K_{6,H2}$ [Pa^{-1}] (1173 K)	9.36	
	$K_{6,H2}$ [Pa^{-1}] (1273 K)	4.07	
	$K_{6,H2O}$ [Pa^{-1}] (1173 K)	8.07×10^{-5}	
	$\Delta H_{6,H2O}$ [kJ/mol]	69	
Iron-Steam	N_{14}	0.39	Lorente [95]

	n_{14}	0.17	

The parameters for the industrial-scale reactor packed with a nickel-based OC are presented in Table A.6. For the oxidation stage, the parameters represent air at 900 °C and 20 bar, and for the reduction stage, they are taken for methane at 450 °C and 20 bar.

Table A.6. Heat and mass transfer parameters for the oxidation and reduction stages in packed bed CLC with a nickel-based oxide.

Parameter	Oxidation	Reduction	Source
C_{pf} [J/mol/K]	33.87	58.55	[56]
C_{ps} [J/kg/K]	1250	1250	[110]
d_{pore} [m]	1×10^{-8}	1×10^{-8}	[56]
ε_b	0.37	0.37	[63]
λ_{e0} [W/m/K]	0.01	0.01	[6]
λ_i [W/m/K]	Ni: 75 Al_2O_3: 7	NiO: 13 Al_2O_3: 7	[110]
μ [Pa·s]	3.90×10^{-5}	4.02×10^{-5}	[56]
ρ [kg/m^3]	6.50	4.54	[56]
ρ_s [kg/m^3]	3470	3470	[110]
τ_p	3.0	3.0	[6]
d_{ij} [m^2/s]	3.128×10^{-5}	(See Table A.9)	

The general parameters for the biomass-fueled reactor model are presented in Table A.7.

Table A.7. General parameters for the reduction stage of biomass-fueled chemical-looping.

Parameter	Value	Source
C_{pf} [J/mol/K]	58.55	[56]
C_{ps} [J/kg/K]	883.1	[6]
d_{pore} [m]	1.0×10^{-8}	[56]
ε_b	0.37	[56]
λ_{e0} [W/m/K]	0.01	[6]
λ_i [W/m/K]	Fe_2O_3: 5 SiO_2: 2	[6]
μ [Pa·s]	4.02×10^{-5}	[6]
ρ [kg/m^3]	0.311	[56]
ρ_s [kg/m^3]	3257	[91]
τ_p	3.0	[6]
h_w [W/m^2/K]	90	[28]
d_{ij} [m^2/s]	(see Table A.9)	

The proximate and ultimate analyses of the biomass fuels used in the experiments performed by Liu et al. [18] and Huang et al. [17] are presented in Table A.8.

Table A.8. Proximate and ultimate analyses of the biomass fuel used by Liu et al. and Huang et al.

	Proximate Analysis (wt%, dry basis)			Ultimate Analysis (wt%, dry basis)				
	Volatile Matter	Fixed Carbon	Ash	C	H	O	N	S
Liu [18] **(CLG)**	84.02	15.03	0.95	49.51	06.28	42.90	0.00	0.36
Huang [17] **(CLC)**	84.82	14.58	0.60	48.44	06.21	45.29	0.05	0.01

The binary gas phase diffusivities for the reduction stage are obtained by calculating their values at a given temperature and pressure, according to the appropriate correlation (Equations A.5 to A.7). The parameter values were obtained from [111] and [112] and are listed in Table A.9.

$$\text{Equation 1: } d_{ij} = \left(\frac{AT^B}{P_{in}}\right)\left[\ln\left(\frac{C}{T}\right)\right]^{-2}\exp\left(-\frac{D}{T}-\frac{E}{T^2}\right) \tag{A.5}$$

$$\text{Equation 2: } d_{ij} = \left(\frac{AT^B}{P_{in}}\right)\exp\left(-\frac{D}{T}\right) \tag{A.6}$$

$$\text{Equation 3: } d_{ij} = \left(\frac{AT+B}{P_{in}}\right) \tag{A.7}$$

Table A.9. Diffusivity correlation coefficients for various gas pairs present in methane-fueled CLC.

Pair	A	B	C	D	E	Equation
H_2-CO	15.39×10^{-3}	1.548	0.316×10^8	-2.8	1067	A.5
H_2-CO_2	3.14×10^{-5}	1.75	-	11.7	0	A.6

CO-CO$_2$	0.577×10^{-5}	1.803	-	-	0	A.6
CO$_2$-H$_2$O	9.24×10^{-5}	1.5	-	307.9	0	A.6
H$_2$-CH$_4$	3.13×10^{-5}	1.765	-	-	0	A.6
H$_2$-H$_2$O	-	0.927	-	-	0	A.7
CH$_4$-H$_2$O	-	0.361	-	-	0	A.7
CH$_4$-CO$_2$	-	0.153	-	-	0	A.7

General correlations for reactor properties and dimensionless numbers are provided below:

$$A_c = \frac{\pi D^2}{4} \tag{A.8}$$

$$v = \frac{G}{\rho} \tag{A.9}$$

$$Q = \frac{G A_c}{\rho} \tag{A.10}$$

$$a_v = 6\frac{1-\epsilon_b}{D_p} \tag{A.11}$$

$$Re_p = \frac{v D_p \rho}{\mu(1-\epsilon_b)} \tag{A.12}$$

$$Re = \frac{v D_p \rho}{\mu} \tag{A.13}$$

$$Sc = \frac{\mu}{\rho D_{m,i}} \tag{A.14}$$

$$Pe_a = \frac{\frac{v}{1-\epsilon_b}D_p}{D_{ax,i}} \tag{A.15}$$

$$Pr = \frac{C'_{pf}\mu}{\lambda_m} \tag{A.16}$$

The heat and mass transfer coefficients are obtained using Equations A.17 and A.18 [111]:

$$k_c = 0.357 Re^{-0.359} Sc^{-\frac{2}{3}} \frac{G}{\rho \epsilon_b} \tag{A.17}$$

$$h_f = 1.37 \left(\frac{0.357}{\epsilon_b}\right)(C'_{pf}G) Re^{-0.359} Sc^{-\frac{2}{3}} \tag{A.18}$$

The effective axial dispersion coefficient can be calculated through the axial Peclet number, which can be obtained through the following correlation [113]:

$$\frac{1}{Pe_a} = \frac{\epsilon_b}{\tau_p Re_p Sc} + \frac{0.45}{1 + \frac{7.3}{Re_p Sc}} \tag{A.19}$$

The effective axial thermal conductivity is determined using Equation A.20 [114]:

$$\frac{\lambda_{ax}}{\lambda_m} = \frac{\lambda_{e0}}{\lambda_m} + 0.7 Pr Re_p \tag{A.20}$$

The effective diffusivity is calculated using the following correlations:

$$D_{m,i} = \frac{(1 - y_i)}{\sum_{j=1}^{n_g} \frac{1 - y_{ij}}{d_{ij}}} \tag{A.21}$$

$$D_{k.i} = \frac{d_{pore}}{3} \sqrt{\frac{8R'_g T}{\pi MW_{air}}} \tag{A.22}$$

$$\frac{1}{D_{e,i}} = \frac{\tau}{\epsilon_b} \left(\frac{1}{D_{m.i}} + \frac{1}{D_{k.i}}\right) \tag{A.23}$$

The thermal conductivity of the OC can be determined using Equation A.24:

$$\lambda_s = \frac{1}{\sum_{i=1}^{n_s} \frac{C_i}{\lambda_i}} \tag{A.24}$$

Appendix B – Supplemental Information for NMPC of Packed Bed CLC

Comparisons with Experimental Data

During model validation, the reduction model was also compared to simulation results from Jin et al. [27] at 973 K. The results are presented in Figure B.1.
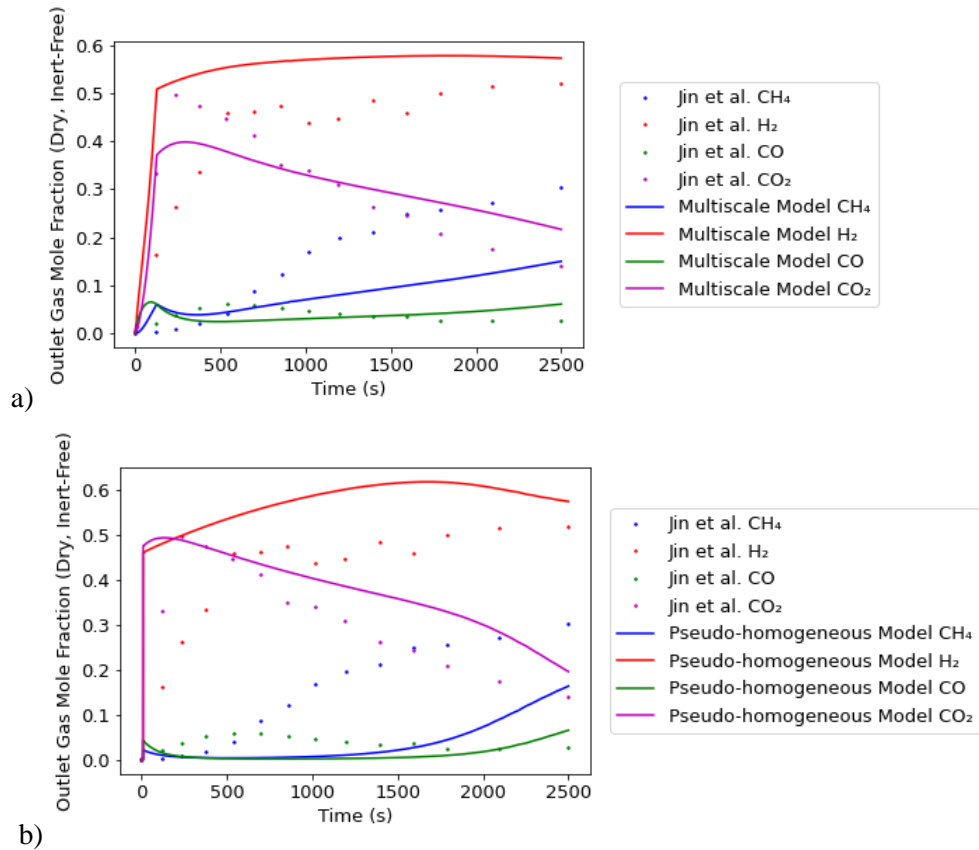

a)

b)

Figure B.1. Profiles for the outlet temperature of the reduction stage simulation compared to the simulation results presented by Jin et al. at 973 K using a) the multiscale model and b) the pseudo-homogeneous model.

For the reduction stage, when the multiscale model was used to perform a simulation under the experimental conditions used by Jin et al. [27] at a temperature of 973 K (Figure B.1a), it gives a

reasonable prediction of the outlet mole fractions. At this temperature, the outlet hydrogen fraction is overpredicted, and the outlet methane fraction is underpredicted, but the predicted outlet fractions follow the same trends as those observed experimentally. The pseudo-homogeneous model (Figure B.1b) shows greater mismatch under this set of conditions, as it neglects the diffusion within the particle and consequently predicts a faster reaction rate. This mismatch can be explained by the larger particle size, which increases the time required for gas to diffuse into the particle. Because the mismatch is small and the overall trends are still reasonable, the use of both the multiscale and pseudo-homogeneous models for NMPC is justified.

Sensitivity Analyses

Oxidation

For the sensitivity analyses of the oxidation stage, the nominal reactor design and operating conditions were the same as those used in NMPC, using an inlet air flux of 2.5 kg/m^2/s (with no inlet inert gas). Plots for the trends under different inlet mass fluxes (Figure B.2), reactor lengths (Figure B.3), and oxygen carrier loadings (Figure B.4) are presented below.
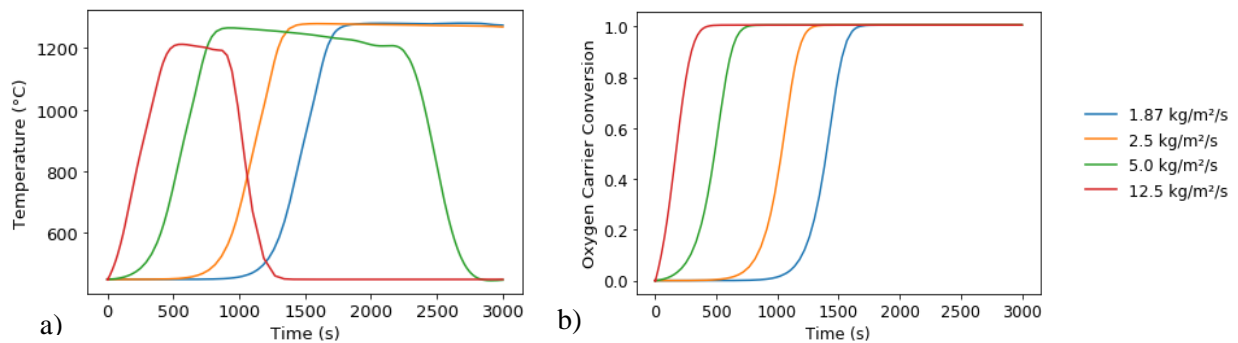
Figure B.2. Outlet a) temperature and b) oxygen carrier conversion profiles for the oxidation stage when the inlet mass flux is varied.
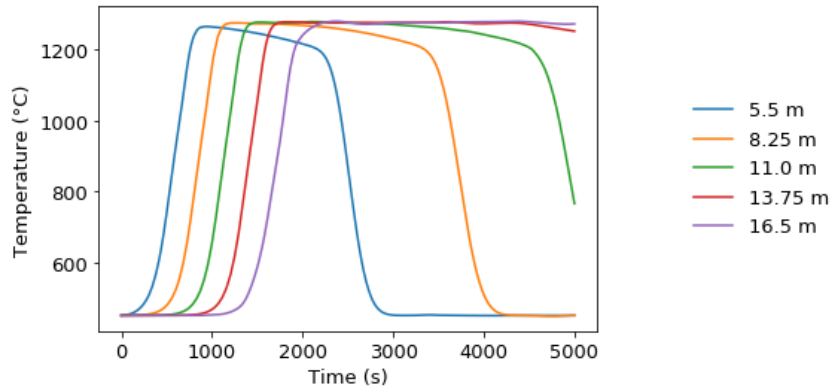
Figure B.3. Outlet temperature profiles for the oxidation stage when the reactor length is varied.
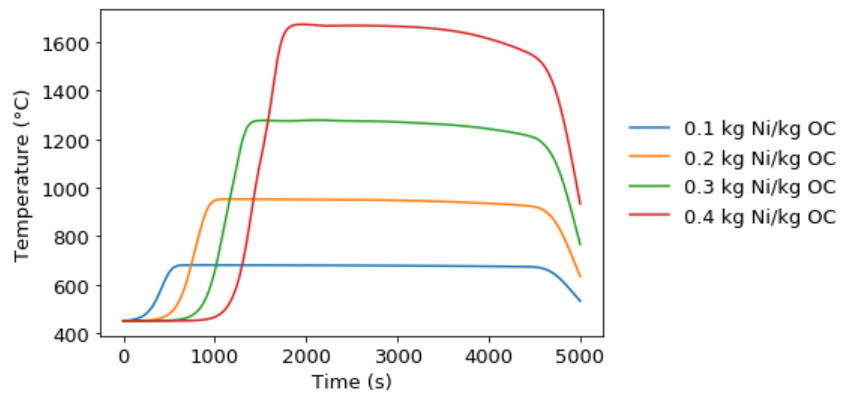

Figure B.4. Outlet temperature profiles for the oxidation stage when the active metal (Ni) loading on the oxygen carrier is varied.

As shown in Figure B.2a and Figure B.3, changing the inlet mass flux and reactor length do not affect the temperature achieved during the oxidation stage. Increasing the inlet mass flux speeds up the rate at which oxygen is introduced to the system and speeds up the progression of the reaction front through the reactor (Figure B.2b), thereby decreasing the time it takes for the heat front to reach the reactor outlet (Figure B.2a). Increasing the reactor length increases the time it takes for the heat front to reach the outlet as well as the amount of oxygen carrier in the system, which maintains a higher temperature for a longer period of time (Figure B.3). Finally, increasing the nickel concentration on the

107

OC can increase the outlet temperature, as presented in Figure B.4. Increasing the active metal concentration increases the amount of reaction that occurs at a given point in the reactor, which produces more heat and results in a higher outlet temperature achieved during the reaction.

Reduction Stage

For the sensitivity analysis of the reduction stage, the nominal conditions were also based on the conditions used in NMPC, using a nominal inlet fuel flux of 0.21 $kg/m^2/s$. The results of changing the inlet temperature (Figure B.5), nickel oxide loading (Figure B.6), inlet fuel flux (Figure B.7), and reactor length (Figure B.8) are presented.
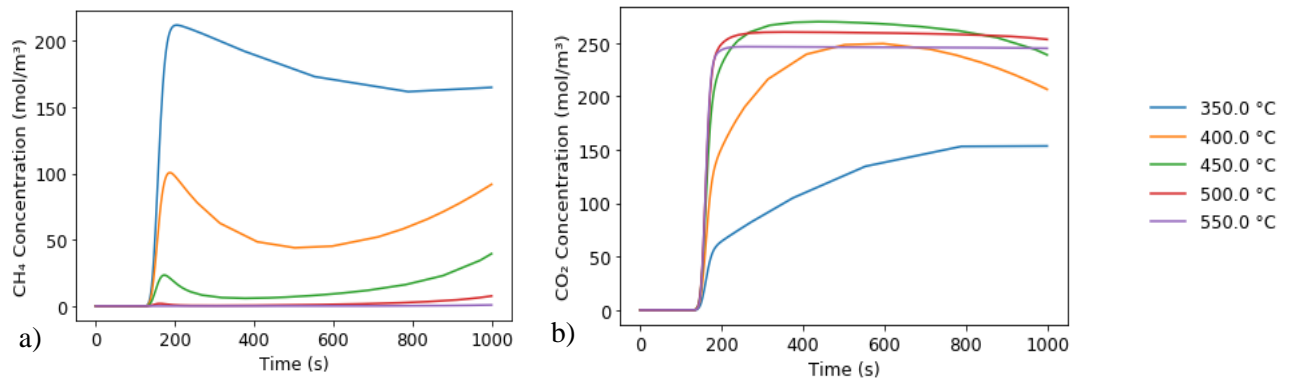
Figure B.5. Outlet a) methane and b) carbon dioxide concentration profiles for the reduction stage when the inlet temperature is varied.
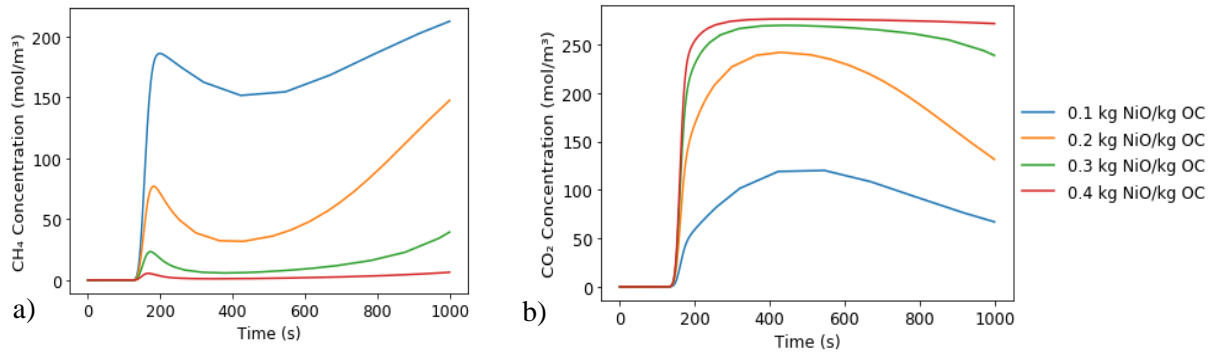
Figure B.6. Outlet a) methane and b) carbon dioxide concentration profiles for the reduction stage when the active metal loading on the oxygen carrier is varied.
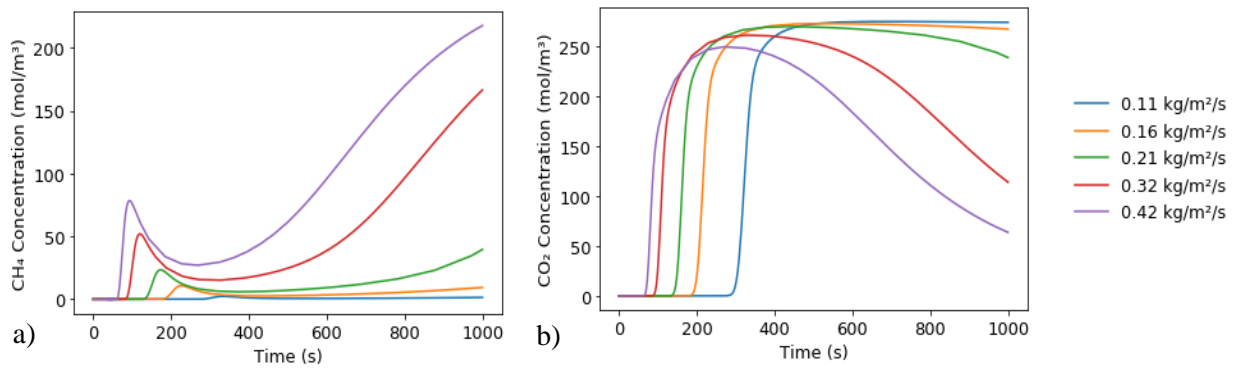

Figure B.7. Outlet a) methane and b) carbon dioxide concentration profiles for the reduction stage when the inlet fuel flux is varied.
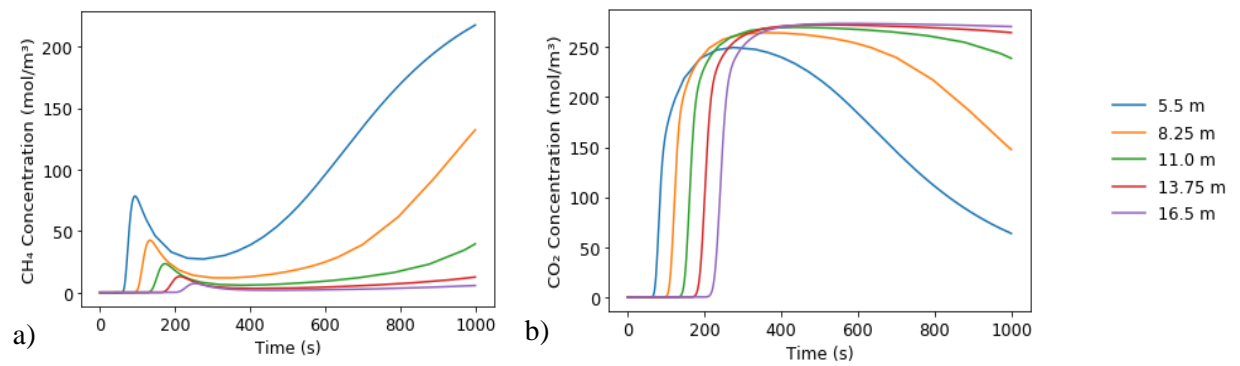

Figure B.8. Outlet a) methane and b) carbon dioxide concentration profiles for the reduction stage when the reactor length is varied.

Changing the temperature (Figure B.5) increases the reaction rates of the compounds in the system, which increases the rates of the oxygen carrier reactions, increasing the CH_4 conversion to CO_2. Changes to the active metal loading (Figure B.6) have a similar impact, as a higher NiO fraction increases the OC reaction rates, increasing the conversion of CH_4 to CO_2. The main difference is that changing the NiO fraction does not impact the equilibrium constant of the system, so the CO_2 concentration does not decrease as the active metal loading is further increased.

Changing the inlet fuel flux (Figure B.7) largely impacts the velocity of the reaction front, as in the oxidation stage, but as the reaction kinetics of the reduction stage are slower, the resulting change in residence time has a more prominent effect on the outlet concentrations. Increasing the fuel flux will decrease the residence time, resulting in higher concentrations of unreacted CH_4 at the outlet, and increasing the rate at which the OC reaches full conversion. Similarly, increasing the reactor length (Figure B.8) increases the residence time and decreases the unreacted CH_4, while increasing the length of time that CO_2 is produced due to the higher quantity of OC in the reactor.

NMPC Results: OC Conversion

The OC conversion profile at different points within the reactor during the oxidation stage is presented in Figure B.9.
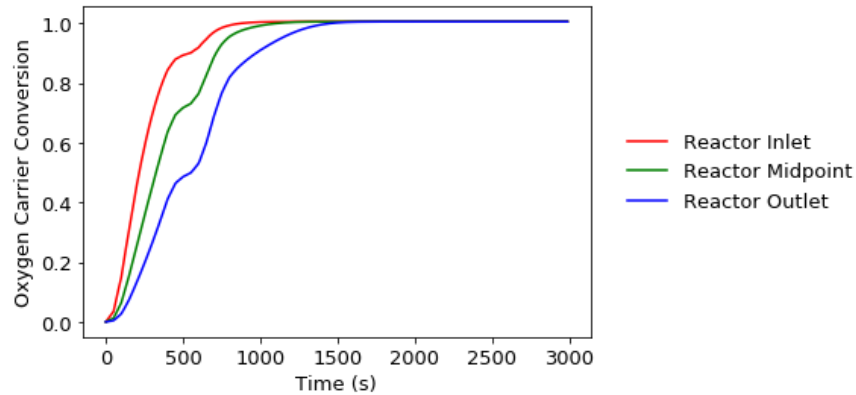
Figure B.9. Oxygen carrier conversion at different axial positions when NMPC is performed for the oxidation stage, using an outlet temperature setpoint of 900 °C.

When NMPC is performed for the oxidation stage of packed bed CLC, the OC conversion throughout the reactor increases quickly as air is introduced to the system. At about 500 s, the rate of OC conversion is slowed when the inlet air flux is decreased (as per Figure 3.8a); likewise, the conversion occurs more quickly when the air flux peaks for a second time at 700 s. Past 1000 s, the OC is has reached complete conversion, which is when the inlet mass flux is kept at its lower bound as the reactor enters the heat recovery phase.

Appendix C – Supplemental Information for Packed Bed Biomass-Fueled CL

Model Validation

Chemical-Looping Gasification

In addition to comparing the component syngas yields obtained by the model to those obtained experimentally by Liu et al. [18], the corresponding gasification efficiencies are calculated, shown in Figure C.1.
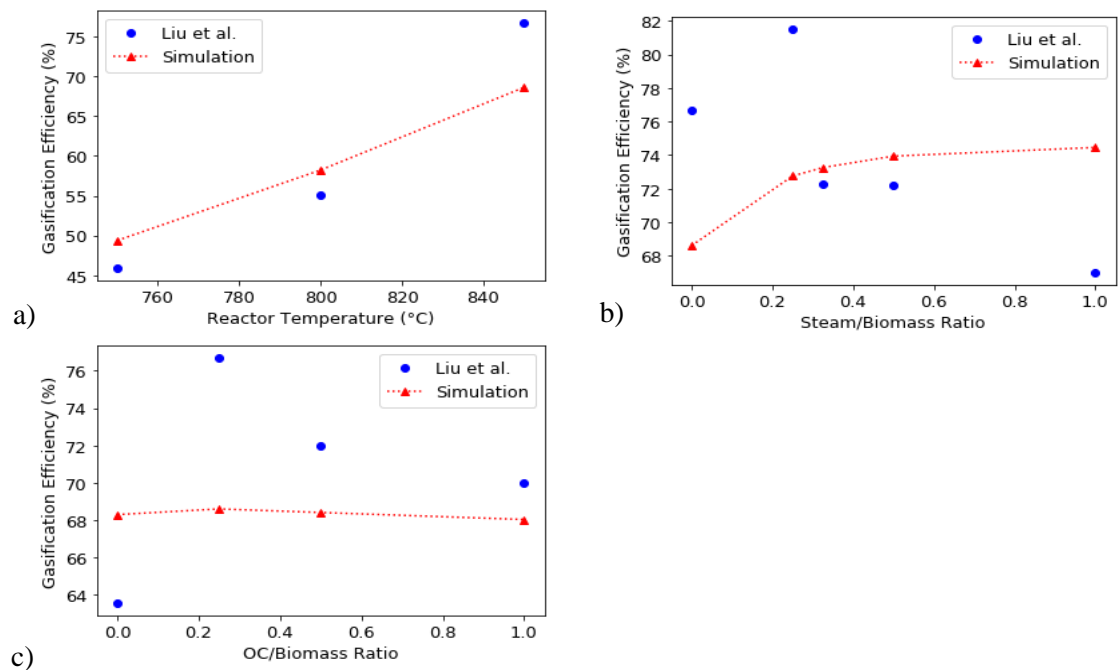

Figure C.1. Comparison between the gasification efficiencies obtained through Liu et al.'s experiment and through simulation results while varying a) the reactor temperature, b) the steam/biomass ratio, and c) the OC/biomass ratio.

When the reactor temperature is changed (Figure C.1a), the predicted gasification efficiency shows a similar trend to that observed in the experiment, increasing with higher temperatures, and increasing more steeply between 800 °C and 850 °C. When the OC/biomass ratio is changed (Figure C.1c), the gasification efficiency exhibits the same shape, although it does not change as drastically. This is because the gasification efficiency is a function of the component yields, and the simulated hydrogen yield (Figure 4.2c) did not increase as much as it had in the simulation by Liu et al., likely because the model does not account for the catalytic effect on secondary pyrolysis observed for the OC [98] [99]. Finally, when the steam/biomass ratio is changed (Figure C.1b), the model predicts a similar effect when steam is initially added to the reactor, although at higher steam/biomass ratios, the predicted gasification efficiency continues to increase. This is due to simulated hydrogen yields (Figure 4.2b) that continue to increase as steam is added to the system, increasing the syngas yield. As an additional verification, the steam/biomass ratio was increased beyond 1, and in this case, the hydrogen yield plateaued, and the gasification efficiency decreased.

Chemical-Looping Combustion

An additional sensitivity analysis was performed for the reactor network under chemical-looping combustion conditions to verify the model predictions. For this sensitivity analysis, the reactor was fully packed with oxygen carrier, and steam was used as the inlet gas. The reactor temperature, inlet biomass flowrate, and inlet steam flowrate were manipulated, and the effects on the component gas yields (Figure C.2) and inlet oxygen carrier conversions (Figure C.3) were subsequently evaluated.
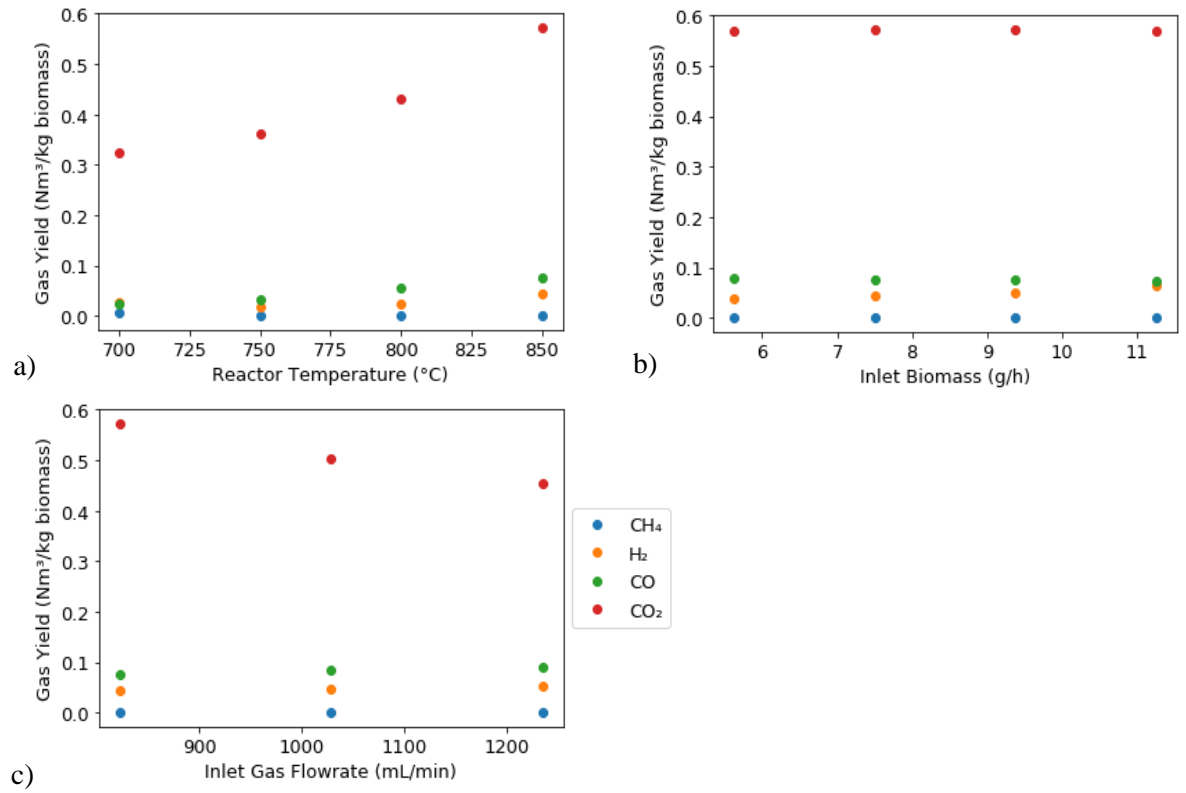
Figure C.2. Biomass-fueled CLC component gas yields at different a) reactor temperatures, b) biomass flowrates, and c) inlet steam flowrates.
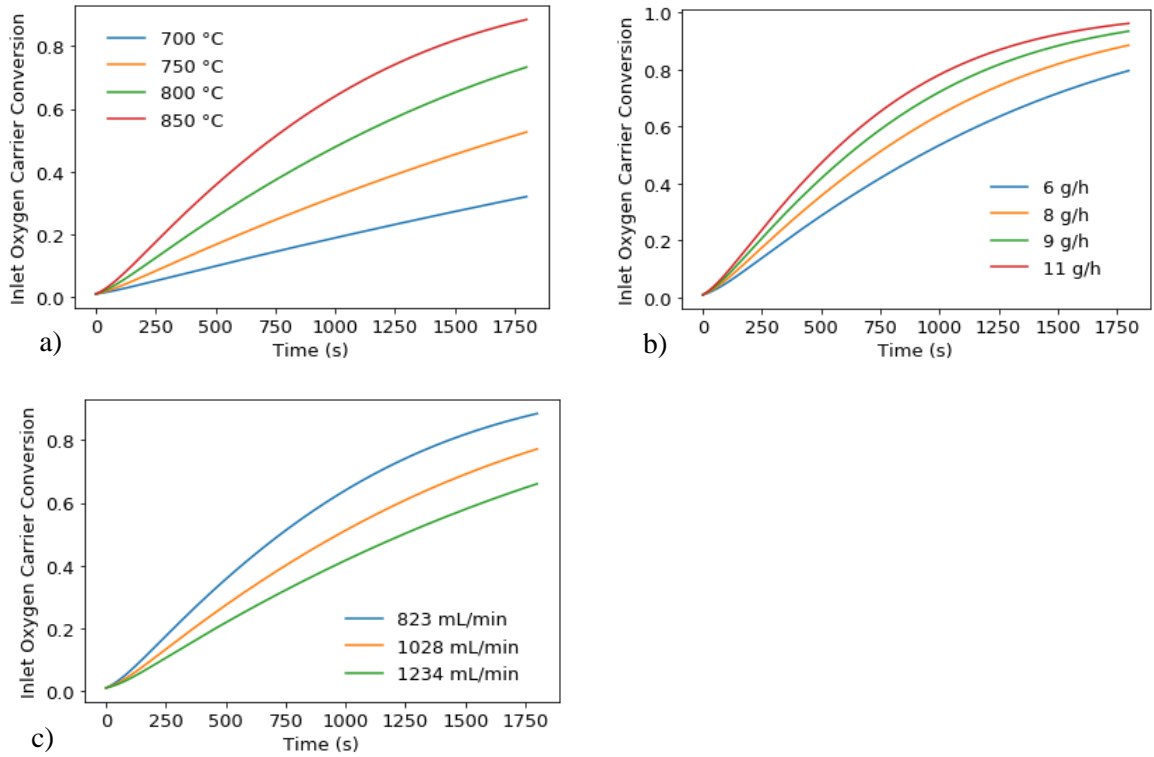
Figure C.3. Inlet oxygen carrier conversion for biomass-fueled CLC at different a) reactor temperatures, b) biomass flowrates, and c) inlet steam flowrates.

To increase the specific CO_2 yield, it was found that using a higher temperature (Figure C.2a) and lower flowrate (Figure C.2c) are the most effective conditions. At higher temperatures, the reactions occur more quickly, increasing the amount of char that reacts to produce gas, as well as the quantities of H_2 and CO that react with the OC to form H_2O and CO_2. Using a lower flowrate increases the residence time, also increasing the biomass conversion. Changing the inlet biomass (Figure C.2b) has minimal impact on the syngas yield, as the yields are normalized and reported in Nm^3/kg biomass. Nonetheless, because the oxygen carrier reaches complete conversion more quickly, the amount unreacted hydrogen reaching the outlet by the end of the reaction increases, thereby increasing the normalized hydrogen yield at higher biomass flowrates.

Figure C.3 shows the corresponding impact on the inlet oxygen carrier conversion. The inlet OC conversion is presented here as it most clearly shows the effect that changing the variables has on the OC. At higher temperatures (Figure C.3a), the OC reactions occur more quickly, increasing the conversion; decreasing the flowrate (Figure C.3c) increases the residence time, thereby increasing the OC conversion; increasing the biomass flowrate (Figure C.3b) increases the amount of fuel that the OC is exposed to, also increasing the conversion.

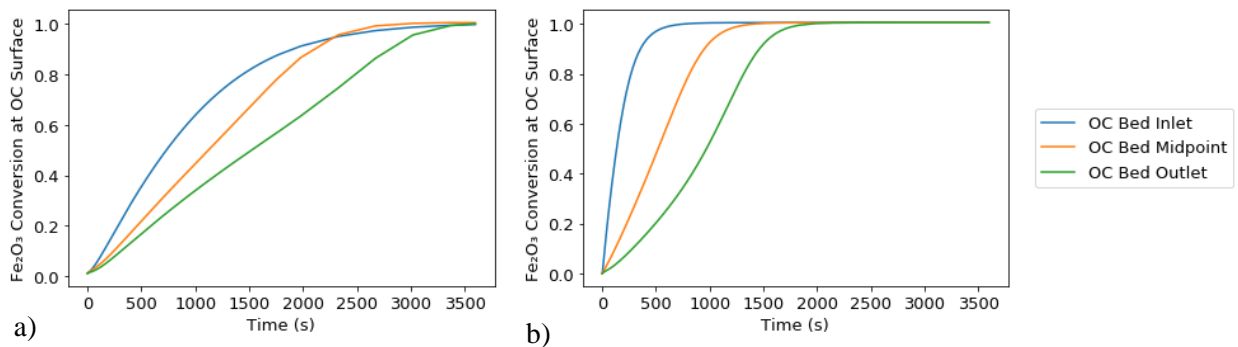**Simulation Results**

Chemical-Looping Combustion – OC Conversion

Figure C.4. Fe_2O_3 conversion at different points in the reactor for biomass-fueled CLC using steam as an inlet gas with a) a fully packed reactor (CLC-C) and b) a half-packed reactor with the OC at the outlet (CLC-G).

Figure C.4 shows the OC conversion profiles for biomass-fueled CLC in a reactor fully packed with OC (Figure C.4a) and in a reactor with half as much OC at the outlet (Figure C.4b), both of which have steam as the inlet gas. In Figure C.4a, the OC has nearly reached full conversion at 2100 s, where in Figure C.4b, this has occurred by about 1000 s; in both cases, this corresponds to the point in time where the outlet H_2 yield starts to increase (Figure 4.7).